

TKK Dissertations 196
Espoo 2009

**OIL FILM PRESSURE IN HYDRODYNAMIC
JOURNAL BEARINGS**

Doctoral Dissertation

Antti Valkonen



**Helsinki University of Technology
Faculty of Engineering and Architecture
Department of Engineering Design and Production**

TKK Dissertations 196
Espoo 2009

OIL FILM PRESSURE IN HYDRODYNAMIC JOURNAL BEARINGS

Doctoral Dissertation

Antti Valkonen

Dissertation for the degree of Doctor of Science in Technology to be presented with due permission of the Faculty of Engineering and Architecture for public examination and debate in Auditorium K216 at Helsinki University of Technology (Espoo, Finland) on the 4th of December, 2009, at 12 noon.

**Helsinki University of Technology
Faculty of Engineering and Architecture
Department of Engineering Design and Production**

**Teknillinen korkeakoulu
Insinööritieteiden ja arkkitehtuurin tiedekunta
Koneenrakennustekniikan laitos**

Distribution:

Helsinki University of Technology
Faculty of Engineering and Architecture
Department of Engineering Design and Production
P.O. Box 4100 (Otakaari 4)
FI - 02015 TKK
FINLAND
URL: <http://edp.tkk.fi/en/>
Tel. +358-9-451 3555
E-mail: tiina.nikander@tkk.fi

© 2009 Antti Valkonen

ISBN 978-952-248-161-0
ISBN 978-952-248-162-7 (PDF)
ISSN 1795-2239
ISSN 1795-4584 (PDF)
URL: <http://lib.tkk.fi/Diss/2009/isbn9789522481627/>

TKK-DISS-2672

Edita Prima Oy
Helsinki 2009



ABSTRACT OF DOCTORAL DISSERTATION	HELSINKI UNIVERSITY OF TECHNOLOGY P.O. BOX 1000, FI-02015 TTK http://www.tkk.fi
Author Antti Valkonen	
Name of the dissertation Oil film pressure in hydrodynamic journal bearings	
Manuscript submitted 22.05.2009	Manuscript revised 30.09.2009
Date of the defence 04.12.2009	
<input checked="" type="checkbox"/> Monograph	<input type="checkbox"/> Article dissertation (summary + original articles)
Faculty	Faculty of Engineering and Architecture
Department	Department of Engineering Design and Production
Field of research	Machine Design
Opponent(s)	Professor Arto Lehtovaara and Associate Professor Yuji Mihara
Supervisor	Professor Petri Kuosmanen
Instructor	
Abstract <p>Hydrodynamic journal bearings are critical power transmission components that are carrying increasingly high loads because of the increasing power density in various machines. Therefore, knowing the true operating conditions of hydrodynamic journal bearings is essential to machine design. Oil film pressure is one of the key operating parameters describing the operating conditions in hydrodynamic journal bearings. Measuring the oil film pressure in bearings has been a demanding task and therefore the subject has been studied mainly by mathematical means.</p> <p>The aim of this study was to determine the oil film pressure in real hydrodynamic journal bearings under realistic operating conditions. The study focused on engine bearings. Test rig experiments, simulations and calculations were carried out to determine the oil film pressure and to understand its relationship with other operating parameters. The main test apparatus was a versatile bearing test rig with a hydraulic loading system. The operating ranges of the bearings were determined by a novel method and the friction loss was determined by a heat flow analysis. The oil film pressure was measured by optical pressure sensors integrated in the bearings. The Author was a member of the research team that developed these sensors.</p> <p>The realistic oil film pressure was measured under hydrodynamic lubrication in realistic operating conditions. Significant differences between the measured and simulated oil film pressure distributions were found. Typically, the measured area of high pressure in the lubricating oil film was wider than the simulated one. The results can be used in the development and validation of mathematical methods for research into hydrodynamic journal bearings.</p>	
Keywords journal bearing, oil film pressure, hydrodynamic, lubrication, tribology	
ISBN (printed) 978-952-248-161-0	ISSN (printed) 1795-2239
ISBN (pdf) 978-952-248-162-7	ISSN (pdf) 1795-4584
Language English	Number of pages 170 + 31
Publisher Helsinki University of Technology, Department of Engineering Design and Production	
Print distribution Helsinki University of Technology, Department of Engineering Design and Production	
<input checked="" type="checkbox"/> The dissertation can be read at http://lib.tkk.fi/Diss/2009/isbn9789522481627/	



VÄITÖSKIRJAN TIIVISTELMÄ	TEKNILLINEN KORKEAKOULU PL 1000, 02015 TKK http://www.tkk.fi
Tekijä Antti Valkonen	
Väitöskirjan nimi Voiteluaineen kalvonpaine hydrodynaamisissa liukulaakereissa	
Käsikirjoituksen päivämäärä 22.05.2009	Korjatun käsikirjoituksen päivämäärä 30.09.2009
Väitöstilaisuuden ajankohta 04.12.2009	
<input checked="" type="checkbox"/> Monografia	<input type="checkbox"/> Yhdistelmäväitöskirja (yhteenveto + erillisartikkelit)
Tiedekunta	Insinööritieteiden ja arkkitehtuurin tiedekunta
Laitos	Koneenrakennustekniikan laitos
Tutkimusala	Koneensuunnittelu
Vastaväittäjä(t)	Professori Arto Lehtovaara ja Associate Professor Yuji Mihara
Työn valvoja	Professori Petri Kuosmanen
Työn ohjaaja	
Tiivistelmä <p>Hydrodynaamiset liukulaakerit ovat kriittisiä voimansiirtokomponentteja, jotka koneiden tehosiheyden suuretuessa kantavat yhä suurenevia kuormia. Tämän vuoksi koneiden suunnittelussa on oleellista tuntea hydrodynaamisten liukulaakerien todelliset toimintaolosuhteet. Voiteluaineen kalvonpaine on eräs tärkeimmistä hydrodynaamisten liukulaakerien toimintaolosuhteita kuvaavista parametreista. Voiteluaineen kalvonpaineen mittaaminen on ollut haastava tehtävä, minkä vuoksi aihetta on tutkittu yleensä matemaattisin menetelmin.</p> <p>Tämän tutkimuksen tavoitteena oli määrittää voiteluaineen kalvonpaine todellisissa liukulaakereissa todellisissa toimintaolosuhteissa. Tutkimus kohdistettiin moottorien laakereihin. Kalvonpaineen ja siihen yhteydessä olevien muiden parametrien määrittämiseksi tehtiin koepenkkitestejä, simulaatioita ja laskentaa. Tärkeimpänä koelaitteena käytettiin monipuolista laakerikoepenkkiä, jossa oli hydraulinen kuormitusjärjestelmä. Laakerien toiminta-alueet määritettiin uudella menetelmällä, ja kitkahäviö määritettiin lämpövirta-analysillä. Voiteluaineen kalvonpaine mitattiin laakereihin integroiduilla optisilla paineantureilla. Tekijä oli paineanturit kehittäneen tutkijaryhmän jäsen.</p> <p>Todellinen voiteluaineen kalvonpaine mitattiin hydrodynaamisessa voitelussa todellisissa toimintaolosuhteissa. Löydettiin merkittäviä eroja mitatun ja simuloitun voiteluaineen kalvonpaineen välillä: tyypillisesti mitattu korkeapaineinen alue voiteluainekalvossa oli laajempi kuin simuloimalla määritetty. Tuloksia voidaan käyttää kehitettäessä ja todennettaessa hydrodynaamisten liukulaakerien tutkimuksessa käytettyjä matemaattisia menetelmiä.</p>	
Asiasanat liukulaakeri, kalvonpaine, hydrodynaaminen, voitelu, tribologia	
ISBN (painettu) 978-952-248-161-0	ISSN (painettu) 1795-2239
ISBN (pdf) 978-952-248-162-7	ISSN (pdf) 1795-4584
Kieli englanti	Sivumäärä 170 + 31
Julkaisija Teknillinen korkeakoulu, Koneenrakennustekniikan laitos	
Painetun väitöskirjan jakelu Teknillinen korkeakoulu, Koneenrakennustekniikan laitos	
<input checked="" type="checkbox"/> Luettavissa verkossa osoitteessa http://lib.tkk.fi/Diss/2009/isbn9789522481627/	

Preface

This Doctoral Dissertation is the main result of a long term contract involving a good deal of hard work in peaceful office rooms and lively laboratory halls. During this long term contract, many things have changed in the Finnish world of academe and in Finland in general.

I thank my present supervisor Prof. Petri Kuosmanen and my former supervisor Prof. Mauri Airila for their encouraging guidance and valuable support during my postgraduate studies.

For their pleasant co-operation on numerous occasions, I am grateful to all my colleagues, fellow workers and superiors at Helsinki University of Technology, Lappeenranta University of Technology, VTT Technical Research Centre of Finland, Finnish Funding Agency for Technology and Innovation Tekes, and Musashi Institute of Technology, as well as to contact persons in many Finnish and foreign companies. I thank the following people for their help and encouragement during my long journey through the world of technical sciences:

Peter Andersson, Otto Blomstedt, Olof Calonius, Erkkö Fontell, Christian Forstner, Elga Gocheva-Fält, Pasi Halla-aho, Jari Halme, Pekka Hautala, Päivi Heimala, Juha Heinonen, Aino Helle, Pekka Hjon, Ari Hokkanen, Kenneth Holmberg, Ismo Hämäläinen, Erkki Jantunen, Jari Juhanko, Sami Jussila, Olli Jylhä, Markku Järviluoma, Osku Kaijalainen, Ilari Kallio, Markku Kapulainen, Seppo Kivioja, Panu Kiviluoma, Tommi Korolainen, Tero Koskenneva, Kai Koski, Jari Koskinen, Sami Koskinen, Markku Kuuva, Matti Kytö, Martti Larri, Ari Lehto, Gösta Liljenfeldt, Petri Makkonen, Hugues Marchand, Juhani Martikainen, Jyrki Molarius, Timo Murtonen, Mikko Mustonen, Jorma Niskala, Hannu Nurmi, Ilmari Pajamäki, Veikko Patronen, Jouni Pekkarinen, Matti Pietola, Esa Porkka, Helena Ronkainen, Kimmo Ruusuvoori, Vesa Saarijärvi, Vesa Saikko, Hannu Sainio, Timo Salin,

Kalevi Salmén, Matti Salo, Riku Salokangas, Carl-Erik Sandström, Wolfgang Schwarz, Jussi Sopanen, Ingmar Stuns, Kauko Suontama, Mike Sutton, Matti Säynätjoki, Jaana Tamminen, Santtu Teerihalme, Olavi Turunen, Simo Varjus, Ismo Vessonen, Juha Virtanen and Olli Ylöstalo.

Nowadays, scientific research work is typically supported by companies. I thank the following companies for the support during my research work: AVL List GmbH, Lubrizol Limited, Miba Gleitlager GmbH, Sisu Diesel Inc., Suomen Petrooli Oy and Wärtsilä Finland Oy.

I thank the Graduated School CE Tampere for providing financial support for my postgraduate studies.

My most lovely sweetheart Anne has given love, light and joy to my world. She has made this long term contract possible. *Omnia vincit Amor!* Finally, I thank my parents, Timo and Heli, and my brother, Heikki, for their love and encouragement.

Espoo, 5th May 2009

Antti Valkonen

Contents

Preface	7
Contents.....	9
List of Abbreviations	13
List of Symbols.....	15
1 Introduction.....	19
2 State of the Art	23
2.1 Basics of the operation of hydrodynamic journal bearings	23
2.2 Experimental bearing research	26
2.2.1 Test rigs	26
2.2.2 Test engines.....	29
2.2.3 Measuring methods and devices	30
2.3 Mathematical bearing research.....	34
3 Materials	39
3.1 General	39
3.2 Test rig.....	39
3.2.1 Main design.....	39
3.2.2 Frame.....	40
3.2.3 Bearing unit	41
3.2.4 Loading system	43
3.2.5 Drive system.....	44
3.2.6 Lubrication system	45
3.2.7 Control system	46
3.2.8 Measuring system.....	51
3.3 Bearings.....	59
3.4 Shafts.....	62

3.5	Housings	64
3.6	Lubricating oils.....	67
4	Methods.....	69
4.1	General	69
4.2	Test rig experiments	71
4.2.1	Determination of the operating range of journal bearings	71
4.2.2	Determination of the friction loss in journal bearings	79
4.2.3	Determination of the oil film temperature	86
4.2.4	Determination of the oil film thickness.....	87
4.2.5	Determination of the oil film pressure	89
4.2.6	Test material, lubricating oil supply and test run matrices	95
4.3	Simulations.....	98
4.3.1	Simulation software and procedure.....	98
4.3.2	Simulation model	99
4.3.3	Simulated viscosity and density	100
5	Results	103
5.1	Operating range	103
5.2	Friction loss	115
5.3	Oil film pressure with a rotating load.....	125
5.4	Oil film pressure with a static load.....	134
6	Discussion.....	145
7	Conclusions and recommendations	157
8	Summary.....	159
	References.....	165
Appendix A	Strength of the frame	A-1
Appendix B	Trial run.....	B-3

Appendix C	Calculations based on the engine data	C-9
Appendix D	Heat transfer coefficient	D-13
Appendix E	Calibration of the optical sensors	E-17
Appendix F	Relative eccentricity	F-23
Appendix G	Viscosity and density	G-25
Appendix H	Resultant of the local forces	H-29

List of Abbreviations

AC	alternating current
DC	direct current
EHD	elastohydrodynamic
FEA	finite element analysis
FEM	finite element method
HD	hydrodynamic
PID	proportional-integral-derivative
TEHD	thermoelastohydrodynamic

List of Symbols

A	surface area of the housing, viscosity parameter, coefficient
A_s	outflow area of the lubrication gap
A_1	amplitude (of the cylinder number 1)
a_i	coefficient
B	width of the bearing, viscosity parameter, coefficient
c	specific heat capacity
c_{Ref}	reference specific heat capacity
c_i	coefficient
C	viscosity parameter, coefficient
D	diameter of the bearing, damping matrix, coefficient
d	diameter of the shaft, distance
e	eccentricity
e	Neper number
F	bearing load, load, resultant
F_x	horizontal component of the resultant
F_{xi}	horizontal component of the cylinder force number i
F_y	vertical component of the resultant
F_{yi}	vertical component of the cylinder force number i
F_1	cylinder force number 1
f_1	density parameter
F_2	cylinder force number 2
f_2	density parameter
F_3	cylinder force number 3
f_3	density parameter
f	frequency, nodal force acting on the oil film

f_A	outer force acting on the journal
f_J	oil film force acting on the journal
h	oil film thickness, clearance, heat transfer coefficient
h_0	minimum oil film thickness
I	intensity
K	stiffness matrix
k_1	coefficient
k_2	coefficient
k_3	multiplier
k_4	exponent
L	bearing load
L_{1m}	resultant
L_{1s}	resultant
L_{2m}	resultant
L_{2s}	resultant
M	total torque, mass matrix
M_0	torque
m	journal mass
N	integer, number
n	rotational speed of the shaft
P	total friction loss
P	pressure, oil film pressure
p_s	specific load
P_s	friction power of the supporting bearings
P_0	friction power
q	volume flow
R	resultant, radius of curvature
Ra	arithmetical mean roughness

So	Sommerfeld number
s	thickness
T	temperature
T_A	average temperature
T_H	temperature of the housing
T_0	reference temperature
T_B	operating temperature of the bearing
T_R	ambient temperature
T_{Ref}	reference temperature
T_1	inlet temperature
T_2	outlet temperature
t	time, thickness
t_a	thickness of bronze layer
t_s	thickness of steel layer
u	coordinate
u_B	shell deformation
u_s	sliding velocity, sliding speed
u_1	velocity
u_2	velocity
V_s	lubrication gap volume
v	coordinate, deflection, kinematic viscosity
x	coordinate
x_j	journal position
y	coordinate
z	coordinate
α	angle, angular position, angle of rotation, viscosity parameter
β	angle
γ	resolution

ε	relative eccentricity
η	dynamic viscosity, viscosity
θ	filling factor
μ	friction coefficient
ρ	density
ρ_{Ref}	reference density
ρ_0	reference density
τ	shear stress
Φ_{A}	heat flow in convection through the housing
Φ_{q}	heat flow transferred by the lubricating oil
ϕ	diameter
ϕ_1	phase difference (of the cylinder number 1)
ψ	relative bearing clearance
ω	angular velocity, hydrodynamic angular velocity
ω_{s}	angular velocity of the shaft

1 Introduction

Background

The power density in various machines, for example in internal combustion engines, is increasing year by year due to growing demands for mechanical and economic efficiency. In machine design, one of the consequences of an increase in power density is that critical power transmission components have to carry increasingly high loads.

Hydrodynamic journal bearings are typical critical power transmission components that carry high loads in different machines. In machine design, therefore, it is essential to know the true or expected operating conditions of the bearings. These operating conditions can be studied both by experimental and mathematical means, for example in test rig experiments, in field or laboratory tests with engines and by calculation or simulation.

Numerous studies of the operating conditions of hydrodynamic journal bearings have been made during the last decades. Still, the case is far from closed. For example, there are a limited number of studies that carry out an in-depth examination of the true operating conditions of bearings in true-scale experiments. There is also a need for experimental studies to verify the theoretical ones.

Research problem

The operating conditions of hydrodynamic journal bearings can be described by a set of tribological variables called key operating parameters. For example, the load level of a hydrodynamic journal bearing is described by two parameters: the specific load and the sliding speed. The key operating parameters most directly related to the bearing-lubricant-shaft contact are the oil film temperature, oil film thickness and oil film pressure. These three key parameters can be determined by experimental or mathematical means with varying levels of complexity.

Until now, oil film pressure in hydrodynamic journal bearings has been studied mainly by mathematical means, because the experimental determination of oil film pressure has been a demanding or even an unfeasible task. Under real operating conditions, there are typically many practicalities that complicate the experimental determination of true oil film pressure in a certain point or at a certain moment. The oil film may be extremely thin and therefore sensitive to different disturbing factors, for example defects in geometry. In addition, the level of the oil film pressure may be extremely high or have a high level of dynamic variability.

Aim of the research

The main aim of the study was to determine the oil film pressure in hydrodynamic journal bearings carrying realistic loads. In addition, the relationship between the oil film pressure and other key operating parameters of journal bearings was studied. Therefore, the study also included the determination of the operating range, friction loss, oil film temperature and oil film thickness.

Research methods

The operation of journal bearings was studied both by experimental means in a laboratory environment and by theoretical means using mathematical simulations. In the experimental study, the main test apparatus was a versatile bearing test rig with an advanced measuring system for determining practically all major tribological variables of journal bearings. The test rig was developed by a research team. The Author was in charge of the main design, construction and operation of the test rig. The oil film pressure in hydrodynamic journal bearings was measured by optical pressure sensors developed by a research team, of which the Author was a member. In the theoretical study, advanced simulation software was used for the bearing simulation. The simulations were executed by the Author.

Scope of the research

Common journal bearings running under hydrodynamic operating conditions were studied. The experiments with the bearings were made in true scale and realistic bearing

loads were used. The study focused on the main bearings in the crank train of a high-speed diesel engine.

Contribution

The realistic oil film pressure in real types of hydrodynamic journal bearings was measured at various operating points across the realistic operating range. By determining the oil film pressure in hydrodynamic journal bearings, it is possible to increase knowledge about the true operating conditions of bearings. The knowledge can be used in the development of safer and more efficient machines and engines with hydrodynamic journal bearings that carry high and dynamic loads.

2 State of the Art

2.1 Basics of the operation of hydrodynamic journal bearings

Lubrication reduces friction between two surfaces (such as sliding surfaces of a bearing and a shaft) in relative motion. It is typically categorised as boundary, mixed and hydrodynamic lubrication, for example by Heywood (1988), Becker (2004) and Gleghorn and Bonassar (2008). When a journal bearing operates under boundary lubrication, the sliding surfaces of the bearing and shaft are practically in direct contact and friction is at its highest level. Lower friction levels are achieved through the use of mixed lubrication, where the sliding surfaces are partially separated by the lubricant, and of hydrodynamic lubrication, where the sliding surfaces are completely separated by the lubricant.

To illustrate how friction varies under different lubrication conditions, Stribeck curves (or diagrams) have been used widely in different engineering sciences. In Stribeck curves, the friction coefficient is presented as a function of a dimensionless parameter calculated from the dynamic viscosity, angular speed and pressure (see Figure 2-1). The above-mentioned parameter is typically called the duty parameter or Hersey number. The minimum of the friction coefficient is reached at the critical value of the duty parameter, at the dividing line between the mixed and hydrodynamic lubrication zones. Heywood (1988) presented a Stribeck curve for a journal bearing. Methods for the calculation of Stribeck curves were studied by de Kraker *et al.* (2007). They calculated the friction coefficient as a function of the journal frequency at different values of the projected bearing pressure.

A hydrodynamic journal bearing (see Figure 2-2) is designed to operate normally under hydrodynamic lubrication, where hydrodynamic pressure (see Figure 2-3) in the lubricant keeps the sliding surfaces of the bearing and shaft separated from each other. The hydrodynamic pressure is caused by the sliding motion.

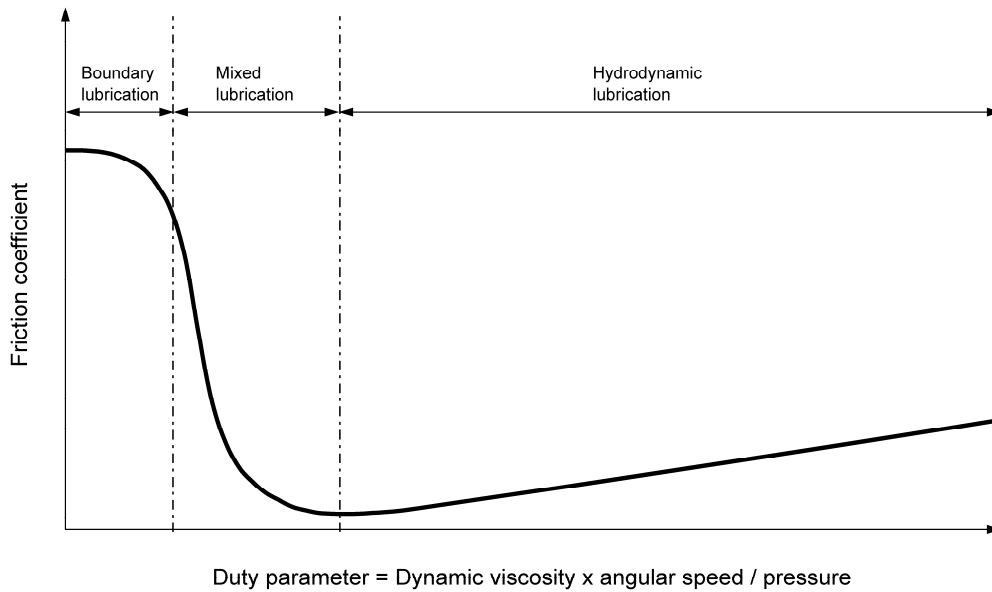


Figure 2-1. Stribeck curve showing the friction coefficient as a function of the duty parameter under boundary, mixed and hydrodynamic lubrication.

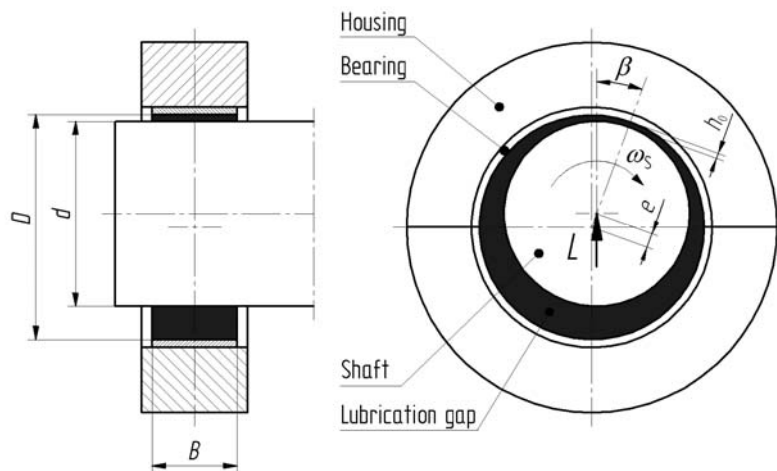


Figure 2-2. Hydrodynamic journal bearing with the diameter D and the width B carrying the bearing load L . The shaft with the diameter d runs at the angular velocity ω_s . An oil film in the lubrication gap separates the sliding surfaces of the bearing and shaft. The eccentricity e and the angle β determine the position of the point with the minimum oil film thickness h_0 .

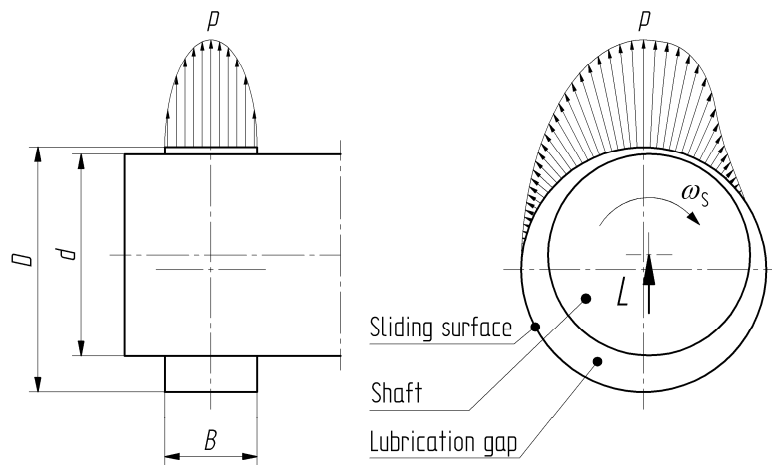


Figure 2-3. Distribution of the hydrodynamic pressure p in the oil film on the sliding surface of a hydrodynamic journal bearing with the diameter D and the width B carrying the bearing load L . The shaft with the diameter d runs at the angular velocity ω_s .

Hydrodynamic journal bearings are simple but critical components and numerous parameters influence their operation. Therefore, research into the operation of hydrodynamic journal bearings is typically a demanding task requiring extensive knowledge of machine design. Knowledge for research into bearings can be obtained in test rig experiments, by performing field or laboratory tests on engines and by mathematical means. There are advantages and disadvantages to each of the above-mentioned ways to collect information about bearings.

2.2 Experimental bearing research

2.2.1 Test rigs

Test rig experiments usually have one or more of the following benefits: applicability to multiple or repetitive tests, wide range of operation, possibility of performing extreme value tests safely, possibility of using accurately adjusted bearing loads, possibility of studying different variables separately and possibility of performing demanding measurements. Therefore, in many cases in the practical bearing research, the optimal way to obtain knowledge is to carry out test rig experiments. Test rig experiments are also typically performed as preliminary tests before engines are tested in the laboratory or in the field, as well as for verifying bearing calculations.

Naturally, the benefits of a test rig experiment depend heavily on the characteristics of the bearing test apparatus. The following are some obvious requirements for a useful bearing test apparatus: versatility, wide operating range, applicability to true-scale experiments with realistic bearing loads, and advanced control and measuring systems.

Various bearing test rigs have been developed for experimental bearing research work at different research institutes and industrial companies. Naturally, various designs have been used for different applications, for example for testing bearing designs or materials, testing bearing lubricants or lubrication solutions, testing durability, or for testing carried out during the development of measuring devices to be used in tribological research. Typically, a test rig consists of a frame, a bearing unit and loading, drive, lubrication, control and measuring systems.

The main components of the test rig are installed in the frame. The frame is generally relatively rigid to avoid disturbing deformations and vibrations.

The bearing unit consists of the bearing, housing, shaft and supporting bearings. The housing in which the bearing is placed for testing typically has a simplified cubic or cylindrical design, but housings of real types have also been used. For example, Dowell (2005) used a real type housing to simulate a connecting rod big-end. A large high-precision roller bearing with both radial and axial load carrying capacity is a common supporting bearing type used in low and medium speed applications. These have been used, for example, by Savaşkan *et al.* (2002). In high speed or extreme load applications, sliding bearings have been used as an alternative, for example by Okamoto *et al.* (2000) and Zhou *et al.* (2004). The shaft is typically supported on both sides of the bearing, but single side support solutions have also been used, for example by Tanaka (2000).

The loading system generates the bearing load. There are test rigs with dynamic and static loading systems. Hydraulic and pneumatic cylinders are widely used in loading systems. Dowell (2005) used a test rig with a single hydraulic cylinder in an experimental investigation of journal bearing seizure. Test rigs with a single hydraulic cylinder were also used by Del Din and Kassfeldt (1999), Durak *et al.* (2003) and Savaşkan *et al.* (2002). Test rigs with a single pneumatic cylinder were used by Marx and Junghans (1996), Syverud (2001) and Brito *et al.* (2006). Eccentric rotating shafts were used to generate high dynamic bearing loads by Okamoto *et al.* (2000). Electro-magnets generating impulses were used by Jiang *et al.* (1997). A test rig with dead weights was used for bearing loading in tests on journal bearings lubricated with water by Andersson and Lintula (1994) and Andersson *et al.* (1996). Dead weights were also used for bearing loading by Ozsarac *et al.* (2007), Sinanoğlu *et al.* (2005), Syverud and Tanaka (1997), Tanaka (2000) and Ünlü *et al.* (2007). A loader with a spring to generate the bearing load was used by Tomimoto (2003). A loading system with spring-opposed bellows was used by Zhou *et al.* (2004). Experiments with bearings carrying the mass of a rotor were made by Ene *et al.* (2008).

The drive system drives the shaft and consists of a power unit and a transmission unit. Because of relatively low power losses in the bearings, high output from the driving unit

is seldom required. An electric motor is a common power unit type because of its high applicability to a laboratory environment. Alternatively, both direct current (DC) and alternating current (AC) motors have been used. DC motors were used by Jiang *et al.* (1997) and Zhou *et al.* (2004). AC motors were used by Brito *et al.* (2006) and Durak *et al.* (2003). Turbines have also been used to drive the shaft. An example of this is the test rig by Ene *et al.* (2008), in which the shaft is driven by an air turbine at rotational speeds of up to $1 \cdot 10^3$ 1/s. Belts and gearboxes are used for the transmission. Belts were used, for example, by Syverud and Tanaka (1997) and Berg (1996), whereas Zhou *et al.* (2004) used a gear box. Drive systems with and without a drive shaft exist. Designs with a drive shaft have been used by Berg (1996) and Dowell (2005). In designs with a drive shaft, flexible couplings between the test shaft and drive shaft have been used to dampen impulses from the power unit and to avoid the effects of possible alignment errors between the shafts. Designs without a drive shaft have been used by Del Din and Kassfeldt (1999), Tanaka (2000) and Syverud (2001). For accurate rotational speed control, the power unit is driven by a feedback controller. Flywheels have been used to decrease variation in rotational speed.

The lubrication system lubricates the bearing. Circulation lubrication systems consisting of a tank, pump, heating or cooling devices, filters and pipeline have been used for the bearing. Supporting bearings are lubricated separately by oil or grease.

The control system controls the main operations of the test rig. Automated control systems have been favoured, especially with large test rigs used for long-term testing. Manual control is suitable for small test rigs used for short-term testing.

The measuring system measures and records the data required for the control and analysis of the case that is being studied. The measuring system consists of measuring and recording devices. Devices to measure the variables related to contacts between the bearing, lubricant and shaft are placed in the bearing, housing or shaft.

2.2.2 Test engines

Experiments for the bearing research have been carried out both on running and non-running test engines. Mihara *et al.* (1995) carried out experiments with a running two-cylinder diesel engine with a displacement of 1885 cm³ and used a thin film pressure sensor to measure oil film pressure in the main bearing with a diameter of 62 mm. Mihara *et al.* (1996) carried out experiments with a running four-cylinder petrol engine with a displacement of 1588 cm³. They used a thin film strain sensor to study the influence of bearing deformation on the output of a thin film pressure sensor measuring the oil film pressure in the main bearing, the diameter of which was 52 mm. Someya and Mihara (2004) used thin film pressure sensors to measure oil film pressure in the main bearing of a running four-cylinder diesel engine with a displacement of 5307 cm³. The diameter of the main bearing was 81 mm. As a part of a study of the main bearing load and the deformation of an engine, Ichikawa *et al.* (1995) used thin film pressure sensors to measure oil film pressure in the main bearing of a running petrol engine. Moreau *et al.* (2002) used eddy current gap sensors to measure the oil film thickness in three main bearings and a connecting rod big-end bearing of a running four-cylinder petrol engine with a displacement of 2 dm³. The diameter of the main bearing was 60 mm. Irani *et al.* (1997) used capacitive transducers to measure oil film thickness in the main bearing of a running six-cylinder diesel engine with a displacement of 9 dm³. The diameter of the main bearing was 90 mm. Leclère *et al.* (2005) measured the main bearing loads indirectly in an operating diesel engine by using accelerometers measuring the three-dimensional response of crankshaft bearing caps. Berg (1996) measured temperatures in the main bearing to determine friction loss in a running four-cylinder diesel engine with a displacement of 1896 cm³. The diameter of the main bearing was 54 mm. Aoyama *et al.* (2003) analysed noise occurrence caused by cavitation in the main bearing of a six-cylinder diesel engine with a displacement of 4.2 dm³. Nursoy *et al.* (2008) used a four-cylinder engine, driven by an electric motor, as a test machine in a study of the wear behaviour of a crankshaft bearing.

2.2.3 Measuring methods and devices

Different measuring devices have been used in experimental studies to determine the main tribological parameters related to the hydrodynamic journal bearings. Typical measuring methods and devices are described below.

To measure oil film pressure, thin film pressure sensors consisting of thin material layers on the sliding surface of the bearing were used by Ichikawa *et al.* (1995), Mihara *et al.* (1995), Mihara *et al.* (1996), Mihara and Someya (2002) and Someya and Mihara (2004). The pressure sensors typically consist of three layers of material with a total thickness of about 6 μm (Someya and Mihara, 2004). The pressure-sensitive part of the sensor is called sensitive film. It is in the middlemost layer and is made of Manganin, an alloy of copper, manganese and nickel. This pressure-sensitive part is connected as the fourth resistor in a Wheatstone bridge. The operation of the thin film pressure sensor is based on the change of resistance in the pressure-sensitive part when it is loaded by pressure. The lowest layer, called insulation film, electrically insulates the sensitive film from the bearing shell. The uppermost layer, called protection film, protects the sensitive film from wear. Because the surface of the protection film is plain, the thin film pressure sensor resembles a common plain coating on the sliding surface of the bearing. Masuda *et al.* (1992) carried out test rig experiments in which oil film pressure in a connecting rod big-end bearing was measured by a semi-conductor strain gauge-type transducer embedded in the surface of the crankpin. They used a slip ring to transmit the pressure signal from the crankpin to the data recorder. Brito *et al.* (2006) used high precision Bourdon pressure gauges attached via manifold valves to a series of bores in the circumferential centreline of the bush to measure the oil film pressure in a journal bearing with two axial grooves. They used a total of fourteen pressure gauges to determine the oil film pressure distribution. Sinanoğlu *et al.* (2005) determined the oil film distribution by using sixteen manometer tubes. They drilled twelve holes in the circumferential direction and four holes in the axial direction of the bearing shell to place the manometer tubes. The first optical pressure sensor to measure oil film pressure in journal bearings was developed by Ronkainen *et al.* (2008). In this study, different

versions of the above-mentioned optical pressure sensor were used to measure oil film pressure in hydrodynamic journal bearings (see Chapter 4.2.5).

Determining oil film thickness has been typically based on shaft position measurements. Oil film thickness and other variables related directly to the shaft position (such as the eccentricity and orbital path of the shaft and the bearing play or clearance) have been calculated from shaft position data. In the test rig experiments carried out by Berg (1996), laser distance sensors installed in a ring surrounding the bearing housing were used to measure the distance to the shaft and, thereby, to determine the bearing play and the orbital path of the shaft. Moreau *et al.* (2002) used eddy current gap sensors to measure the oil film thickness on the main bearings of a running petrol engine. They used four sensors on each bearing. In their study of the performance of a hydrodynamic journal bearing with axial grooves, Brito *et al.* (2006) measured the relative position of a shaft using two pairs of eddy current proximity probes installed in the bush. They took into consideration the estimated thermal deformations that influence the shaft position measurements. By measuring the total capacitance of the oil film, Bates *et al.* (1990) determined the oil film thickness in the connecting rod big-end bearing of a running petrol engine. They electrically insulated the bearing shells from the shaft using a thin layer of alumina ceramic and calculated the minimum oil film thickness as a function of the measured capacitance. Ahn (2006) presented a cylindrical capacitive sensor for measuring both radial and axial motions in rotating machinery. Irani *et al.* (1997) used capacitive transducers to measure oil film thickness in the main bearing in a running diesel engine. They found that these capacitive transducers were suitable and had high durability and long-time stability. Tomimoto (2003) used an inductive displacement meter to measure oil film thickness in test rig experiments with journal bearings. In test rig experiments with a single bore journal bearing, Syverud and Tanaka (1997) determined the eccentricity of a shaft by using a total of eight distance sensors. They positioned four distance sensors on the front side and four on the back side of the bearing to measure the distance to the shaft.

Methods to determine oil film temperature have been typically based on the measurement of the operating temperature of the bearing. To measure the oil film temperature, thin film thermocouples formed on the sliding surface of bearings were used by Mihara *et al.* (1995) and Someya and Mihara (2004). A typical thin film thermocouple consists of three different material layers with a total thickness of about 6 μm (Someya and Mihara, 2004): The middlemost layer is the temperature-sensitive part of the thermocouple and consists of two parts. The first part is made of chrome and the other of constantan. The temperature-sensitive part is connected as the fourth resistor in a Wheatstone bridge and the operation of the thin film thermocouple is based on changes in resistance in the temperature-sensitive part when it is subjected to a change in temperature. The lowest layer is called insulation film and electrically insulates the sensitive film from the bearing shell. The uppermost layer, known as protection film, protects the sensitive film from wear. Syverud and Tanaka (1997) used nine copper-constantan thermocouples to measure the bearing surface temperature at the bearing mid-line. They fixed the thermocouples with an adhesive in small bores drilled from the outside of the bearing. Dowell (2005) measured the temperature of the bearing by using three spring loaded temperature sensors pressed against the back of the bearing shell.

Friction loss has been typically determined based on measurements of torque or heat flow caused by the friction. Andersson and Lintula (1994) and Andersson *et al.* (1996) determined the coefficient of friction of water-lubricated journal bearings by using a force transducer to measure friction torque reaction force in a lever arm. Del Din and Kassfeldt (1999) used a lever arm equipped with strain gauges to measure friction torque in test rig experiments performed to study wear characteristics under mixed lubrication conditions in a journal bearing. Durak *et al.* (2003) used a lever and beam with strain gauges to measure the friction force. Marx and Junghans (1996) used a lever arm with a force transducer to measure the friction force. Mosleh *et al.* (2002) used a lever arm with a wire connected to a load cell to measure the friction force. In a test rig used by Tomimoto (2003), the friction was measured by a torque sensor placed between the shaft and the servomotor driving the shaft. To determine the friction loss in test rig experiments with a hydrodynamic journal bearing, Brito *et al.* (2006) used a static

torque sensor to measure the torque applied to a bush surrounding the bearing. They calculated the friction loss as a function of the bush torque, applied load, shaft eccentricity, attitude angle and angular velocity. In a test rig used by Ünlü and Atik (2007), the friction coefficient was determined by using a spring and comparator. To determine the friction loss of a bearing in a running four-stroke diesel engine, Berg (1996) carried out a thorough analysis of the heat flow caused by friction. The heat flow analysis was based on numerous temperature, pressure, flow, load and torque measurements. In the engine, Berg used five temperature-measurement points in or close to the main bearing, the oil supply channel and the oil sump. In addition, there were other temperature-measurement points in various locations and parameters related to the oil supply were measured. The torque of the engine was measured by a hydraulic brake.

One of the typical parameters that is determined experimentally is the real bearing load, especially in real applications. Yang *et al.* (2007) presented a bearing force sensor for simultaneously measuring bearing loads in three dimensions. They designed the force sensor for sliding bearings within large rotor-bearing systems. They placed the force sensor between the housing and the base of the housing. Leclère *et al.* (2005) carried out an indirect measurement of the main bearing loads in a running diesel engine. They used the engine structure equipped with numerous accelerometers as a multi-force sensor and determined the bearing loads by analysing the measured three-dimensional response in the engine structure.

2.3 Mathematical bearing research

For mathematical research into hydrodynamic journal bearings, various bearing simulation methods have been developed. These bearing simulation methods are typically based on numerical solutions of different versions of the Reynolds differential equation. The simulation methods based on the solution of the Reynolds equation can be divided, for example, into the following categories: hydrodynamic (HD), elastohydrodynamic (EHD) and thermoelastohydrodynamic (TEHD) methods.

The hydrodynamic and elastohydrodynamic methods are based on the extended Reynolds equation given by (Bukovnik *et al.* 2006):

$$\frac{\partial}{\partial x} \left(\frac{1}{12\eta} \theta h^3 \frac{\partial p}{\partial x} \right) + \frac{\partial}{\partial z} \left(\frac{1}{12\eta} \theta h^3 \frac{\partial p}{\partial z} \right) = \frac{u_1 + u_2}{2} \frac{\partial(\theta h)}{\partial x} + \frac{\partial(h\theta)}{\partial t} \quad (1)$$

where x is the coordinate,
 η is the dynamic viscosity,
 θ is the filling factor,
 h is the clearance,
 p is the pressure,
 z is the coordinate,
 u_1 is the velocity,
 u_2 is the velocity,
 t is the time.

By removing the filling factor θ from the extended Reynolds equation (1) we get the basic version of the Reynolds equation:

$$\frac{\partial}{\partial x} \left(\frac{1}{12\eta} h^3 \frac{\partial p}{\partial x} \right) + \frac{\partial}{\partial z} \left(\frac{1}{12\eta} h^3 \frac{\partial p}{\partial z} \right) = \frac{u_1 + u_2}{2} \frac{\partial h}{\partial x} + \frac{\partial h}{\partial t} \quad (2)$$

where x is the coordinate,
 η is the dynamic viscosity,
 h is the clearance,
 p is the pressure,
 z is the coordinate,
 u_1 is the velocity,
 u_2 is the velocity,
 t is the time.

The extended Reynolds equation (1) is solved for the pressure p in the lubrication region and the filling factor θ in the cavitation region. The filling factor serves to model the cavitation effects and is defined as the fraction of volume filled with oil to the total volume. (Bukovnik *et al.* 2006)

The thermoelastohydrodynamic method solves the extended Reynolds equation together with the energy equation of the oil film. The energy equation takes into consideration heat convection in all directions, heat conduction in the radial direction, compression and viscous heating. Within the Reynolds equation, both the oil viscosity and density vary in three dimensions of space. (Bukovnik *et al.* 2006)

The deformation of the bearing shell as a result of oil film pressure is ignored in the hydrodynamic method, but is taken into account in the elastohydrodynamic and thermoelastohydrodynamic methods. The shell deformation is considered by the following linear dynamic equation system obtained from the finite element method (FEM) discretization of the shell (Bukovnik *et al.* 2006):

$$M\ddot{u}_B + D\dot{u}_B + Ku_B = f \quad (3)$$

where M is the mass matrix,
 u_B is the shell deformation,
 D is the damping matrix,
 K is the stiffness matrix,
 f is the nodal force acting on the oil film.

In the hydrodynamic, elastohydrodynamic and thermoelastohydrodynamic methods, the motion of the journal is determined by the following equation (Bukovnik *et al.* 2006):

$$m\ddot{x}_j = f_j + f_A \quad (4)$$

where m is the journal mass,
 x_j is the journal position,
 f_j is the oil film force acting on the journal,
 f_A is the outer force acting on the journal.

An illustrative comparison of different bearing simulation methods based on the solution of the Reynolds equation was made by Bukovnik *et al.* (2006). They compared the classical methods by Holland and Butenschoen with more modern HD, EHD and TEHD methods for simulating the non-stationary response of journal bearings in combustion engines. The comparison included the following bearing parameters: peak oil film pressure, minimum oil film thickness and volume flow of the oil. The results of the study showed that the elasticity of the shell ultimately has to be considered for an accurate modelling of the bearing behaviour.

There have also been other kinds of mathematical studies made in relation to hydrodynamic journal bearings. For example, Moreno Nicolás *et al.* (2007) studied the solution of temperature fields in hydrodynamic bearings by a numerical network method. Sun and Changlin (2004) calculated the distribution of the oil film pressure of a

misaligned journal bearing. In a study of the nonlinear dynamic coefficients in plain journal bearings, Meruane and Pascual (2008) used a computational fluid dynamic model of a bearing operating under high dynamic loading conditions. Turaga *et al.* (1999) used a special model to study the effect of surface roughness on the load carrying capacity of hydrodynamic journal bearings.

3 Materials

3.1 General

A versatile bearing test rig, designed especially for the tribological research into crankshaft bearings of internal combustion engines, was the main test apparatus used for the experiments in this study. In the test rig, different test specimens (bearings, shafts and housings) were tested and lubricants of different types were used for lubrication. The test rig, bearings, shafts, housings and lubricating oils are described below.

3.2 Test rig

3.2.1 Main design

The test rig was developed by a research team. The Author was in charge of the main design, construction and operation of the test rig. The main design of the bearing test rig was simple, spacious and based on the use of replaceable components. The bearing test rig consisted of a frame, bearing unit and loading, drive, lubrication, control and measuring systems all of which are described below. A view of the three-dimensional model of the bearing test rig is shown in Figure 3-1. The main design of the bearing test rig was influenced by an advanced solution presented by Berg (1996).

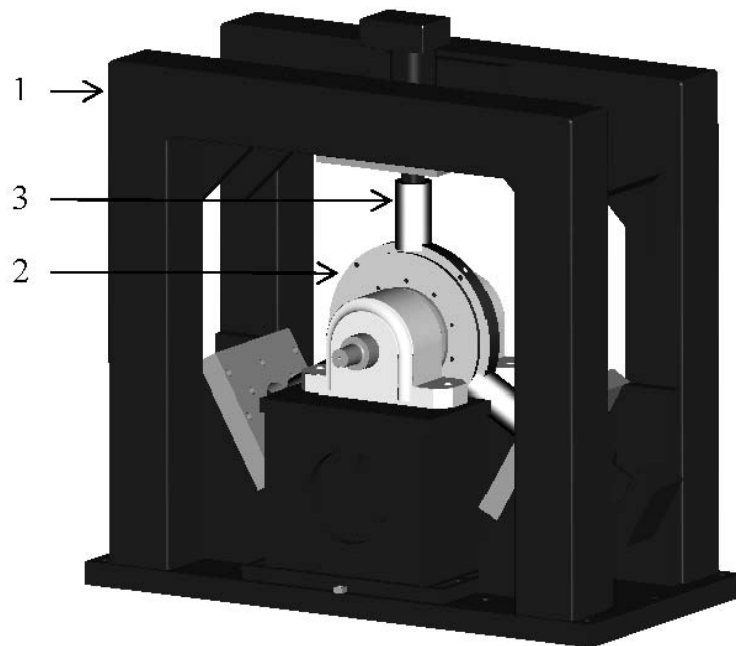


Figure 3-1. Versatile bearing test rig. A view of the three-dimensional model including the frame (1), bearing unit (2) and load cylinders (3).

3.2.2 Frame

The frame of the bearing test rig consisted of a coarse base plate and two firm angular beams with housings for the load cylinders. The width, height and length of the frame were circa 1.2, 1.1 and 0.6 m, respectively. The frame was firm enough to resist disturbing yield and resonance phenomena in its nominal operating range. The strength of the frame was studied mathematically by Lappeenranta University of Technology, using the finite element method (FEM). According the above-mentioned study, the expected maximum stress in the frame was 90 MPa at 120 % load and the lowest natural oscillation frequency of the frame was 91 Hz (see Appendix A).

3.2.3 Bearing unit

The bearing unit included the bearing, a housing with seal ring covers, a force ring (surrounding the housing) with two heating resistors, shaft, supporting bearings (with housings and movable stands) and an alignment arm. The nominal output of the heating resistors was 1 kW. The supporting bearings were spherical roller bearings operating with negligible bearing play. The nominal kinematic rotational speed, nominal thermal rotational speed and nominal dynamic load-carrying capacity of the supporting bearings were 4000 1/min, 3200 1/min and 455 kN, respectively. There was a slide rail on the base plate of the frame to guide the movable stands of the supporting bearings. The alignment arm connecting the force ring to the frame was used for positioning. The alignment arm allowed small horizontal, vertical and rotational motions between the force ring and the frame.

Due to the spacious main design of the bearing test rig, it has been possible to carry out experiments with bearings and shafts of different types and sizes. An exploded view of the bearing unit is shown in Figure 3-2. An assembled bearing unit is shown in Figure 3-3.

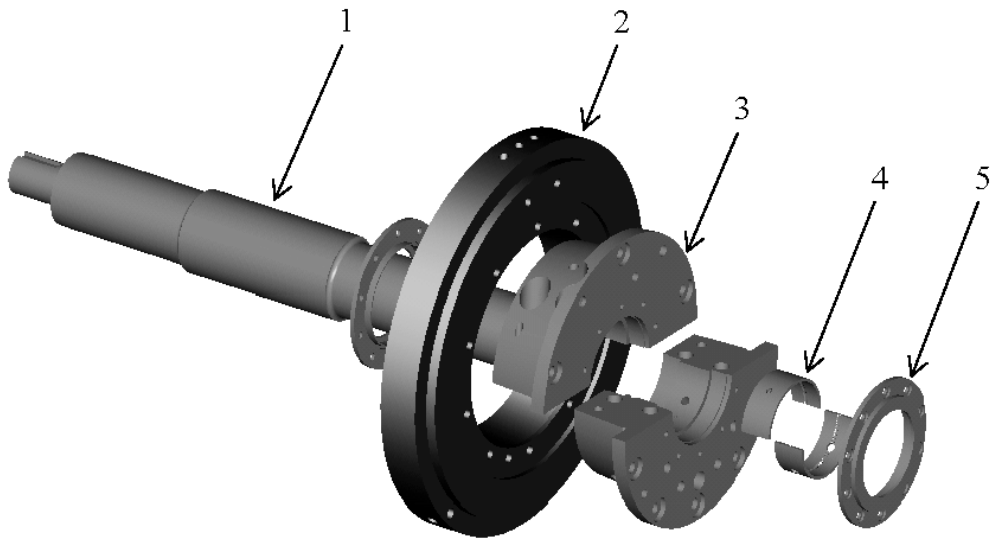


Figure 3-2. An exploded view of the bearing unit including the shaft (1), force ring (2) and housing (3) with the bearing (4) and seal ring covers (5).

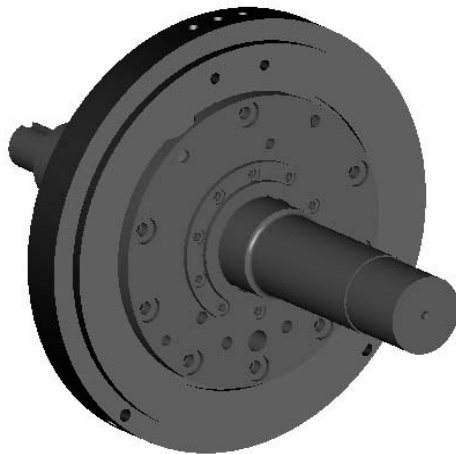


Figure 3-3. Assembled bearing unit (front view without the supporting bearings).

3.2.4 Loading system

The loading system generated the load on the bearing. The main components of the loading system were three servo valve controlled hydraulic cylinders and a hydraulic plant unit. Commissioning tests and a trial run of the loading system were carried out by the supplier of the hydraulics, Helsinki University of Technology and VTT Technical Research Centre of Finland. Results from the trial run are presented in Appendix B. The diameter of the cylinder piston, the maximum stroke length and the maximum hydraulic fluid pressure were 80 mm, 50 mm and 245 bar, respectively. The cylinders pushed the force ring, housing and bearing against the shaft, thus producing the bearing load. The loading system was able to generate both static and dynamic bearing loads, for example load cycles resembling those in a running engine. For static loads, the load range of the bearing test rig was 0 to 100 kN. For dynamic loads, the load range was narrower. It was possible to vary the bearing load both continuously and gradually. With gradual load control, the minimum load step and the maximum load step were ± 0.1 kN and ± 100 kN, respectively. Three hydraulic cylinders of the loading system are shown in Figure 3-4.

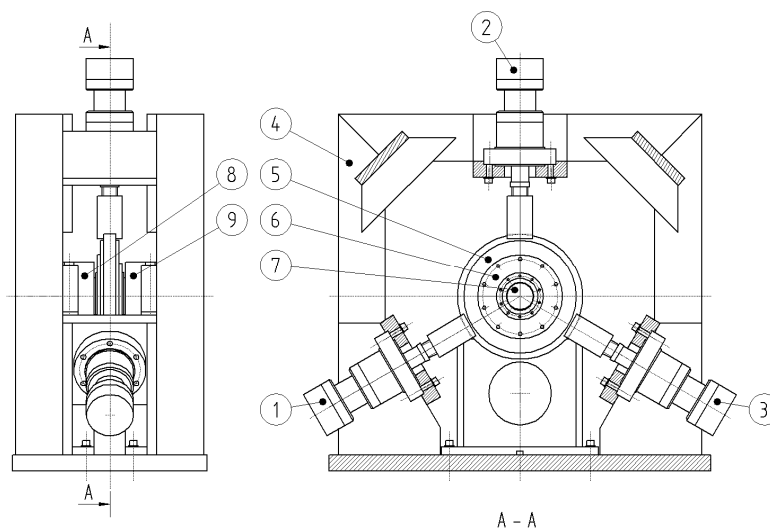


Figure 3-4. Three hydraulic cylinders (1, 2 and 3) of the loading system. The cylinders were placed in the frame (4) and they pushed the force ring (5), housing (6) and bearing against the shaft (7) with the supporting bearings (8 and 9).

3.2.5 Drive system

The drive system drove the shaft (see Figure 3-5). The drive system consisted of a frequency modulator with a control unit, three-phase motor with a pulley, drive shaft with a pulley and pulse sensor, poly-V belt connecting the pulleys, coupling (with an integrated torque transmitter) connecting the shafts and two roller bearings (supporting the drive shaft) with housings and stands. The nominal output of the three-phase motor was 11 kW. The rotational speed of the shafts was variable and controlled by the frequency modulator. The rotational speed range was 0 to 3000 1/min. The sliding speed was determined by the rotational speed of the shaft and the diameter of the bearing. In typical experiments with 85 mm diameter bearings, the sliding speed range was 0 to 13.4 m/s. The sliding speed level was continuously controlled with an accuracy of ± 0.1 m/s. It was possible to freely choose the sliding direction (*i.e.*, the direction in which the shaft rotates).

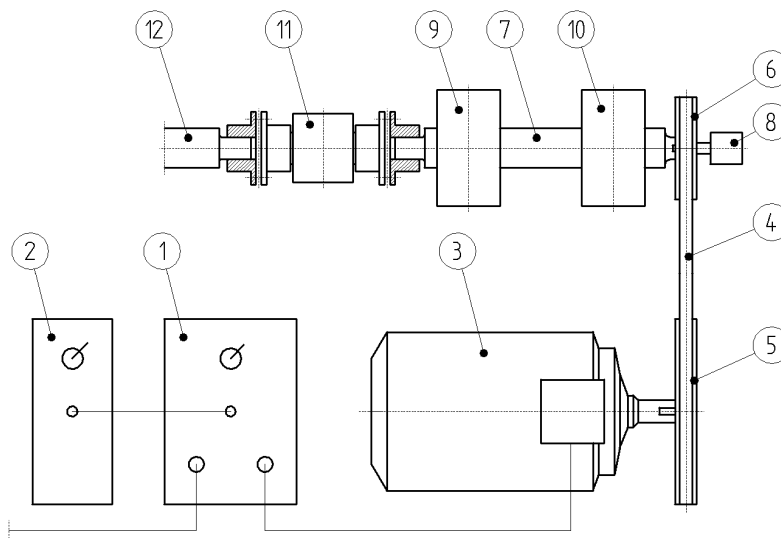


Figure 3-5. Drive system. The frequency modulator (1) with a control unit (2) controlled the three-phase motor (3). The poly-V belt (4) connected the pulleys (5 and 6). The drive shaft (7) with a pulse sensor (8) was supported by two roller bearings (9 and 10). The coupling (11), with an integrated torque transmitter, connected the drive shaft to the shaft (12).

3.2.6 Lubrication system

The lubrication system supplied the lubricating oil for the bearing. The main components of the lubrication system were an oil pump, oil tank, filters and heating devices with thermostats. There were two possible options for feeding the oil into the bearing: through the housing and the oil holes in the bearing or through the rotating union and the shaft. The inlet pressure range was 0 to 10 bar. The inlet pressure was controlled by a manually operated valve with an accuracy of ± 0.2 bar. The inlet temperature range was from room temperature to 100 °C. The inlet temperature level was controlled automatically with an accuracy of ± 3 °C. The maximum rotational speed, oil temperature and oil pressure of the rotating union were 3500 1/min, 120 °C and 70 bar, respectively. A schematic overview of the lubrication system is shown in Figure 3-6.

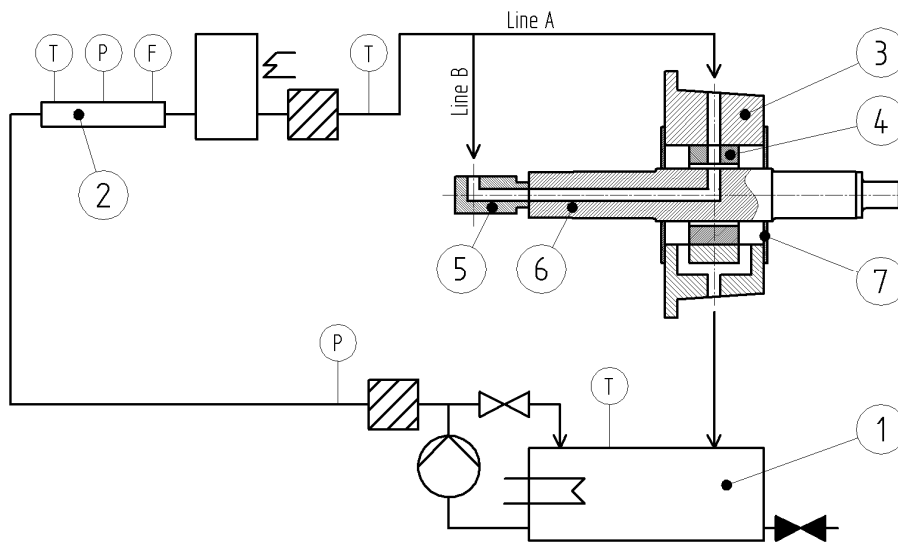


Figure 3-6. Schematic overview of the lubrication system. The lubricating oil was pumped from the oil tank (1) into the flow meter unit (2). Line A was used to supply oil through the housing (3) and the oil holes in the bearing (4). Line B was used to supply oil through the rotating union (5) and the shaft (6) with radial oil-feeding holes. The housing had seal ring covers (7).

3.2.7 Control system

The control system controlled the bearing load generated by the hydraulic cylinders of the loading system. The main components of the control system were a controlling computer with a signal processor card and an analogue output board, along with analogue proportional-integral-derivative (PID) amplifiers, anti-aliasing filters, three two-stage servo directional valves with analogue amplifier modules, six pressure transmitters, a pulse sensor and pulse counter electronics. A schematic overview of the control system is shown in Figure 3-7.

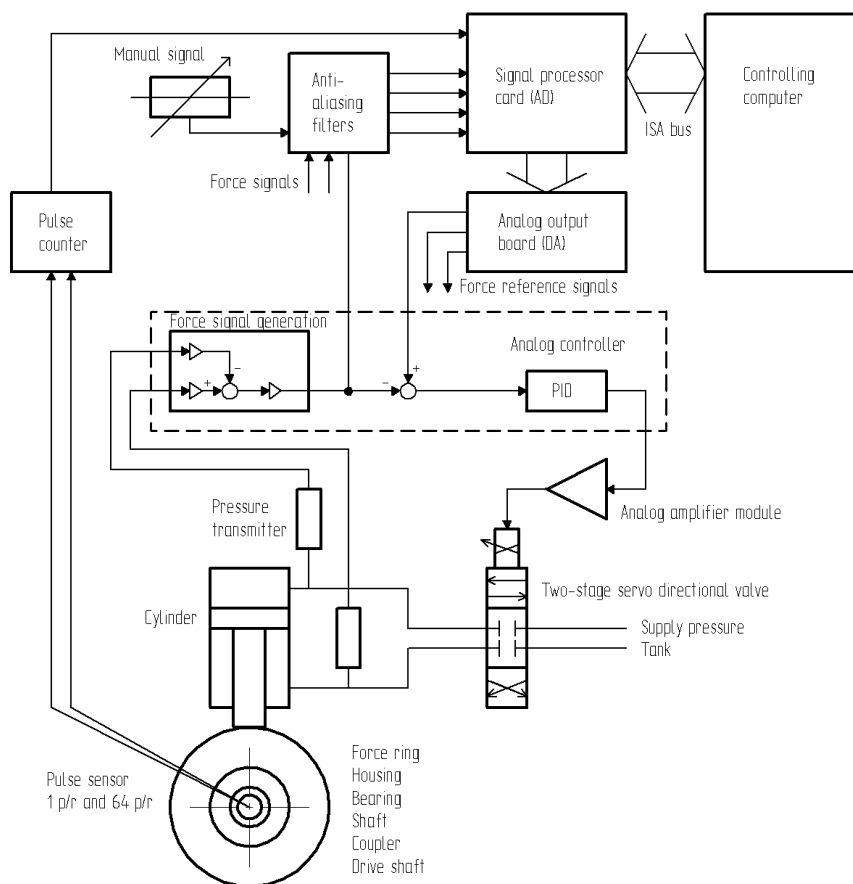


Figure 3-7. Schematic overview of the control system.

The commands for the signal processor card were sent by the controlling computer using a command language and user interface. Most of the tasks of the signal processor card were coded with a common program language and compiled for the card using its custom command support software. These commands were downloaded to the signal processor card via the user interface. Some parameter values were included in these custom commands and they were set (if necessary) during the operation via the user interface. The signal processor card was used for generating reference signals for the analogue PID amplifiers, which controlled the forces of the cylinders. The force signals for the PID amplifiers were generated with analogue electronics from cylinder pressure measurements. These force signals were also read (if necessary) by the signal processor card and used for digital force control (instead of analogue PID-control). The pulse sensor and pulse counter outputs were used by the signal processor to produce the cylinder forces, which were synchronised with the rotation of the shaft. The synchronised operation of the cylinders made it possible to generate various bearing load patterns, such as static, sine wave, impulse and rotating loads.

An illustrative example of the synchronised operation of the cylinders was the rotating load. With this load, the hydraulic cylinders number 1, 2 and 3 generated the cylinder forces F_1 , F_2 and F_3 respectively. The cylinder forces varied in a wave-like manner as functions of the angle of rotation. The cylinder forces had certain given amplitudes and phase differences. For example, the cylinder force F_1 was determined by the following equation:

$$|F_1| = A_1 + A_1 \sin(\alpha + \phi_1) \quad (5)$$

where A_1 is the amplitude (of the cylinder number 1),
 α is the angle of rotation,
 ϕ_1 is the phase difference (of the cylinder number 1).

The resultant of the cylinder forces was called load F , which was a static load revolving around the bearing and pushing it against the shaft. This resultant, or load F , was determined by the following vector equation:

$$F = F_1 + F_2 + F_3 = \sum_{i=1}^3 F_{xi} + \sum_{i=1}^3 F_{yi} \quad (6)$$

where F_1 is the cylinder force number 1,
 F_2 is the cylinder force number 2,
 F_3 is the cylinder force number 3,
 F_{xi} is the horizontal component of the cylinder force number i ,
 F_{yi} is the vertical component of the cylinder force number i .

The bearing load L was the counterforce of load F . The cylinder forces and their resultant are presented in Figure 3-8. The cylinder forces and their resultant, as functions of the angle of rotation with a rotating load of 10 kN, are presented in Figure 3-9. The horizontal and vertical components of the resultant of the cylinder forces during one revolution of the shaft are presented in Figure 3-10.

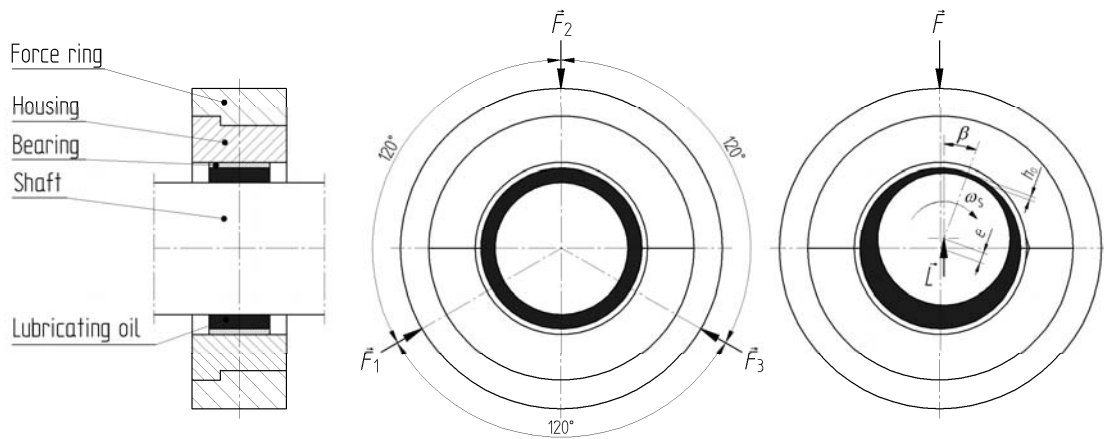


Figure 3-8. Cylinder forces F_1 , F_2 and F_3 pushing the bearing against the shaft (in the middle), and the resultant, load F (right). The bearing load L was the counterforce of load F . The shaft rotated at the angular velocity ω_s . The bearing load and rotation caused the eccentricity e .

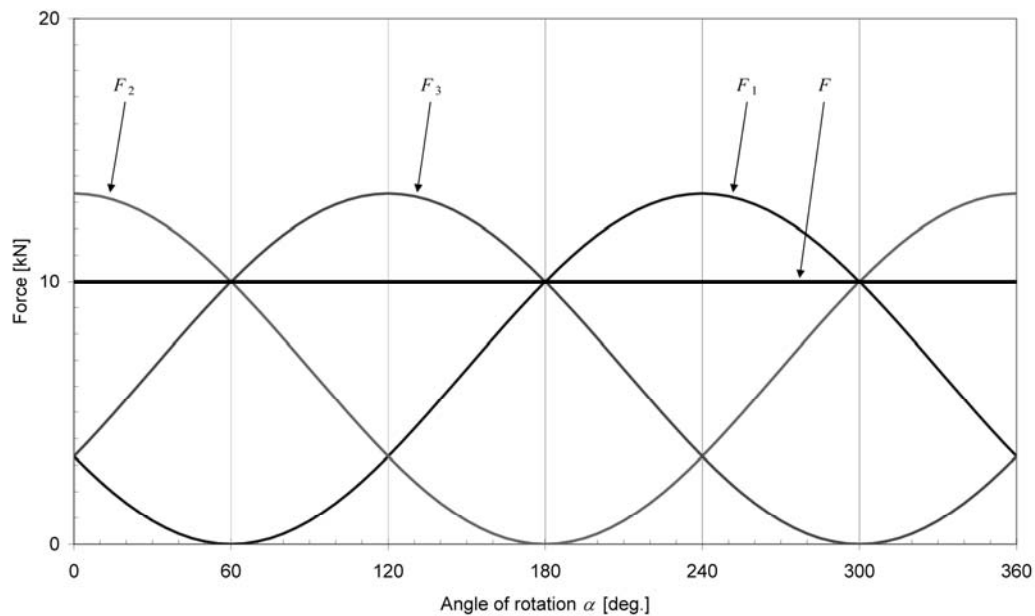


Figure 3-9. Cylinder forces (F_1 , F_2 and F_3) and the resultant (F) as functions of the angle of rotation α with a rotating load of 10 kN.

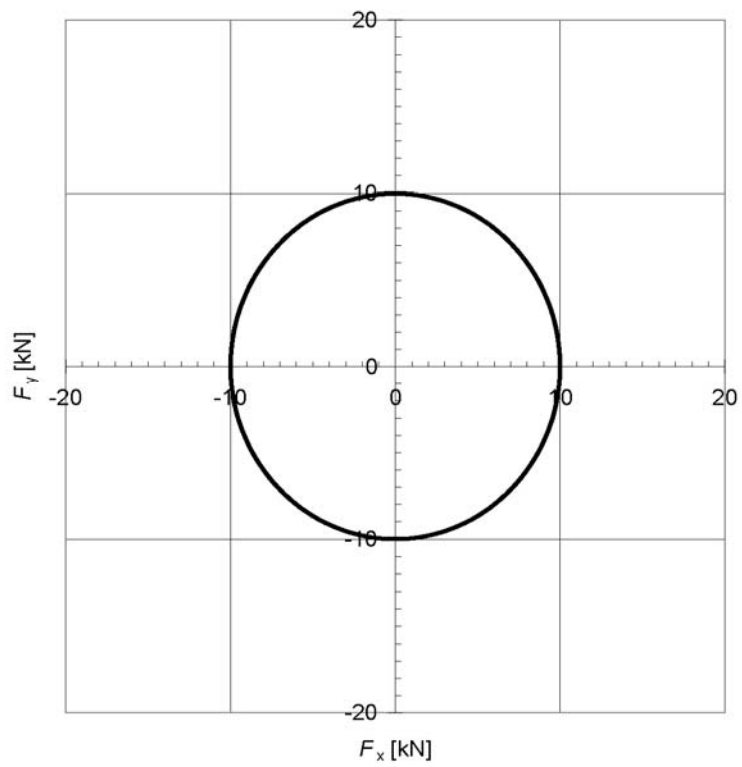


Figure 3-10. Horizontal component of the resultant F_x and vertical component of the resultant F_y with a rotating load of 10 kN during one revolution of the shaft.

3.2.8 Measuring system

The measuring system measured and recorded the data. A measuring computer, signal processing modules and various measuring devices were the main components of this measuring system. The measuring computer was equipped with a measurement card and measurement program. The measuring devices used in this study are shown in Table 3-1. The main devices measuring the operating conditions of the bearing were located in the housings. Different measuring device combinations were used with different housings. A schematic view of the measuring devices in the first housing (housing HS, see Chapter 3.5) is presented in Figure 3-11. A schematic view of the measuring devices in the second housing (housing HO, see Chapter 3.5) is presented in Figure 3-12.

Table 3-1. Measuring devices.

Device(s) and their quantity	Variable(s) measured by the device(s)
Pressure transmitters (6)	Hydraulic pressure in the load cylinders
Optical pressure sensors (1 or 3)	Oil film pressure
Pulse sensor	Angle of rotation of the shaft
Torque and rotational speed transmitter	1) Total torque of the bearings, 2) Rotational speed of the shaft
Pressure transmitter	Inlet pressure
Volume flow meter	Volume flow
Type K thermocouple	Inlet temperature (in the flow unit)
Type K thermocouple	Inlet temperature
Type K thermocouple	Outlet temperature
Type K thermocouple	Temperature of the housing
Type K thermocouples (1 or 2)	Operating temperature of the bearing
Type K thermocouples (2)	Operating temperature of supporting bearings
Type K thermocouple	Outer temperature of the oil filter
Type K thermocouple	Oil temperature in the oil tank
Type K thermocouple	Ambient temperature

Thermocouples to measure operating temperature

The operating temperature of the bearing was measured by one or two thermocouples in the housing. These thermocouples were located in bushings with springs (see Figure 3-13). The measurement points were located on the outer surface of the upper bearing shell. It was assumed that, under typical operating conditions, the point of maximum bearing temperature was close to the temperature measurement points.

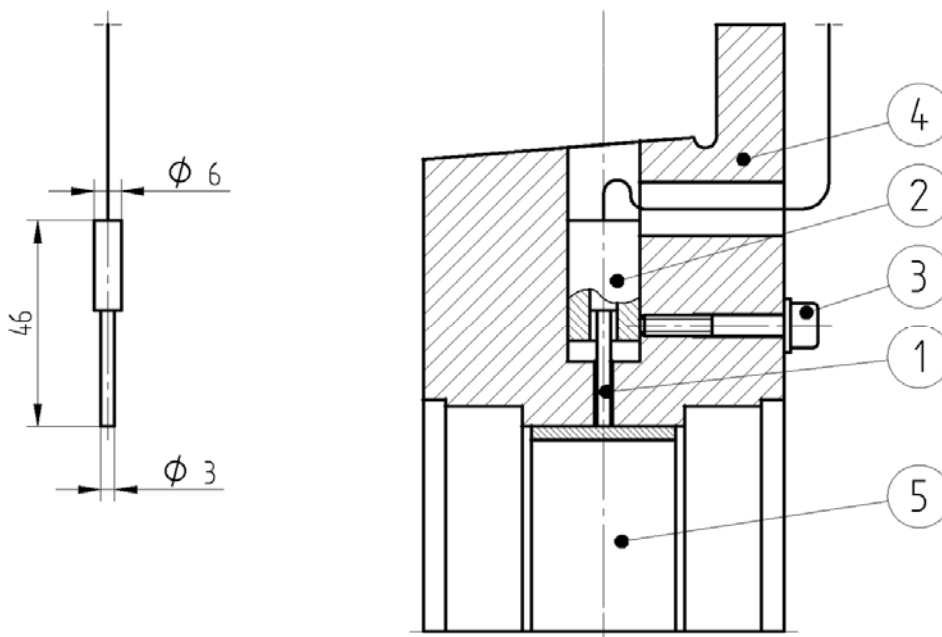


Figure 3-13. Thermocouple (1) in the bushing (2) with springs. A screw (3) locked the bushing in the housing (4). The measurement point was on the upper surface of the bearing shell (5).

Optical pressure sensors to measure oil film pressure

The optical pressure sensors (see Figure 3-14) measuring the oil film pressure were located in the housing HO. The measurement points were located on the outer surface of the upper bearing shell. For each of the measurement points, a cavity with a measurement membrane was made in the bearing shell. Some additional measuring devices and accessories were used for the optical pressure sensors. Details related to the optical pressure sensors are presented in Chapter 4.2.5.

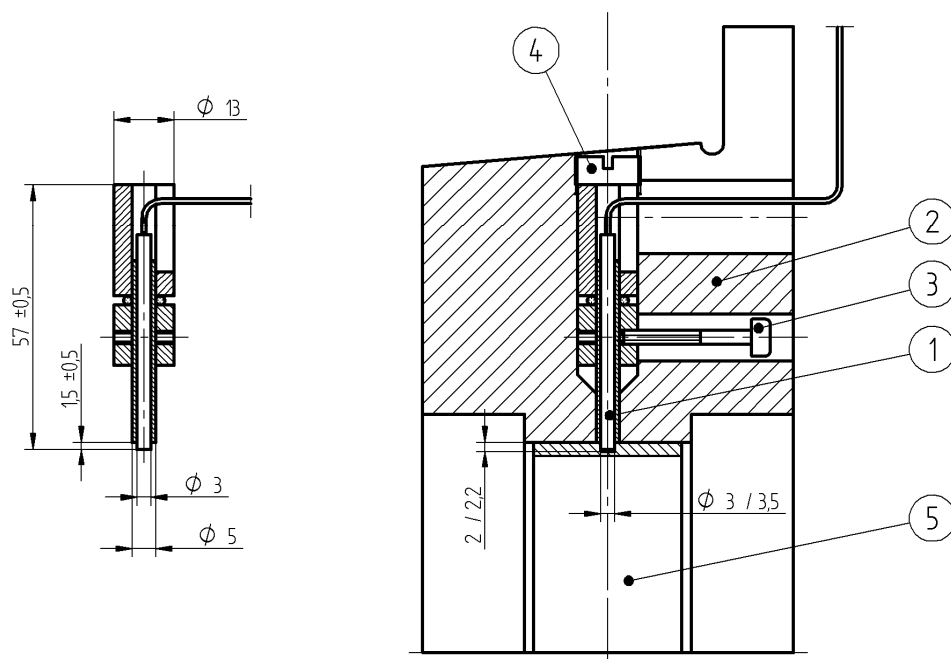


Figure 3-14. Optical pressure sensor (1) with its protection sleeves in the housing HO (2). A screw (3) locked the supporting tube with the sensor head in the lower protection sleeve. There was a rubber ring between the protection sleeves. Another screw (4) locked the sensor in the axial direction. A cavity was made in the bearing shell (5) for the sensor.

Pressure transmitters in the load cylinders

A total of six piezoresistive pressure transmitters (two pieces per cylinder) were used to measure the oil pressure pushing the pistons in the cylinders, in order to determine the bearing load generated by the hydraulic load cylinders. The pressure transmitters had sensor cells with a thin-film strain gauge on a steel membrane. According to the

specifications, the pressure transmitter had the following characteristics: a measuring range of 0 to 250 bar; its dispersion, the error in the linearity and the error caused by the hysteresis were below 0.3 % of the full scale; the error in repeatability was below 0.05 % of the full scale and the response time was below 0.5 ms. The estimated relative error in the bearing load that was determined from cylinder pressure data was ± 2 % for static loads and ± 5 % for dynamic loads.

Torque and rotational speed transmitter

The torque and rotational speed transmitter measured the total torque (the sum of the torques caused by friction in the bearing and supporting bearings) and the rotational speed of the shaft. The torque and rotational speed transmitter was located between the shaft and the drive shaft (see Figure 3-15). The torque transmitter had the following characteristics: its measuring range was 0 to 200 Nm, its rotational speed range was 0 to 4000 1/min and its maximum measuring frequency was 15 kHz. The torque and rotational speed transmitter was calibrated using a torque arm and dead weights.

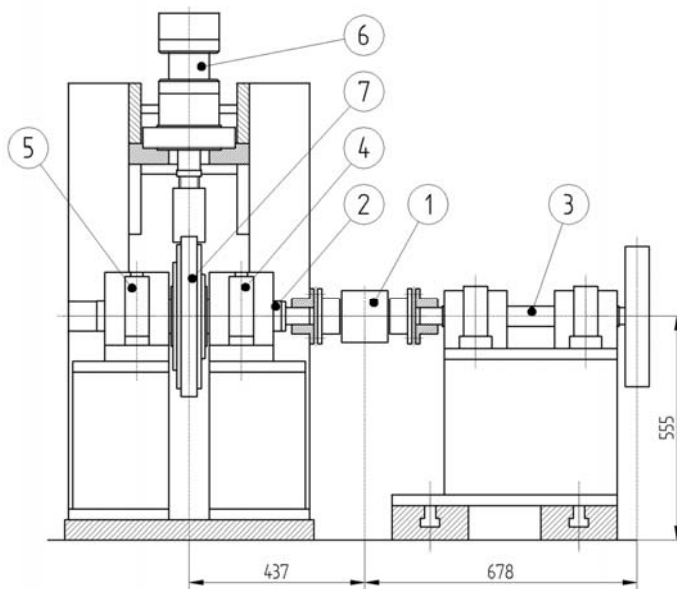


Figure 3-15. Torque and rotational speed transmitter (1) between the shaft (2) and drive shaft (3) with supporting bearings (4 and 5). The hydraulic cylinder (6) pushed the force ring (7), housing and bearing against the shaft.

Measuring devices used to determine the heat flow through the housing

The devices used to determine the heat flow through the housing were the following: 1) A thermocouple on the back of the bearing to measure the operating temperature of the bearing, 2) a thermocouple on the force ring to measure the temperature of the housing and 3) a thermocouple to measure the ambient temperature.

Measuring devices used to determine the heat flow transferred by the lubricating oil

The following devices were used to determine the heat flow transferred by the lubricating oil: 1) A thermocouple to measure the inlet temperature, 2) a thermocouple to measure the outlet temperature and 3) a volume flow meter to measure the volume flow of the lubricating oil. The volume flow meter was calibrated by using a measuring glass and a seconds counter.

Measuring devices used for control

The following devices were used for control: 1) A pressure transmitter to measure the inlet pressure, 2) a thermocouple to measure the inlet temperature in the flow unit, 3) two thermocouples to measure the operating temperature of the supporting bearings, 4) a thermocouple to measure the outer temperature of the oil filter, 5) a thermocouple to measure the oil temperature in the oil tank and 6) a pulse sensor to measure the angle of rotation of the shaft. The pulse sensor gave 64 pulses and one trigger pulse per revolution. Those pulses were used to synchronise the loading system.

Optional measuring devices

The test rig had some optional measuring devices that were not used in this study. However, they may be useful for further studies. A piezoresistive pressure and temperature transmitter (see Figure 3-16) has been used to measure oil film pressure and temperature. The transmitter was installed in the housing HS. The measuring range of the transmitter was from 0 to 1000 bar.

Two inductive distance sensors (see Figure 3-17) have been used to measure the distance between the bearing and the shaft. The distance sensors, with their protection sleeves, were installed in the housing HS. The measuring range of the distance sensor was 0 to 500 μm . The oil film thickness was calculated from the distance data combined with the geometry data.

Thin-film pressure sensors integrated in the sliding surface of the bearing (see Figure 3-18) have been used to measure the oil film pressure. It has been possible to place bearings with thin-film sensors both in the housing HS and HO. The thin-film sensors were made by Musashi Institute of Technology.

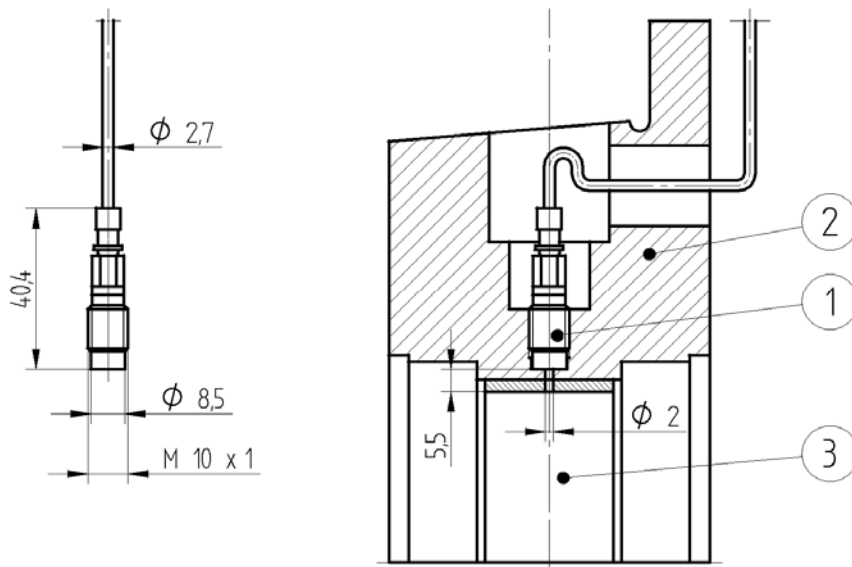


Figure 3-16. Pressure and temperature transmitter (1) in the housing HS (2). The measurement point was on the upper surface of the bearing shell (3).

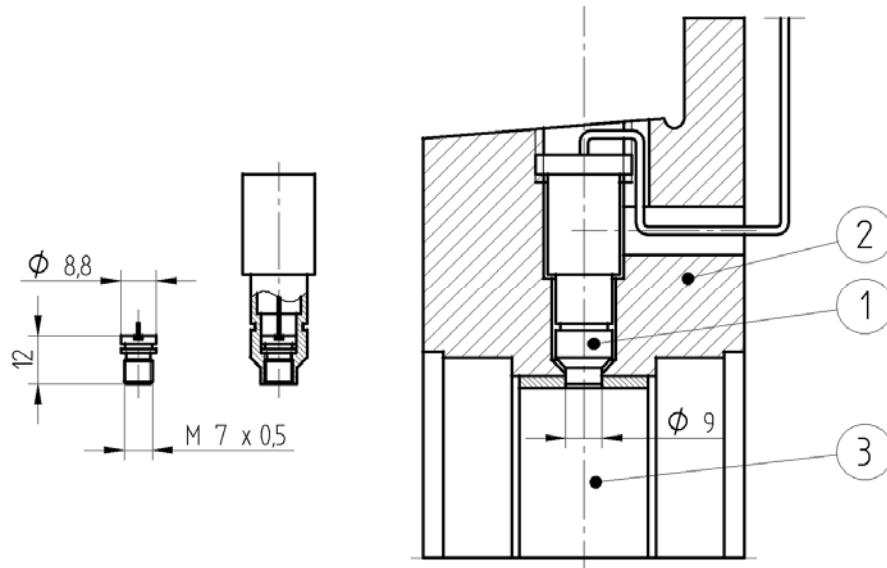


Figure 3-17. Distance sensor with a protection sleeve (1) in the housing HS (2). A bore was made in the bearing (3) for the distance sensor.

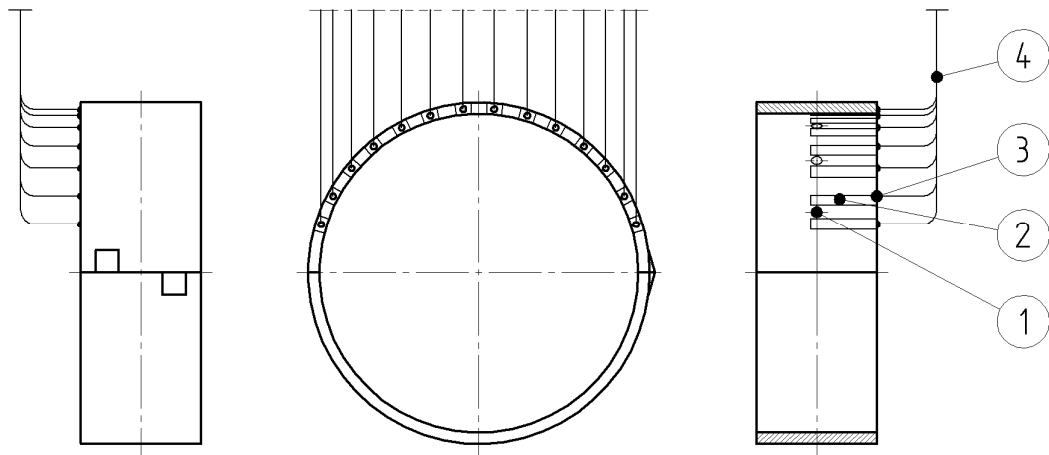


Figure 3-18. Thin-film pressure sensor with sensitive parts (1) and lead films (2) on the sliding surface of the bearing. The jointing points (3) of the wires (4) were on the front side of the bearing.

3.3 Bearings

Four different bearings, designated BS, BA, BE and BD, were used. All bearings had the same main design and the same nominal dimensions, based on a real engine bearing. The nominal outer diameter, inner diameter, width and wall thickness of the bearings were 91 mm, 85 mm, 32 mm and 3 mm, respectively. The bearings consisted of two half-round sleeves: the lower sleeve A and the upper sleeve B. The lower sleeve was either plain (non-grooved and without oil holes) or equipped with an oil groove and two oil holes. Different sensors were connected to the upper sleeve, which was non-grooved in all experiments.

The bearing BS (see Figure 3-19) was the main bearing of a high-speed six-cylinder four-stroke diesel engine with a displacement of 7.4 dm³. The rotational speed of the crankshaft of the above-mentioned engine is 1400 1/min at the nominal torque and 2200 1/min at the nominal output, according to the data by the engine manufacturer and Internal Combustion Engine Laboratory of Helsinki University of Technology, where the engine has been used for experimental research. The bearing shell was made of steel. The bearing alloy was lead bronze. The sliding surface was plated with lead indium. The lower sleeve of the bearing had an oil groove with a width of 4.3 mm and two oil holes with a diameter of 6 mm. The bearing was lubricated by oil supplied through the oil inlet hole in the lower sleeve and the oil outlet hole was not used. In the real engine, the main bearing is lubricated by a slightly different way; the oil is supplied through the upper sleeve with a groove and the lower sleeve carrying the main part of the bearing load is plain. The oil outflow runs partly into the oil outlet hole and partly into the oil sump.

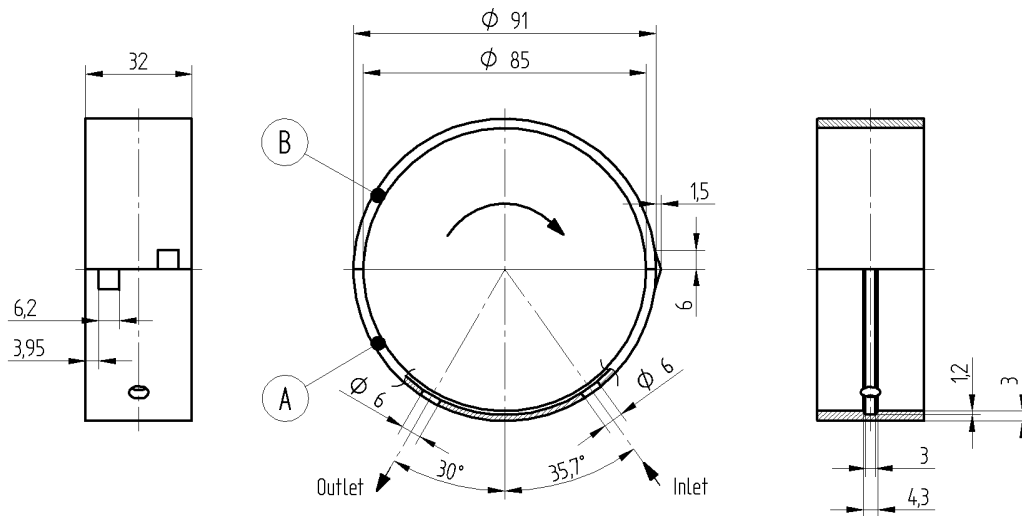


Figure 3-19. Bearing BS had an oil groove with a width of 4.3 mm in the lower sleeve (A). The lubricating oil was supplied through the oil inlet hole. The oil outlet hole was blocked. The lubricating oil ran from the bearing into two outlet channels in the housing. The upper sleeve (B) was plain.

The bearing BA (see Figure 3-20) was a special bearing. The bearing shell was made of steel. The bearing alloy was bronze. The sliding surface was plated with lead-tin. The bearing was non-grooved and lubricated by oil supplied through the shaft.

The bearing BE (see Figure 3-20) was a special bearing. The bearing shell was made of steel. The bearing alloy was aluminium. The bearing was non-grooved and lubricated by oil supplied through the shaft.

The bearing BD (see Figure 3-21) was a special bearing. The bearing shell was made of steel. The bearing alloy was lead-free bronze. The sliding surface was non-plated. The lower sleeve had an oil groove and two oil holes. The width of the oil groove was 8 mm and the oil holes had a diameter of 6 mm. Both oil holes were blocked. The bearing was lubricated by oil supplied through the shaft. Small cavities were made on the outer surface of the bearing for the optical pressure sensors.

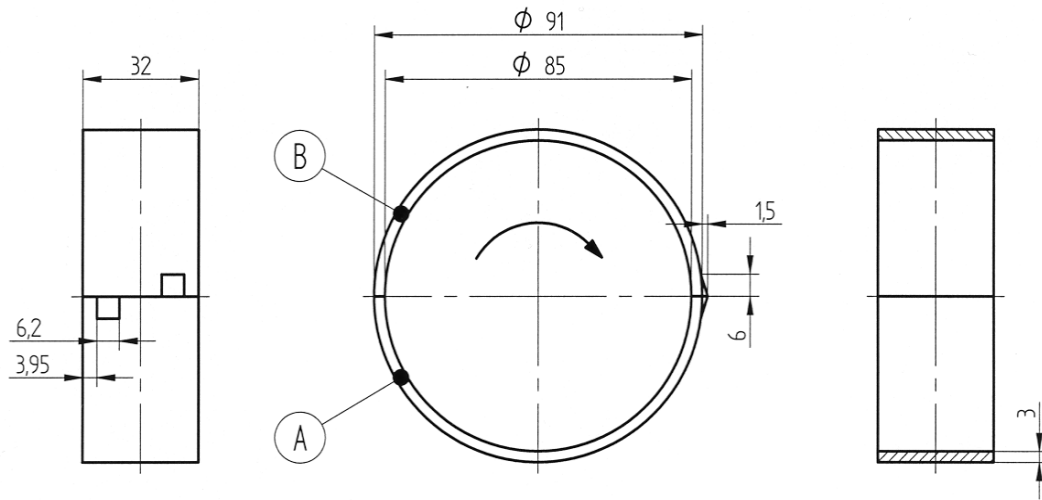


Figure 3-20. Bearings BA and BE were non-grooved. In the bearing BA, the bearing alloy was bronze. In the bearing BE, the bearing alloy was aluminium.

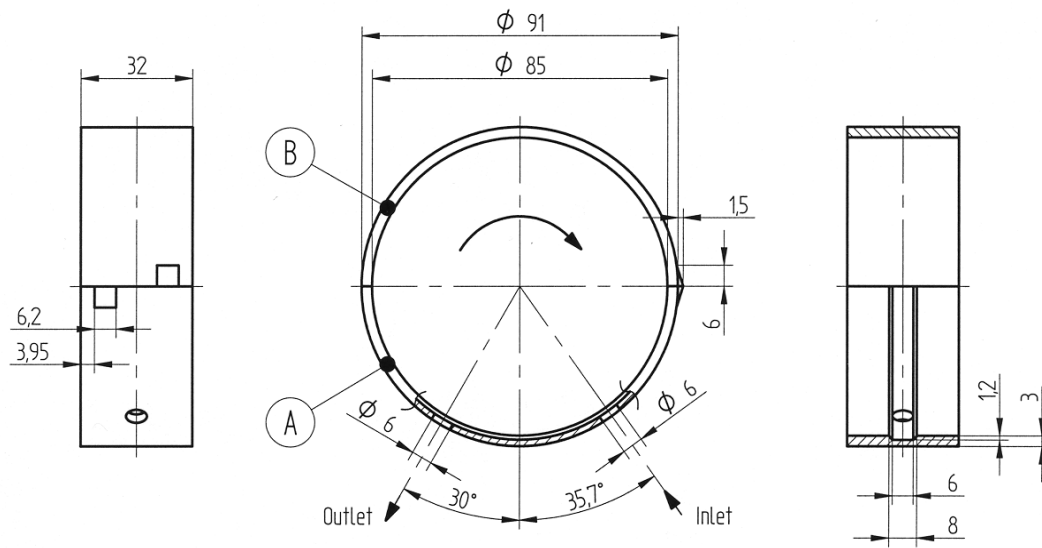


Figure 3-21. Bearing BD had an oil groove with a width of 8 mm in its lower sleeve. The lubricating oil was supplied through the shaft. The oil inlet and outlet holes were blocked. The lubricating oil ran from the bearing into two outlet channels in the housing.

3.5 Housings

Two different housings, designated HS and HO, were used. Both of the housings had the same main design and nominal dimensions. The nominal outer diameter, inner diameter and width of the housings were 270 mm, 91mm and 80 mm, respectively. The housings consisted of two half-round, thick-wall conical sleeves with flanges (see Figure 3-24). The sleeves were attached to each other by four screws with M16 threads and by two locating pins. The lower sleeve had lubrication channels. The upper sleeve had holes for different measuring devices. In typical experiments, the bearing load was carried mainly by the bearing shell in the upper sleeve. The housings were extremely rigid and practically could not be bent. The design of the housings made it possible to use realistic pre-tensioning caused by oversized bearing shells.

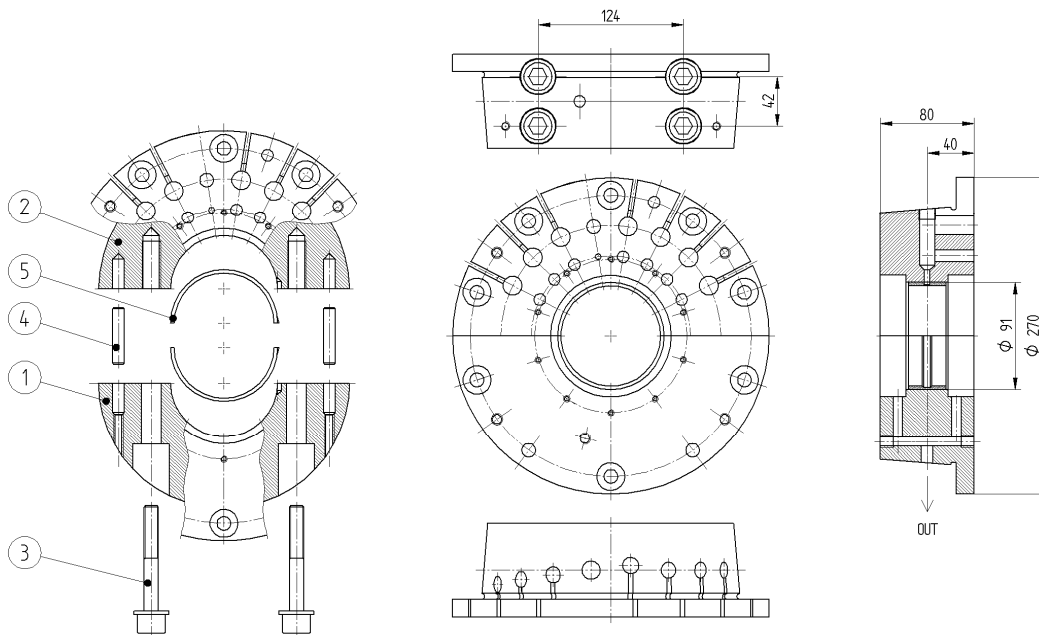


Figure 3-24. Housings consisting of two half-round sleeves (1 and 2) attached to each other with screws (3) and locating pins (4). Oversized bearing shells (5) caused realistic pre-tensioning.

In the lower sleeve of the housing HS (see Figure 3-25), there were oil inlet and outlet channels. In the upper sleeve, there were holes for two thermocouples, two distance sensors and one pressure and temperature transmitter.

In the lower sleeve of the housing HO (see Figure 3-26), there were oil outlet channels. In the upper sleeve, there were holes for seven optical pressure sensors and one thermocouple.

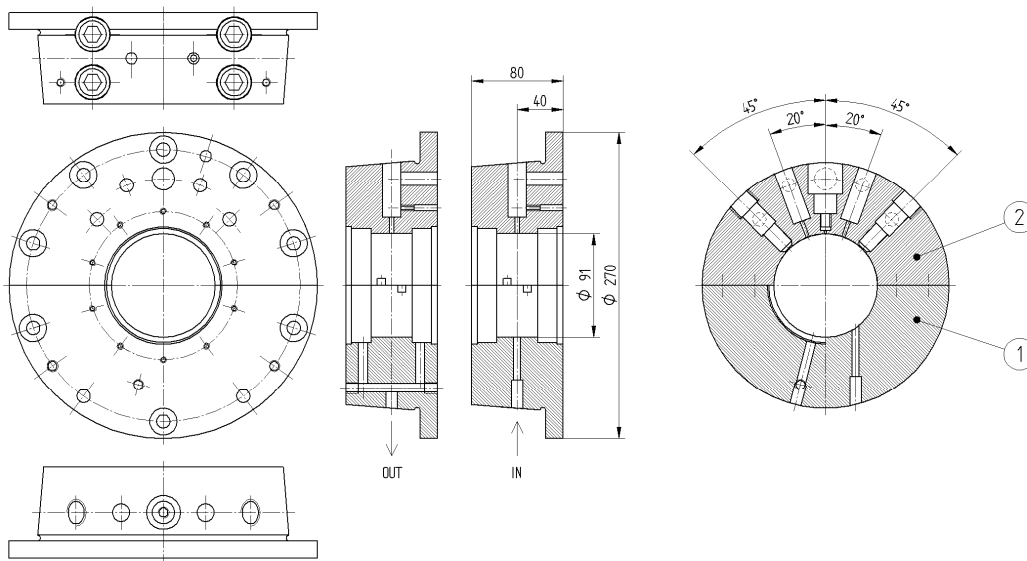


Figure 3-25. Housing HS had oil inlet and outlet channels in the lower sleeve (1). In the upper sleeve (2), there were holes for two thermocouples, two distance sensors and one pressure and temperature transmitter.

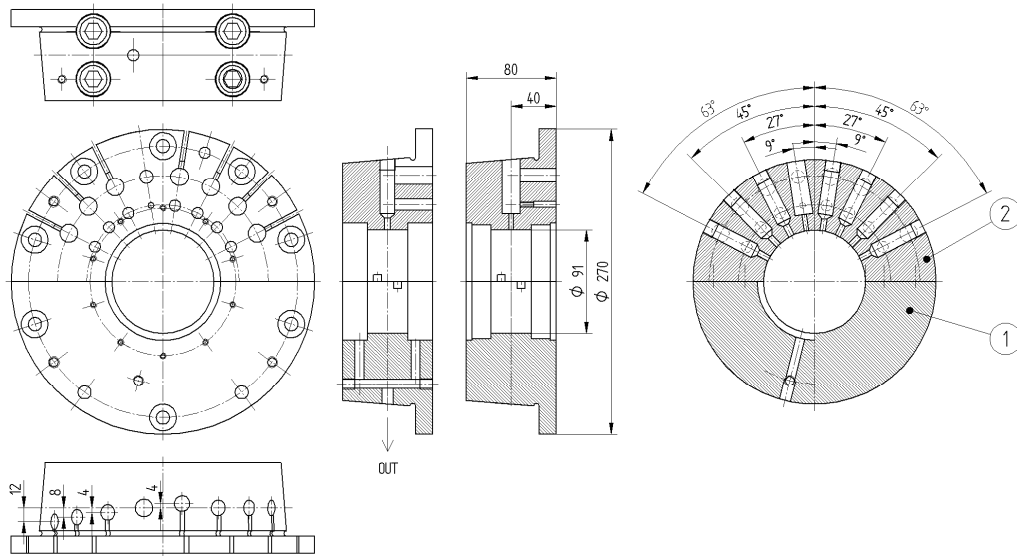


Figure 3-26. Housing HO had oil outlet channels in the lower sleeve (1). In the upper sleeve, there were holes for seven optical pressure sensors and one thermocouple.

3.6 Lubricating oils

Seven different lubricating oil types, designated A, B, C, D, E, F and G, were used. Oil A was a typical SAE 40 mono-grade engine lubricant with a relatively low viscosity index (101). Oils B, C, D, E and F were special oils with relatively high viscosity indices (138 to 149) and different additives. Oil G was a combined cylinder and crankcase lubricant designed for use in medium speed marine diesel engines operating on residual fuel. The oil was manufactured from mineral base oils, had an additive package and was blended as SAE 40. The density, kinematic viscosity, viscosity index and SAE classification of the lubricating oils are presented in Table 3-2.

For each oil change, the lubrication system was cleaned and new oil filters were installed. About 10 dm³ of new oil was used for cleaning. Finally, the oil tank was filled with 10 dm³ of new oil.

Table 3-2. Density, kinematic viscosity, viscosity index and SAE classification of the lubricating oils A, B, C, D, E, F and G. (Data by the lubricant manufacturers)

	Oil A	Oil B	Oil C	Oil D	Oil E	Oil F	Oil G
Density at 15 °C [kg/m ³]	n/a	872.4	888.9	876.2	856.1	856.2	916
Density at 20 °C [kg/m ³]	898.0	n/a	n/a	n/a	n/a	n/a	n/a
Kinematic viscosity at 40 °C [mm ² /s]	137.7	64.4	106.4	76.1	62.5	71.6	139
Kinematic viscosity at 100 °C [mm ² /s]	14.3	9.9	14.5	11.6	10.0	11.2	14.9
Viscosity index []	101	138	140	145	144	149	n/a
SAE classification	40	10W30	15W40	10W30	10W30	10W30	40

4 Methods

4.1 General

The operation of hydrodynamic journal bearings was studied using both experimental methods (test rig experiments) and mathematical methods (simulations and calculations).

The experimental studies were split up into three main sets of experiments, which were designated as range, friction and pressure experiment sets. In addition, the range experiment set was divided into two cases (Cases 1 and 2) and the pressure experiment set was divided in four cases (Cases 1, 2, 3 and 4). The order used in this work to present the different sets of experiments and cases roughly matches the chronology of the experimental studies. The test material, lubricating oil supply and test run matrices used in the different sets of experiments and cases are presented in Chapter 4.2.6.

The range experiment set was used to study the operating ranges of hydrodynamic journal bearings. The aim of the study was to determine the operating range and the main factors influencing its width. Isotherm mapping (see Chapter 4.2.1) was used as the main test method in the test rig experiments. Two different bearing types and two different bearing clearances were used to evaluate the test method. The bearings were non-grooved (or plain). The results from the range experiment set were used in the planning and execution of further sets of experiments.

The friction experiment set was used to study the friction loss that influenced the width of the operating range of the hydrodynamic journal bearing. Heat flow analysis (see Chapter 4.2.2) was used as the main test method in the test rig experiments. Six different oil types with different densities and viscosities were used to evaluate the test method. To improve lubrication, the bearing had an oil groove in the lower shell. The

results from the friction experiment set were used to support the analysis of the results from the other sets of experiments.

The pressure experiment set was used to study the oil film pressure influencing the width of the operating range of the hydrodynamic journal bearing. Optical pressure measurement (see Chapter 4.2.5) was used as the main test method in the test rig experiments and newly developed optical pressure sensors (available only in these latest experiments) were used to measure the oil film pressure. To evaluate the test method, the pressure measurements were carried out at different bearing load and sliding speed levels, with two different bearing load patterns, close to the expected limits of the operating range of the bearing. To improve lubrication, the bearing had an oil groove in the lower shell. The results from the pressure experiment set were used to support the analysis of the results from the other sets of experiments.

The mathematical studies consisted of simulations by advanced simulation software (see Chapter 4.3) and calculations by common calculation methods. The mathematical studies were performed mainly to analyse the results from the experimental studies. Because the study of the oil film pressure in hydrodynamic journal bearings was the main aim of this work, the simulations were focused on the pressure experiment set. An instant analysis of the results from the sets of experiments to study range and friction was made using common calculations, as the simulation software was not available at the time. Later, the first case of the range experiment set was also analysed using the simulations and data from the calculations and simulations were briefly compared.

4.2 Test rig experiments

4.2.1 Determination of the operating range of journal bearings

For the design and validation of journal bearings for different machines and engines, it is essential to know the true or expected operating range of the bearings. The operating range of a bearing can be determined by experimental or mathematical means. In practice, regardless of the high efficiency and reliability of modern bearing calculations and simulations, it is usually necessary to verify the mathematical results by experimental means, that is, there is still a need for experimental studies related to the operating range of journal bearings.

The operating range of a journal bearing can be described as an area covering usable operating points at different levels of sliding speed u_s and specific load p_s (the bearing load L divided by the product of the diameter D and the width B). At all of the operating points in the operating range, the operation of the bearing must be safe, *i.e.* stable and controllable. Wear and other deformations of the sliding surface of the bearing should be at acceptable levels, the heat flows heating and cooling the bearing should be balanced and the operating temperature should be stable.

In principle, the limits of the operating range of journal bearings can be studied experimentally simply by increasing or decreasing the sliding speed or specific load until the operation of the bearing is no longer stable and controllable. However, in practice, determining the operating range is typically difficult. Firstly, if the sliding speed is varied in a wide range separately from the specific load, or *vice versa*, it causes a significant change in the operating temperature. This has an influence on the oil film thickness, friction loss and load-carrying capacity. Therefore, it is difficult to control the operation of the bearing. Secondly, journal bearings are typically sensitive to changes in

the sliding speed level. A small change in the sliding speed level causes a greater change in the operating temperature, which has a significant influence on the bearing's operation. Thirdly, journal bearings are not typically sensitive to changes in the specific load level. A small change in the specific load level causes a barely observable change in operating temperature. Therefore, it is difficult to observe the moment when the operation of the bearing transforms from stable to unstable. Finally, if the bearing's operating range limit is exceeded at high sliding speeds or specific loads, a seizure may occur and cause severe damage to the bearing and, thereby, disturb the experiments. Studies on seizures were reviewed by Wang (1997) and Dowell (2005) studied seizures experimentally.

To avoid the above-mentioned difficulties in the bearing experiments, an experimental method for determining the operating range of journal bearings was developed. The method is called isotherm mapping and it is based on the experimental determination of isotherms of the operating temperature of the bearing. The method was assumed to be workable and results from experiments that used this method were expected to be usable for the following reasons: 1) Typically, operating temperature is the best-known (or the only known) key operating parameter in the contact of the bearing, lubricant and shaft, 2) the operating temperature can usually be easily determined by common measuring arrangements and 3) operating temperature can generally be determined more accurately than other key operating parameters. In addition, it was assumed that determining isotherms would be an effective and illustrative way to find out how the bearing responds to changes in its operating conditions.

For the isotherm mapping, the test rig experiments were carried out by using a special test run procedure, in which the operation of the bearing was presumed to be predictable and safe. In the procedure, both the isotherms of the operating temperature and the limits of the operating range of the journal bearing were determined as functions of the sliding speed and specific load (see Figure 4-1).

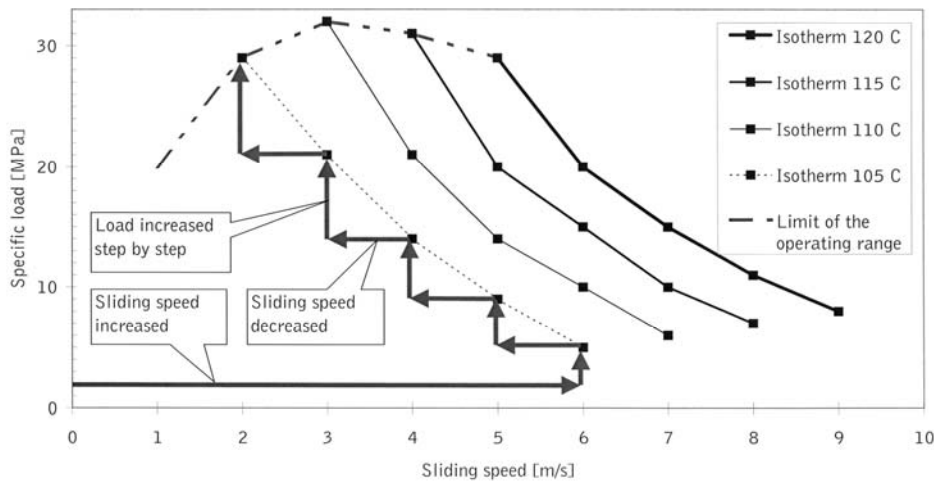


Figure 4-1. Test run procedure used in the isotherm mapping. The results of the procedure are presented in a chart showing the isotherms of the operating temperature and the limit of the operating range. A fictional case.

The test run procedure consisted of different phases. In the first phase of the procedure, the specific load was set to a certain low level (for example 2 MPa) and the sliding speed was increased from zero to a certain medium level (for example 6 m/s). Because the bearings used in the study came from a real engine (as mentioned in Chapter 3.3), the specific load and sliding speed used in this phase were estimated by common calculations from the engine data (see Appendix C). Based on the calculation results, the following were assumed for test rig experiments with sufficiently lubricated bearings: 1) the sliding speed range of the bearing covers sliding speeds of 6 to 10 m/s, 2) the sliding speeds close to 6 m/s can be used safely as “medium speeds”, 3) the highest specific loads are above 8 MPa and 4) specific loads clearly below 8 MPa can be used safely as “low loads”.

After the first phase (as well after all other phases), it was essential to wait until the operating temperature of the bearing stabilised. Intervals also had to be left after all changes to the sliding speed and specific load levels during the procedure, in order to stabilise the operating temperature. Typically, the length of the interval was 5 to 20 minutes.

In the second phase, the specific load was increased gradually (for example, in steps of +1 MPa) until the required operating temperature level, or the first isotherm (for example 105 °C), was reached. In the third phase, the sliding speed was decreased (for example, in steps of –1 m/s). In the fourth phase, the specific load was increased gradually until the required operating temperature level (in this case 105 °C) was reached again. At this stage, two operating points on the isotherm were known and it was possible to roughly predict the trend of the isotherm. Based on this prediction, it was possible to estimate the sliding speed and specific load levels at the next operating point on the isotherm. This information was useful for the optimisation of the next sliding speed and specific load steps. The two last phases mentioned above were repeated (when applicable) until the limit of the operating range was reached.

At the limit of its operating range, the bearing operated in a labile way. For example, the torque and operating temperature started to increase rapidly and, if the load had not been decreased immediately and significantly, a seizure would have been imminent (see Figure 4-2). By observing the torque level continuously, it was possible to avoid unsafe operating conditions and, thereby, to avoid the seizure.

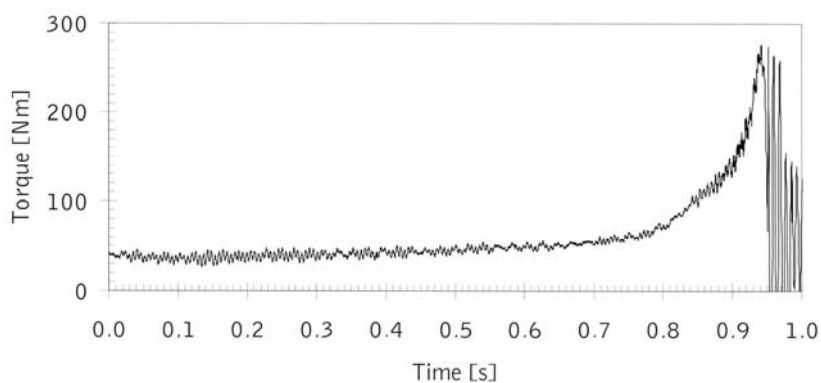


Figure 4-2. Torque during the seizure.

Next, the above-mentioned phases were repeated (to the appropriate extent) in order to determine new isotherms (for example 110 °C, 115 °C *etc.*) until the maximum operating temperature (for example 120 °C) was reached, *i.e.*, until it was not possible to

increase the operating temperature without losing the stability or controllability of the bearing. At this stage, it was possible to determine a part of the limit of the operating range as a function of the sliding speed and specific load. The limit of the operating range ran through the operating points at the ends of the isotherms. In addition, the limit ran (approximately) along the isotherm that described the maximum operating temperature level. Based on the known limit of the operating range, it was possible to roughly predict the trend of the limit in the operating range that was not covered. This information was useful in subsequent phases for determining the isotherms at low operating temperatures (for example, 100 °C, 95 °C *etc.*) below the first isotherm that was determined.

The results of the procedure were presented in a chart, or operating temperature map, showing the specific load on isotherms of the operating temperature and the limit of the operating range as functions of the sliding speed and specific load. The accuracy of the operating temperature map depended on the accuracy of the measurements, as well as on the magnitude of the speed and load steps used and on the chosen isotherm interval. According to practical experience gained from tests on crankshaft bearings of high-speed diesel engines, the useful magnitude of sliding speed steps, specific load steps and isotherm intervals are circa 1 m/s, 1 MPa and 5 °C respectively. Logically, it was possible to increase the accuracy of the operating temperature map by studying some critical operating points separately, for example at extremely low or high sliding speeds or those close to the highest isotherm of the operating temperature.

In order to specify the factors that influenced the limits of the operating range, the specific load and the minimum oil film thickness were determined (either directly from the measurement data or by mathematical means) as a function of the sliding speed on the isotherms of the operating temperature (see Figure 4-3). A curve fitting process, based on the least squares method, was used to find trend-lines for the variables as functions of the sliding speed at different temperatures. Simple trend-lines with high coefficients of determination (or R^2 values) were preferred.

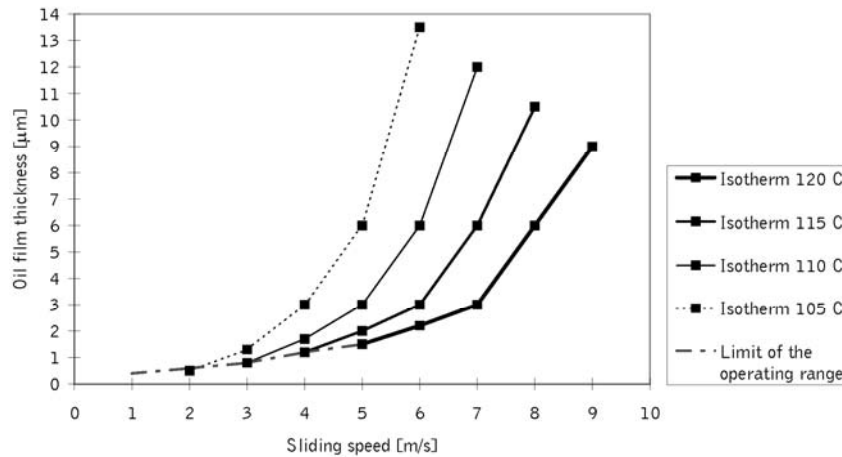


Figure 4-3. Oil film thickness on various isotherms of the operating temperature of the bearing. A fictional case.

Logarithmic trend-lines were chosen to describe the specific load p_s as a function of the sliding speed and temperature:

$$p_s = A(T)\text{Ln}(u_s) + B(T) \quad (7)$$

where A is the coefficient,
 T is the temperature,
 u_s is the sliding speed,
 B is the coefficient.

Polynomial trend-lines were chosen to present the coefficients A and B in the equation (7) as functions of the temperature T . The highest possible degree of polynomials was lower than the number of the experimentally determined isotherms. To achieve smooth trend-lines, the simplest polynomials of the first, second and third degree were preferred. For example, the following polynomial of the second degree was used for the coefficient A :

$$A(T) = \sum_{i=0}^2 a_i T^i \quad (8)$$

where a_i is the coefficient,
 T is the temperature.

Next, it was possible to present the specific load as a function of the sliding speed and operating temperature.

Exponential trend-lines were chosen to describe the minimum oil film thickness h_0 as a function of the sliding speed and temperature:

$$h_0 = C(T) e^{D(T)u_s} \quad (9)$$

where C is the coefficient,
 T is the temperature,
 e is the Neper number,
 D is the coefficient,
 u_s is the sliding speed.

Polynomial trend-lines were chosen to describe the coefficients C and D in the equation (9) as functions of the temperature T . The highest possible degree of polynomials was lower than the number of the experimentally determined isotherms. To achieve smooth trend-lines, the simplest polynomials of the first, second and third degree were preferred. For example, the following polynomial of the third degree was used for the coefficient C :

$$C(T) = \sum_{i=0}^3 c_i T^i \quad (10)$$

where c_i is the coefficient,
 T is the temperature.

Next, it was possible to present the minimum oil film thickness as a function of the sliding speed and operating temperature.

For the final analysis, the data related to the isotherms and oil film thickness were combined by the following way: first, the sliding speed at the constant thickness curves (for example with the minimum oil thickness $h_0 = 1, 2, 3 \dots \mu\text{m}$) was determined by using the coefficients C and D from the equation (9) and solving the following equation by iteration:

$$h_0 = C(T)e^{D(T)u_s} = 1,2,3\dots\mu\text{m} \quad (11)$$

where C is the coefficient,
 T is the temperature,
 e is the Neper number,
 D is the coefficient,
 u_s is the sliding speed.

To determine the specific load at the constant thickness curves, the equation (7) was solved by using the sliding speed from the equation (11). The isotherms of the operating temperature of the bearing, the specific load at the constant thickness curves and the experimentally determined limit of the operating range were plotted in one figure as functions of the sliding speed.

4.2.2 Determination of the friction loss in journal bearings

Friction loss is typically one of the significant energy losses in running machines and engines. Because friction generates heat, friction loss causes various heat flows that heat the machine or engine. Heat flows caused by friction loss can be determined by carrying out experimental or theoretical heat flow analyses. A thorough heat flow analysis to determine the friction loss of a dynamically loaded journal bearing was presented by Berg (1996). Experimental heat flow analysis is a useful method, particularly for tribological research into crankshaft bearings of internal combustion engines. It is typically possible to determine total friction loss of a running engine by using common experimental methods, such as those presented by Heywood (1988). However, it is practically impossible to specify friction loss for all the subsystems of the engine. A common assumption is that the engine components most subject to friction are the crankshaft bearings and the components of the piston assembly and valve train. For example, according to estimates presented by Coy (1998), in a petrol engine running at a certain load and lubricated with different multi-grade oils, the friction losses in the crankshaft bearings, piston assembly and valve train are 38 to 40 %, 36 to 51 % and 9 to 26 % of the total friction loss, respectively. By performing a thorough experimental heat flow analysis for engine bearings, it is possible to determine the friction loss of the bearings and, therefore, significantly increase the accuracy of estimates related to the distribution of friction loss in the engine. Accurate information on the distribution of friction loss is useful, for example, for the development of low-friction engines.

In this study, friction loss in the hydrodynamic journal bearing was analysed by carrying out an experimental heat flow analysis adapted for test rig experiments. In this experimental heat flow analysis, different heat flows related to the friction loss of a journal bearing were determined by measurements and calculations. The simplest equations were used in the calculations. A schematic representation of the experimental heat flow analysis is presented in Figure 4-4.

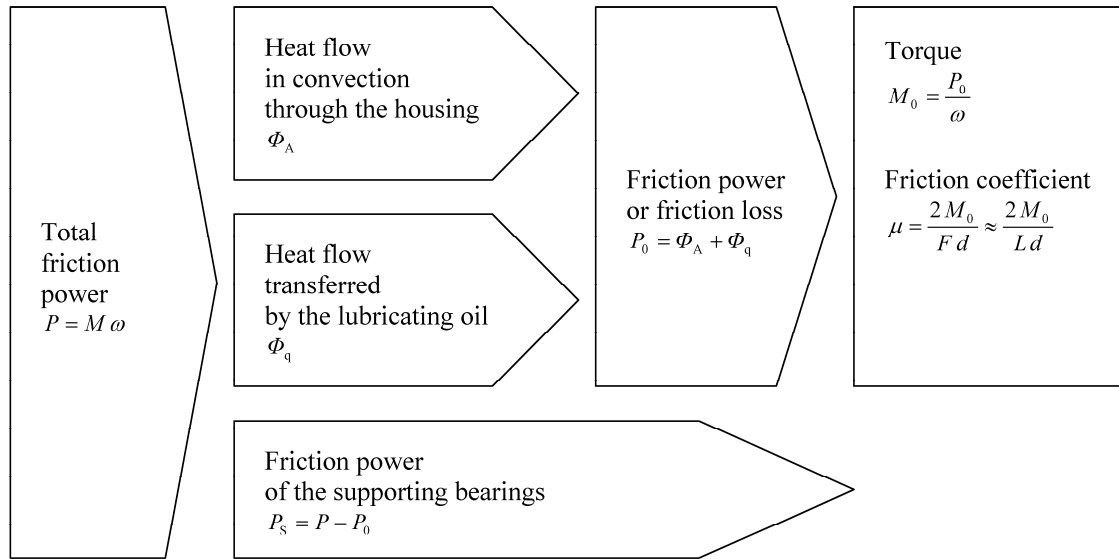


Figure 4-4. Schematic representation of the experimental heat flow analysis developed for test rig experiments on journal bearings with circulating lubrication.

The experimental heat flow analysis consisted of various phases. At first, the heat flow in convection through the housing Φ_A was determined experimentally. When the temperature of the housing varied freely, the following equation was used:

$$\Phi_A = h A (T_A - T_R) = h A \left(\frac{T_B + T_H}{2} - T_R \right) \quad (12)$$

where h is the heat transfer coefficient,
 A is the surface area of the housing,
 T_A is the average temperature,
 T_R is the ambient temperature,
 T_B is the operating temperature of the bearing,
 T_H is the temperature of the housing.

When the temperature of the housing was controlled, a part of the heat flow in convection through the housing was generated by heating resistors and the heat flow in

convection through the housing Φ_A was determined experimentally by the following equation:

$$\Phi_A = h A \left(\frac{T_B + T_H}{2} - T_R \right) - h A (T_H - T_R) = h A \left(\frac{T_B - T_H}{2} \right) \quad (13)$$

where h is the heat transfer coefficient,
 A is the surface area of the housing,
 T_B is the operating temperature of the bearing,
 T_H is the temperature of the housing,
 T_R is the ambient temperature.

The surface area of the housing A in the above equations (12) and (13) was set to be equal to the total outer surface area of the following set of jointed components: the housing, force ring and seal ring covers. An approximate constant value of the heat transfer coefficient h was determined experimentally in a cooling test, presented in Appendix D. It is noteworthy that the data from the cooling test were also used to determine the gradient of temperature in free cooling $\Delta T_c / \Delta t$, a useful parameter for mapping the operating temperature.

Next, the heat flow transferred by the lubricating oil Φ_q was determined experimentally by using the following equation:

$$\Phi_q = q [(c(T_2) \rho(T_2) T_2) - (c(T_1) \rho(T_1) T_1)] \quad (14)$$

where q is the volume flow,
 c is the specific heat capacity,
 T_2 is the outlet temperature,
 ρ is the density,

T_1 is the inlet temperature.

The density ρ and the specific heat capacity c in the above equation (14) may either be measured or calculated by different standard methods. For example, Dzida and Prusakiewicz (2008) measured densities and specific heat capacities of different oils. Effenberger (2000) presented an equation for estimating specific heat capacity as a function of the density and temperature. By using the approximate values and equations presented by Affenzeller and Gläser (1996), for typical engines oils with a density of about 900 kg/m^3 and a specific heat capacity of about 1.8 kJ/kgK , it can be calculated that the relative change in density is typically about $-0.07 \text{ \%}/\text{K}$ and the relative change in specific heat capacity is typically about $0.2 \text{ \%}/\text{K}$. In this study, it was assumed that the density varies linearly as a function of the temperature at a constant pressure, it was estimated that the relative change in density $\Delta\rho/\Delta T$ was $-0.07 \text{ \%}/\text{K}$, and the density ρ was calculated by the following equation:

$$\rho(T) = \rho_{\text{Ref}} + \Delta\rho/\Delta T (T - T_{\text{Ref}}) \approx \rho_{\text{Ref}} (1 - 0.0007(T - T_{\text{Ref}})) \quad (15)$$

where ρ_{Ref} is the reference density,
 T is the temperature,
 T_{Ref} is the reference temperature.

In addition, it was assumed that the specific heat capacity varies linearly as a function of the temperature at constant pressure, it was estimated that the reference specific heat capacity c_{Ref} of all oils was about 1.8 kJ/kgK at the reference temperature T_{Ref} of 288.15 K ($15 \text{ }^\circ\text{C}$) and that the relative change in specific heat capacity $\Delta c/\Delta T$ was $0.2 \text{ \%}/\text{K}$, and the specific heat capacity c was calculated by the following equation:

$$c(T) = c_{\text{Ref}} + \Delta c/\Delta T (T - T_{\text{Ref}}) \approx 1.8 \cdot 10^3 (1 + 0.002(T - 288.15)) \quad (16)$$

where c_{Ref} is the reference specific heat capacity,
 T is the temperature,
 T_{Ref} is the reference temperature.

The friction loss in a journal bearing is caused by friction where the bearing, lubricant and shaft come into contact. In the heat flow analysis, this friction loss was called friction power. The friction power P_0 was calculated by using the following equation:

$$P_0 = \Phi_A + \Phi_q \quad (17)$$

where Φ_A is the heat flow in convection through the housing,
 Φ_q is the heat flow transferred by the lubricating oil.

The angular velocity ω was calculated by using the following equation:

$$\omega = 2\pi n \quad (18)$$

where n is the rotational speed of the shaft.

The torque M_0 was calculated by using the following equation:

$$M_0 = \frac{P_0}{\omega} \quad (19)$$

where P_0 is the friction power,
 ω is the angular velocity.

The friction coefficient μ was calculated by using the following equation:

$$\mu = \frac{2M_0}{Fd} \quad (20)$$

where M_0 is the torque,
 F is the load,
 d is the diameter of the shaft.

In this case, the load F was the resultant of the forces generated by the load cylinders of the bearing test rig. In a running internal combustion engine, the load F is the counterforce of the bearing load L . The relation of the load F and the bearing load L was determined by the following equation:

$$L = F\sqrt{1 - \mu^2} \Rightarrow L \approx F \text{ if } (\mu \approx 0) \quad (21)$$

where μ is the friction coefficient,
 F is the load.

According to the above equation (21), there is a difference between the magnitudes of load F and bearing load L , but this is practically insignificant with a small friction coefficient μ , for example under hydrodynamic operation of the bearing. Therefore, the value of the load F can usually be used as an estimate of the value of the bearing load L or *vice versa*. In addition, the friction coefficient μ can be estimated accurately enough by using the following equation:

$$\mu \approx \frac{2M_0}{Ld} \quad (22)$$

where M_0 is the torque,
 L is the bearing load,
 d is the diameter of the shaft.

At this stage, the variables required for determining the friction loss (friction power) and friction coefficient were defined. In practice, it was still useful to determine two variables: the total friction loss in the bearing test rig and the friction power of the supporting bearings of the shaft.

The total friction loss P was calculated by using the following equation:

$$P = M \omega \quad (23)$$

where M is the total torque,
 ω is the angular velocity.

The friction power of the supporting bearings P_s was calculated by using the following equation:

$$P_s = P - P_0 \quad (24)$$

where P is the total friction loss,
 P_0 is the friction power.

Because some details were excluded from the heat flow analysis, as it was carried out using the minimum number of measuring devices, it was evident that there were certain inaccuracies in the results of the analysis. In addition, possible errors in determining the heat transfer coefficient h , density ρ and specific heat capacity c may have caused inaccuracies. Small variation in operating parameters may also have caused errors. The estimated relative error in the total friction loss P was $\pm 10\%$.

4.2.3 Determination of the oil film temperature

In the experiments made during this study, one of the key variables was the oil film temperature, which was estimated to be equal to the operating temperature, *i.e.* the temperature of the bearing under certain operating conditions. The temperature of the bearing was measured by using one or two thermocouples placed in bushings with springs. There were three temperature measurement points (T1, T2 and T3) on the outer surface of the upper bearing shell on the circumferential centreline (see Figure 4-5). The maximum measured temperature in the bearing was used as the oil film temperature. At typical bearing loads, sliding speeds and direction of rotation (clockwise), the maximum temperatures were measured at the temperature measurement point T2. It can be estimated that the error in the oil film temperature was about ± 0.5 °C.

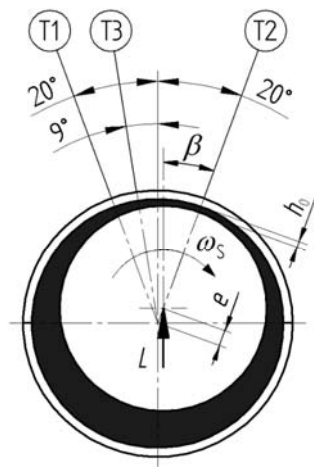


Figure 4-5. Temperature measurement points T1, T2 and T3 on the outer surface of the upper bearing shell. The bearing carries the bearing load L . The shaft rotates at the angular velocity ω_s . The eccentricity e and the angle β determine the position of the point with the minimum oil film thickness h_0 .

4.2.4 Determination of the oil film thickness

The minimum oil film thickness was either simulated by the simulation software or calculated. The simulations are presented in Chapter 4.3. The calculations are presented below.

The calculation was made in three phases. In the first phase, the Sommerfeld number S_o (a dimensionless parameter used in bearing performance calculations) was determined approximately by the following equation, based on the measurement data:

$$S_o = \frac{F\psi^2}{DB\eta\omega} = \frac{F\psi^2}{DB\nu\rho\omega} \quad (25)$$

where F is the bearing load,
 ψ is the relative bearing clearance,
 D is the diameter of the bearing,
 B is the width of the bearing,
 η is the dynamic viscosity,
 ν is the kinematic viscosity,
 ρ is the density,
 ω is the hydrodynamic angular velocity.

The density ρ in equation (25) was calculated as a function of the temperature by using equation (15). In the second phase, the relative eccentricity ε was determined approximately as a function of the Sommerfeld number S_o and the width-to-diameter ratio B/D of the bearing (see Appendix F). The approximation was made for a plain bearing with the width-to-diameter ratio $B/D = 32 \text{ mm} / 85 \text{ mm} = 0.376$, and the relative eccentricity ε was calculated by the following approximate equation:

$$\varepsilon \approx k_1 So^{k_2}, 1 \leq So \leq 200 \quad (26)$$

where k_1 is the coefficient,
 So is the Sommerfeld number,
 k_2 is the coefficient.

The values of the coefficients k_1 and k_2 in the equation (26) are presented in Table 4-1.

Table 4-1. Values of the coefficients k_1 and k_2 with different values of the Sommerfeld number So .

	k_1	k_2
$1 \leq So < 10$	0.798	0.073
$10 \leq So \leq 100$	0.897	0.022
$100 < So \leq 200$	0.980	0.0028

In the third phase, the following equation was used to calculate the minimum oil film thickness h_0 as a function of the bearing diameter, relative bearing clearance and relative eccentricity:

$$h_0 = \frac{1}{2} D \psi (1 - \varepsilon) \quad (27)$$

where D is the diameter of the bearing,
 ψ is the relative bearing clearance,
 ε is the relative eccentricity.

Due to the use of a simple calculation method, it can be estimated that the relative error in the calculated minimum oil thickness was high, about $\pm 20\%$, when the results are compared to values determined by detailed calculation methods.

4.2.5 Determination of the oil film pressure

For the experimental determination of the oil film pressure, optical pressure sensors were used. The optical pressure sensors were developed by a research team (Ronkainen *et al.*, 2008), of which the Author was a member. The Author participated in designing and testing the sensors. The optical pressure sensors were based on optical fibre technology that provides benefits such as insensitivity to electromagnetic disturbances and the capability to transmit information over long distances. The optical sensors were integrated in the bearing in such a way that the sliding surface of the bearing remained unchanged and acted as a measurement membrane. The operating principle of the optical pressure sensor is presented in Figure 4-6.

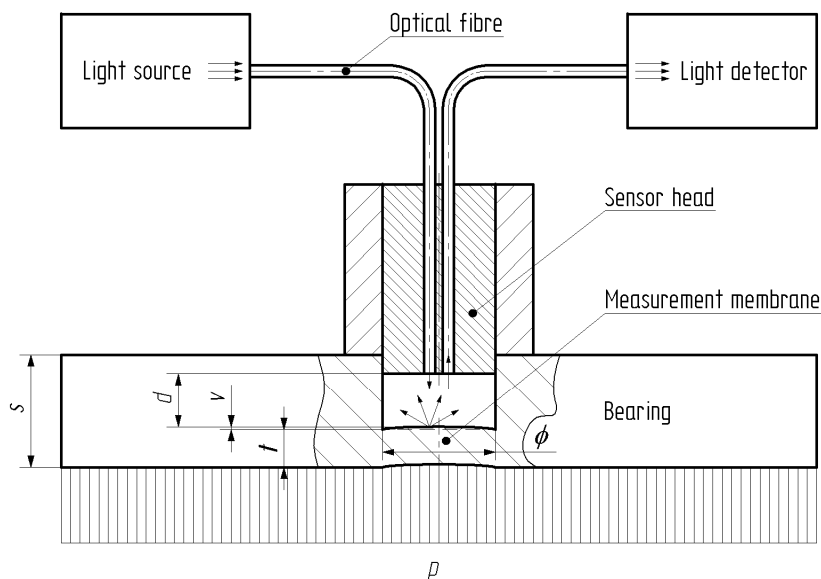


Figure 4-6. Operating principle of the optical pressure sensor. The light source with an optical fibre illuminated the measurement membrane with the thickness t and the diameter ϕ in the bearing with the thickness s . Part of the light reflected from the measurement membrane was coupled to another optical fibre. The intensity of the coupled light was measured by the light detector. The light intensity depended on the distance d between the sensor head and the measurement membrane. The variation in the oil film pressure p on the sliding surface of the bearing caused variation in the deflection v of the measurement membrane and, thereby, also in the distance d .

The optical pressure sensor consisted of a sensor head with illuminating and receiving optical fibres, a supporting tube, two protection sleeves and a rubber ring (see Figure 4-7). The multimode optical fibres had a diameter of 125 μm and were attached to the innermost metallic tube of the sensor head by glue (see Figure 4-8). Two different types of optical pressure sensor were used in the experiments. The first sensor type was called PROTO1 and the second one was called PROTO2. They had the same main dimensions, but different fibre and tube fitting designs.

In the test rig experiments with the first sensor type, a halogen lamp was used as the light source. A photometer was used as the light detector. The measurement signal sent by the photometer was recorded by the measurement computer. The sampling frequency was 2 kHz and the sample size was 1024.

In the test rig experiments with the second sensor type, a white light transmitter was used as the light source. A total of four photometers were used as light detectors: Three photometers detected signals reflected from the measurement membranes. One photometer detected a reference signal from the light source. The measurement signals sent by the photometers were recorded both by the measurement computer (at low frequency) and an additional spectrum analyser of VTT Technical Research Centre of Finland (at high frequency). The data recorded at high frequency were used in the analysis. The sampling frequency was 12.5 kHz and the sample size was 4096. To eliminate certain possible disturbances in the measurement signal, the following measures were taken: 1) the reference signal was used to detect variation in the light output, 2) a thermal aging process was carried out before the test rig experiments to avoid thermal effects in the sensor head and 3) fibre coils were used to avoid cladding modes produced by deflection in the optical fibres.

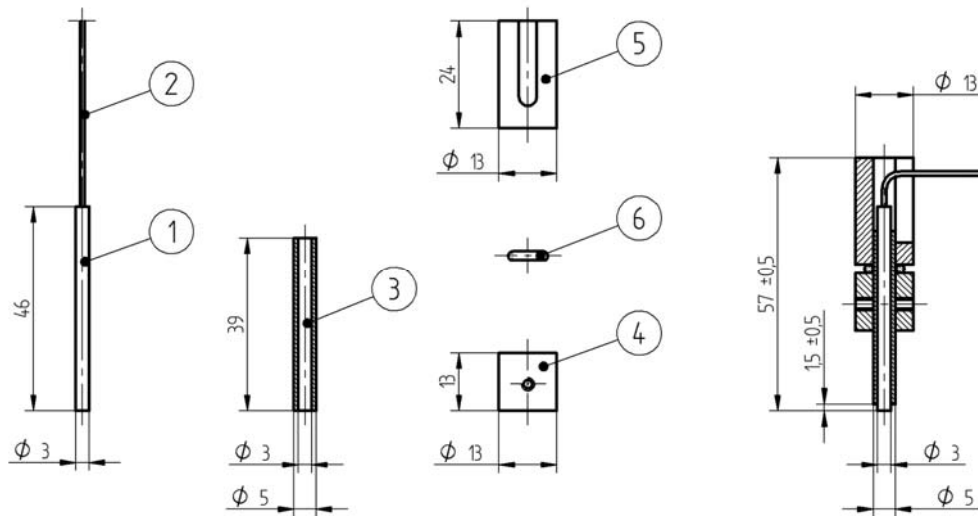


Figure 4-7. Design of the optical pressure sensor. The optical sensor consisted of a sensor head (1) with optical fibres for illumination and reception (2), a supporting tube (3), lower protection sleeve (4), upper protection sleeve (5) and a rubber ring (6).

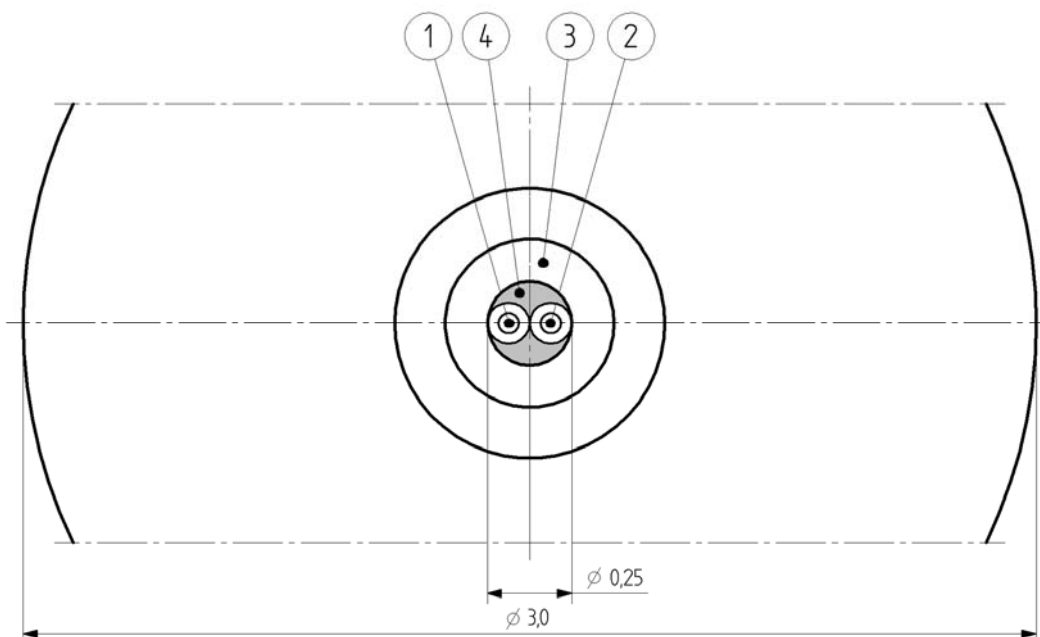


Figure 4-8. Front view of the sensor head with nested metallic tubes and multimode optical fibres with a diameter of 125 μm . The illuminating fibre (1) and the receiving fibre (2) were in the innermost tube (3). The fibres were attached to the tube by glue (4).

The characteristics of the optical pressure sensor depended on the design and materials of the bearing, especially on the dimensions of the measurement membrane on the bottom of a cavity drilled in the bearing (see Figure 4-9). The diameter ϕ of the measurement membrane was 3.5 mm. The thickness t of the measurement membrane was 1.0 mm (with the first sensor type) or 0.8 mm (with the second sensor type). The radius of curvature R in the cavity was about 0.5 mm. The characteristics of the optical pressure sensor also depended on the pre-tension of the bearing in the housing. The pre-tensioning has been taken into account in the sensor design.

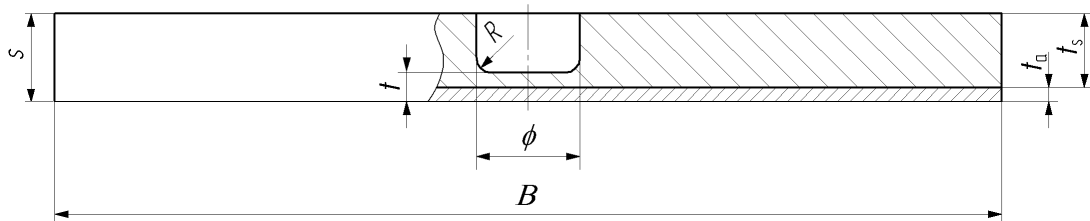


Figure 4-9. Measurement membrane in the bearing with the width $B = 32$ mm and the thickness $s = 3$ mm. The thickness t , the diameter ϕ and the radius of curvature R of the measurement membrane were optimised. The thickness of bronze layer t_a and the thickness of steel layer t_s were taken into account in the optimisation.

Various calculations by the finite element method (FEM) and pre-tests with different devices were made to optimise the design of the optical pressure sensors. The main aims for optimising sensor design were: 1) to obtain high durability, 2) to obtain sufficient sensitivity and 3) to keep the deflection of the measurement membrane so small that its effects on the geometry of the sliding surface remain negligible.

To meet the requirement for high durability, the measurement membrane was designed to operate elastically, that is, below the elastic limits of the bearing materials. To meet the requirements for sufficient sensitivity and small amounts of deflection, the measurement membrane was designed so that the deflection v is higher than the resolution γ of the optical sensor and smaller than the minimum oil film thickness h_0 , under typical operating conditions. In short, it can be estimated that these requirements have been met by a deflection to pressure ratio $\Delta v/\Delta p$ of about $0.03 \mu\text{m}/\text{MPa}$.

The intensity of the signal of the optical sensor varied as a function of the distance between the sensor head and the measurement membrane (see Figure 4-10). In typical measuring ranges, the signal decreased as the distance decreased. In the optimal measuring range, the gradient of the signal was at its highest and the signal varied almost linearly.

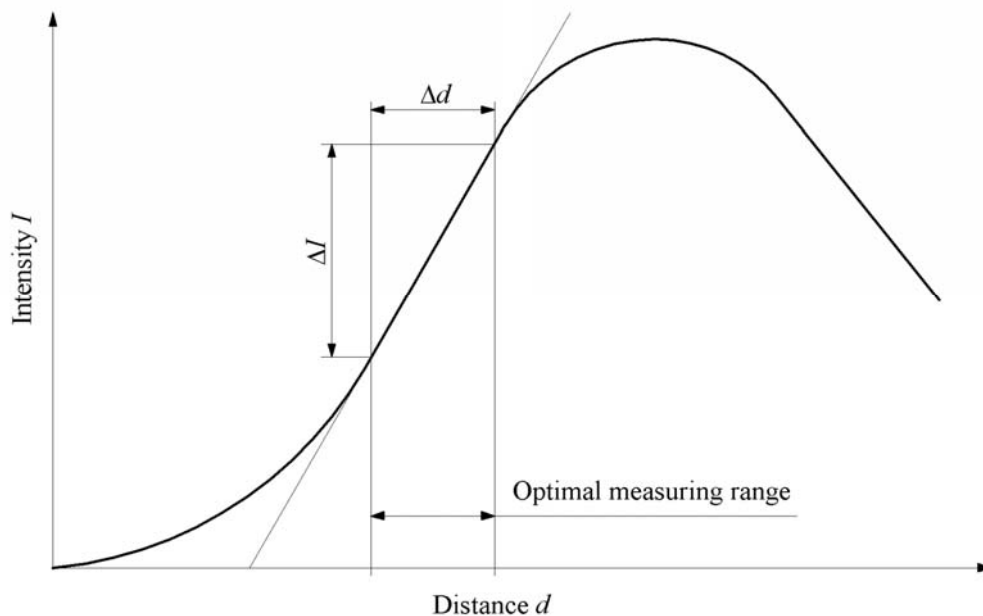


Figure 4-10. Intensity I of the signal of the optical sensor as a function of the distance d between the sensor head and the measurement membrane. In the optimal measurement range, the gradient $\Delta I/\Delta d$ of the signal was at its highest and the signal varied almost linearly.

The optical sensors were calibrated using a specially designed calibration device of VTT Research Centre of Finland. The head of the calibration device resembled a shaft with one radial oil-feeding hole. For the calibration, the optical sensor was installed in the bearing, which was mounted in the housing. During the calibration, pressurised oil was pumped onto the sliding surface of the bearing through the head of the calibration device. The oil pressure was varied gradually. The oil pressure range used in the calibration was 0 to 500 bar. The oil pressure and the signal from the optical pressure sensor were recorded either manually or automatically. The results from the calibration of the optical sensors are presented in Appendix E.

Because the optical pressure sensors had been calibrated before being installed with the bearing in the housing and the dispersion in the calibrated pressure signal was low, it can be estimated that the relative error in the measurement of the oil film pressure was low, about $\pm 5\%$, for cases without possible disturbing factors such as misalignment or deformation of the optical pressure sensor or the bearing.

4.2.6 Test material, lubricating oil supply and test run matrices

As mentioned above, the experimental studies were split up into range, friction and pressure experiment sets. In addition, the range experiment set was divided into two cases (Cases 1 and 2) and the pressure experiment set was divided into four cases (Cases 1, 2, 3 and 4).

The test material and lubricating oil supply for the range, friction and pressure experiment sets are presented in Table 4-2. The test run matrices for the range and friction experiment sets are presented in Table 4-3. The test run matrix for the pressure experiment set is presented in Table 4-4. The pressure measurement arrangements for the pressure experiment set are presented in Table 4-5.

Table 4-2. Test material and lubricating oil supply for the range, friction and pressure experiment sets.

	Range		Friction	Pressure
	Case 1	Case 2		
Bearing type	BA	BE	BS	BD
Shaft type	SB	SB	SA	SC
Housing type	HS	HS	HS	HO
Upper bearing shell	plain	plain	plain	plain
Lower bearing shell	plain	plain	grooved	grooved
Lubricating oil supplied through	shaft	shaft	bearing	shaft
Lubricating oil(s)	G	G	A, B, C, D, E, F	G

Table 4-3. Test run matrices with nominal (or target) operating parameters for the range and friction experiment sets.

	Range		Friction
	Case 1	Case 2	
Bearing load pattern	Static	Static	Static
Bearing load range [kN]	1 to 100	1 to 100	1 to 100
Minimum bearing load step [kN]	±1	±1	±1
Sliding speed range [m/s]	1 to 13	1 to 13	1 to 13
Minimum sliding speed step [m/s]	±1	±1	±1
Isotherms of the operating temperature of the bearing [°C]	≥90 (100, 105, 110, 115, 120, 125)	≥90 (105, 110, 115, 120, 125, 130)	≥90 (110, 115, 120)
Min. operating temperature step [°C]	±5	±5	±5
Temperature of the housing [°C]	90	90	90
Inlet temperature [°C]	90	80	90
Inlet pressure [bar]	6	6	6

Table 4-4. Test run matrix with nominal (or target) operating parameters for cases 1 to 4 of the pressure experiment set.

	Case 1	Case 2	Case 3	Case 4
Bearing load pattern	Rotating	Rotating	Static	Static
Bearing load [kN]	5.0, 7.5, 10.0, 12.5, 15.0	10.0	50, 60, 70	50
Sliding speed [m/s]	4	1, 2, 3, 4, 5	2	1.5, 2, 3, 4, 5, 6
Temperature of the housing [°C]	70	70	90	90
Inlet temperature [°C]	70	70	70	70
Inlet pressure [bar]	3	3	4.5	4.5

Table 4-5. Pressure measurement arrangements for cases 1 to 4 of the pressure experiment set.

	Case 1	Case 2	Case 3	Case 4
Optical sensor type code	PROTO1	PROTO1	PROTO2	PROTO2
Number of optical pressure sensors	1	1	3	3
Angular location of optical pressure sensors [deg.]	+63	+63	-27, +27, +45	-27, +27, +45
Diameter of the cavity [mm]	3.5	3.5	3.5	3.5
Thickness of the measurement membrane [mm]	1	1	0.8	0.8
Number of thermocouples measuring the operating temperature	1	1	1	1
Angular location of thermocouples [deg.]	-9	-9	-9	-9

4.3 Simulations

4.3.1 Simulation software and procedure

The bearing simulation method was based on the numerical solution of the Reynolds differential equation. The bearing simulations were made by the AVL EXCITE simulation software, which has been designed to predict the effects of external load in engine structures. The software used the finite element method (FEM) and finite element analysis (FEA) to simulate the dynamic response of engine parts connected by a set of nonlinear joints. The software consisted of a pre-processor with a graphical user interface and post-processors for two- and three-dimensional graphics.

The simulations were carried out to analyse the measured data and were executed by the Author. A typical simulation procedure carried out for different simulation cases included different phases. In the first phase, the simulation model was chosen from a model library and numerous detailed settings were made to determine the case and its parameters. The parameter values were typically based on the measured data. In addition, settings were made for the required output data and its illustration. In the second phase, the actual simulation run was performed. The duration of a simulation run for a single case was related to the complexity of the simulation case and to the quantity of the required output data. In the third phase, the results of the simulation run were gathered into a simulation report and the main results were illustrated by post-processors.

For an efficient use of the simulation software, a brief manual was written to focus on the cases studied. The manual set out recommended and optional settings required for the cases. By following the instructions presented in the manual, it was possible to use settings that had been examined beforehand. This saved time and avoided certain trivial errors in the settings for new cases.

4.3.2 Simulation model

A simple simulation model was used for the bearing simulations. The simulation model was chosen from the simulation model library of the simulation software. The simulation model consisted of an EHD2 type elasto-hydrodynamic bearing and a short SMOT type shaft in an anchored ANCH type housing (see Figure 4-11). The model of the bearing had 19 nodes in the axial direction and 121 nodes in the circumferential direction. The shaft had five mass points.

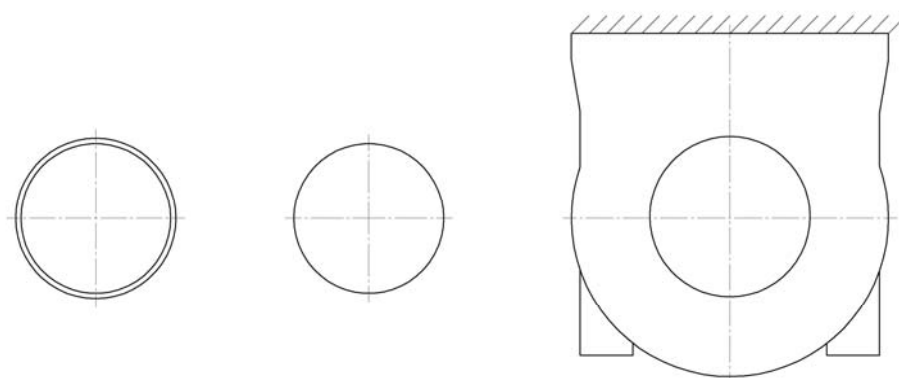


Figure 4-11. Simulation model. An elasto-hydrodynamic bearing, a short shaft and an anchored housing.

Both nominal and measured dimensions were used as the input data in the simulations to determine the main geometry of the components (bearings and shafts). The following parameters were used as the input data in the simulations to determine operating conditions of the bearing: the nominal bearing load, the nominal rotational speed of the shaft (for the nominal sliding speed), the measured operating temperature of the bearing, the nominal inlet temperature and the nominal inlet pressure.

It is noteworthy that in the simulations for elasto-hydrodynamic bearings, the oil temperature is assumed to be constant (*i.e.*, the increase in oil temperature due to

friction is ignored) and the inlet temperature is equal to the operating temperature of the bearing. In this study, the above-mentioned relation of different temperatures was taken into account. The measured operating temperature of the bearing was used as the input data (“the inlet temperature”) in the simulation. That is to say, the lubricating oil temperature was assumed to be constant and equal to the measured operating temperature of the bearing.

Numerous simulation control settings were made. The control settings influenced the accuracy of the simulation results. Some settings (for example, the minimum simulation step size and the maximum simulation step size) were varied according to the complexity of the case studied.

4.3.3 Simulated viscosity and density

In the simulation software, the viscosity η of the lubricating oil was determined by the Vogel-Barus method using the following equation:

$$\eta(p, T) = A e^{\left[\frac{B}{T+C} + \alpha p \right]} \quad (28)$$

where A is the viscosity parameter,
 B is the viscosity parameter,
 C is the viscosity parameter,
 e is the Neper number (≈ 2.71828),
 T is the temperature,
 α is the viscosity parameter,
 p is the pressure.

The equation used in the Vogel-Barus method is a combination of two equations: the Vogel equation gives the viscosity as a function of temperature and the Barus equation gives the viscosity as a function of pressure. The equation used in the Vogel-Barus

method does not take into account the complex variation in viscosity under extremely high pressure. In cases with an extremely high pressure, other equations, such as the Rodermund and Roelands equations, are required. The Rodermund equation was used by Pribsch and Krasser (1996). The Roelands equation was used by Coy (1998).

In the simulation software, the density ρ of the lubricating oil was determined by the Dowson-Higginson method using the following equation:

$$\rho(p,T) = \rho_0 \left[1 + \left(\frac{f_1 p}{1 + f_2 p} \right) \right] [1 - f_3 (T - T_0)] \quad (29)$$

where ρ_0 is the reference density,
 p is the pressure,
 T is the temperature,
 T_0 is the reference temperature,
 f_1 is the density parameter,
 f_2 is the density parameter,
 f_3 is the density parameter.

The settings related to the lubrication oils were adapted from the ones determined for typical engine oils in the oil data library of the software. The settings related to lubricating oil G are presented in Table 4-6. The viscosity and density of lubricating oil G are presented as functions of pressure and temperature in Appendix G.

Table 4-6. Settings related to the lubricating oil G.

Setting	
Viscosity calculation method	Vogel-Barus
Viscosity parameter A [Pas]	0.0000154
Viscosity parameter B [°C]	1600
Viscosity parameter C [°C]	137.7
Viscosity parameter α [1/MPa]	0.002
Density calculation method	Dowson-Higginson
Density parameter ρ_0 [kg/m ³]	916
Density parameter T_0 [°C]	15
Density parameter f_1 [1/MPa]	0.00060
Density parameter f_2 [1/MPa]	0.00170
Density parameter f_3 [1/°C]	0.00065
Specific heat capacity c [J/kgK]	2083

5 Results

5.1 Operating range

The results from the study of the operating ranges of hydrodynamic journal bearings are presented below. The study included the Cases 1 and 2 of the range experiment set.

Case 1: Operating range of the bearing BA

The dimensions and operating parameters used for Case 1 of the range experiment set, with the bearing BA, shaft SB and housing HS, are presented in Table 5-1.

Table 5-1. Dimensions and operating parameters used for Case 1 of the range experiment set, with the bearing BA, shaft SB and housing HS. The bearing was non-grooved. The lubricating oil G was supplied through the shaft.

Dimension or parameter	Value
Diameter of the bearing [mm]	85.107
Diameter of the shaft [mm]	84.940
Bearing clearance [μm]	167
Relative bearing clearance [$1/10^3$]	2.0
Temperature of the housing [$^{\circ}\text{C}$]	92.0 \pm 1.8
Inlet temperature [$^{\circ}\text{C}$]	84.0 \pm 0.8
Inlet pressure [bar]	5.99 \pm 0.05
Room temperature [$^{\circ}\text{C}$]	24.1 \pm 0.3

The specific load on the isotherms of the operating temperature is presented in Figure 5-1. Within the operating range of the bearing, six different isotherms of the operating temperature of the bearing were determined experimentally: the isotherms of 100, 105, 110, 115, 120 and 125 °C. The isotherms varied logarithmically as functions of the sliding speed. The trend-lines for the coefficients A and B are presented in Figure 5-2. The specific load on interpolated and extrapolated isotherms of the operating temperature is presented in Figure 5-3.

The calculated minimum oil film thickness on the isotherms of the operating temperature is presented in Figure 5-4. The minimum oil film thickness varied exponentially as a function of the sliding speed on the isotherms of the operating temperature. The trend-lines for the coefficients C and D are presented in Figure 5-5. The calculated minimum oil film thickness on the interpolated and extrapolated isotherms of the operating temperature is presented in Figure 5-6. The operating range with the isotherms and constant thickness curves is presented in Figure 5-7. Typically, the gradients of the constant oil film thickness curves were high at low sliding speeds and close to zero at high sliding speeds. The results from the calculations related to the minimum oil film thickness were briefly compared with the ones from the simulations. The simulated minimum oil film thickness is presented in Figure 5-8. The simulation did not converge at some points on the isotherms. The ratio of the calculated minimum oil film thickness to the simulated minimum oil film thickness was typically 1.0 to 1.7 (see Figure 5-9).

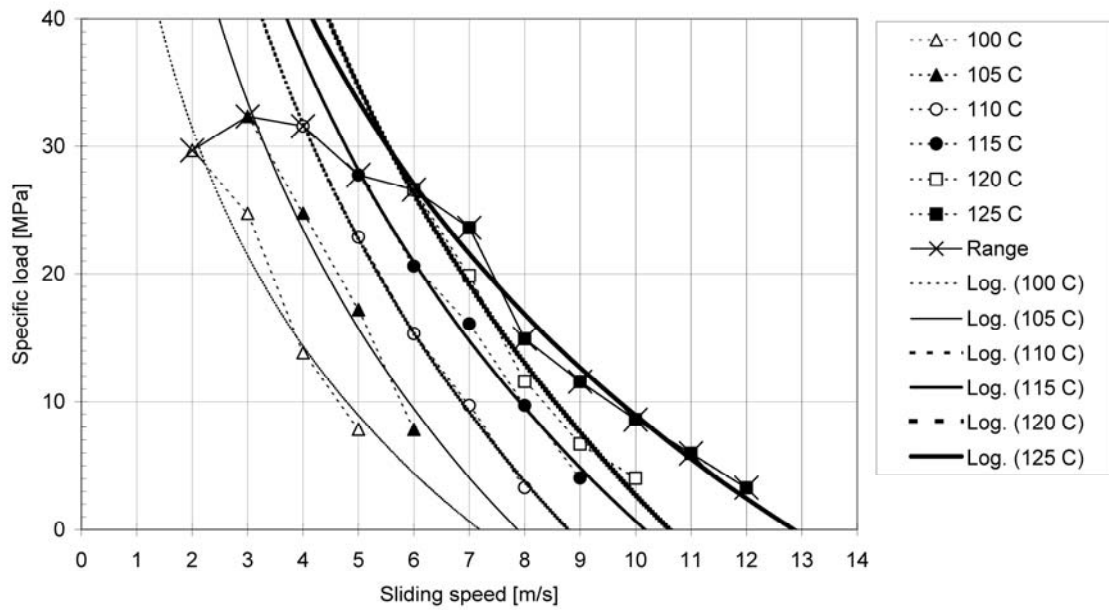


Figure 5-1. Specific load on the isotherms of the operating temperature. The presumed limit of the operating range of the bearing is show by a line with a cross. The isotherms of the operating temperature had logarithmic trend-lines with $R^2 > 0.90$.

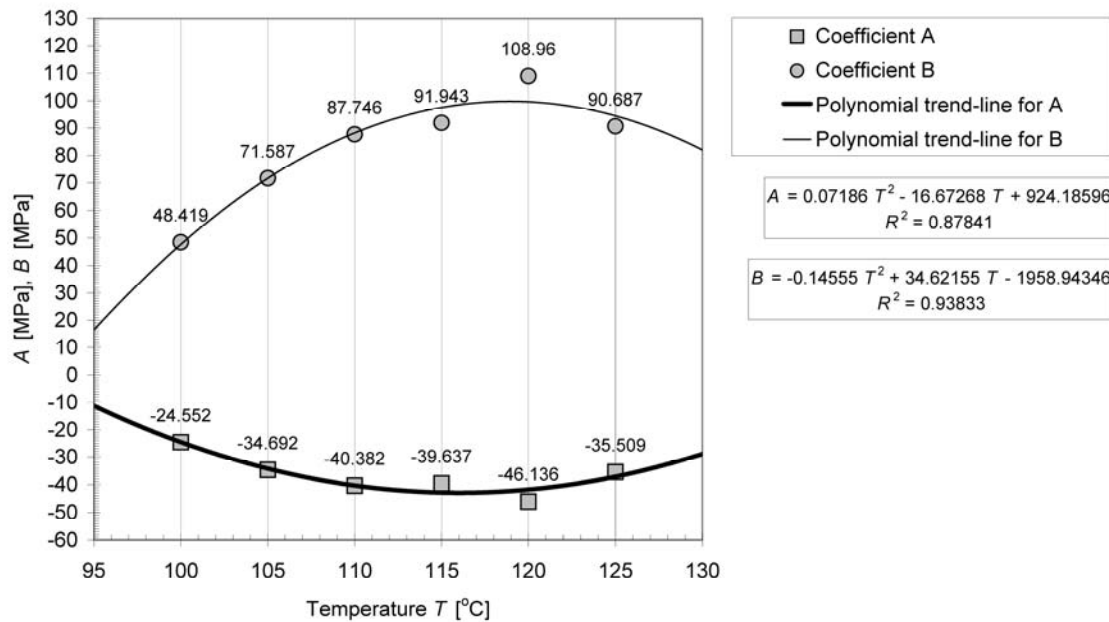


Figure 5-2. Trend-lines for the coefficients A and B in the equation $p_s = A(T)\text{Ln}(u_s) + B(T)$ showing the specific load p_s as a function of the temperature T and the sliding speed u_s .

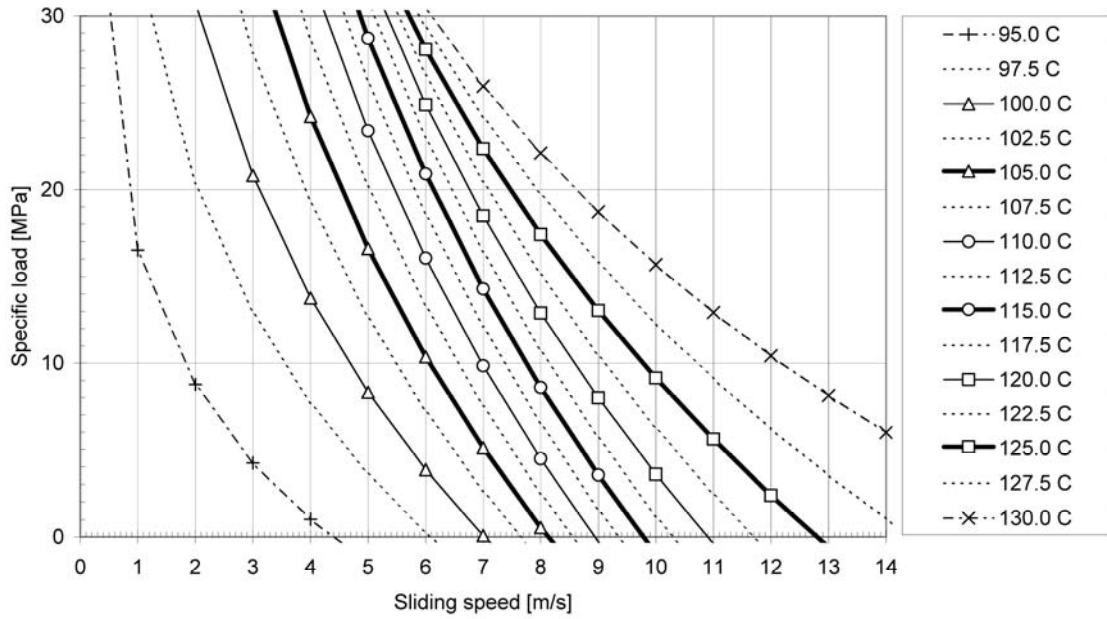


Figure 5-3. Specific load on the isotherms of the operating temperature. The isotherms were interpolated and extrapolated from the trend-line data.

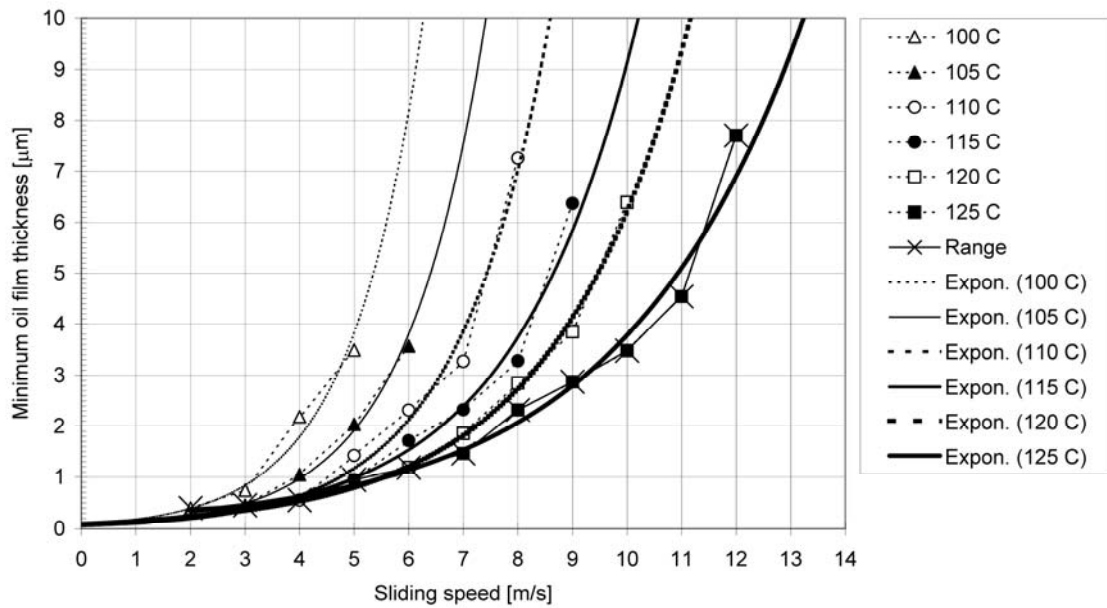


Figure 5-4. Calculated minimum oil film thickness on the isotherms of the operating temperature. The calculated minimum oil film thickness had exponential trend-lines with $R^2 > 0.90$.

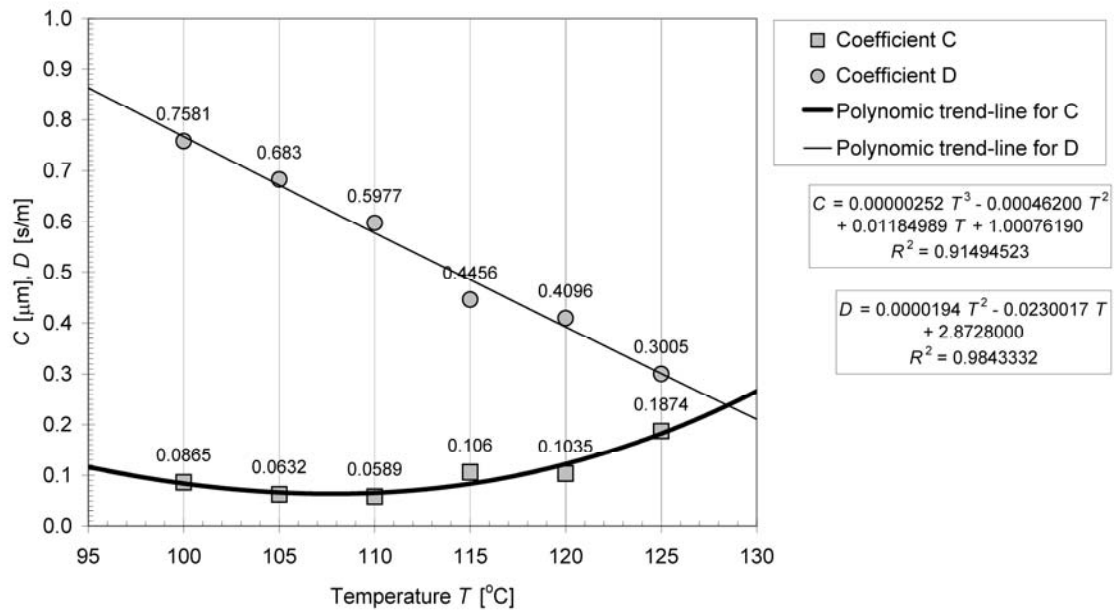


Figure 5-5. Trend-lines for the coefficients C and D in the equation $h_0 = C(T)e^{(D(T)u_s)}$ showing the minimum oil film thickness h_0 as a function of the temperature T and the sliding speed u_s .

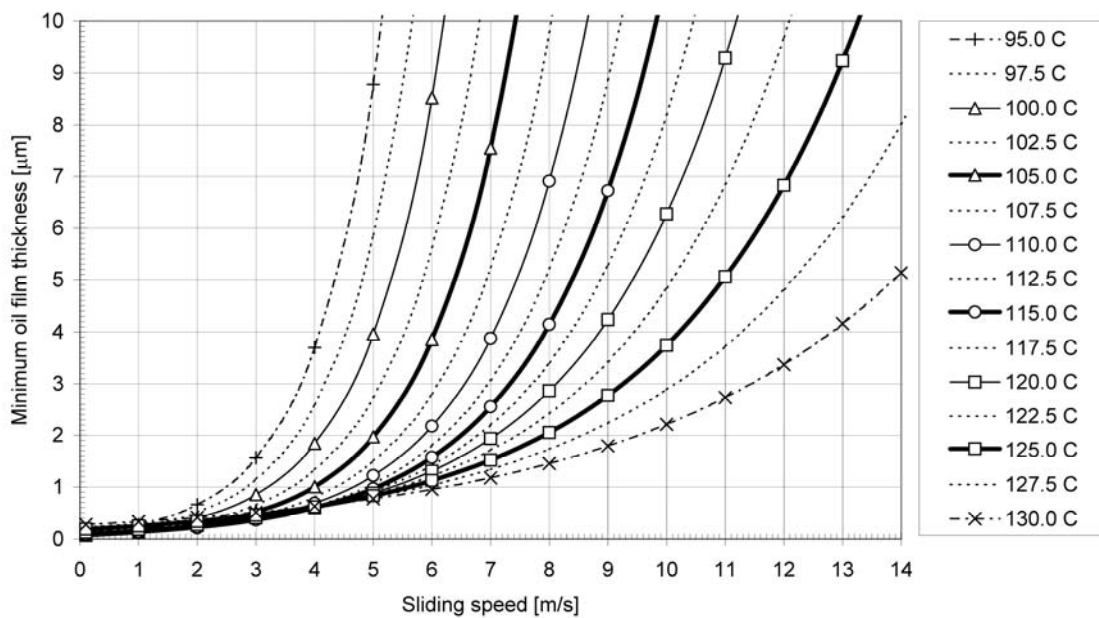


Figure 5-6. Calculated minimum oil film thickness on the isotherms of the operating temperature. The isotherms were interpolated and extrapolated from the trend-line data.

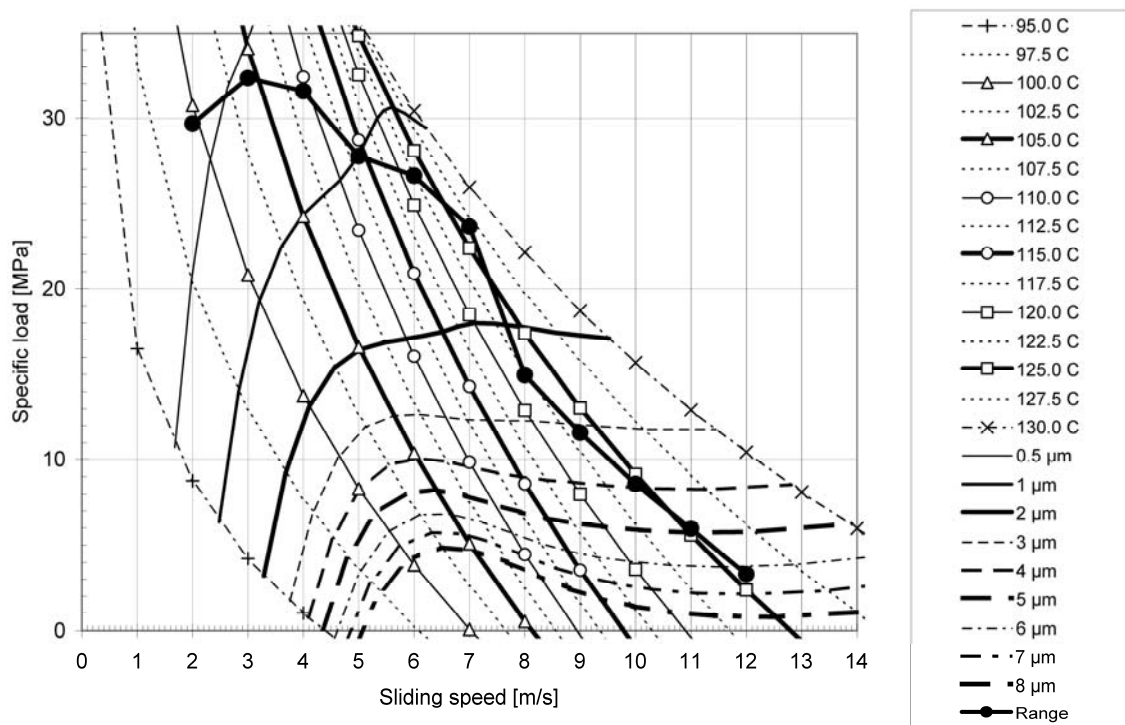


Figure 5-7. Operating range with the isotherms and constant thickness curves interpolated and extrapolated from the trend-line data.

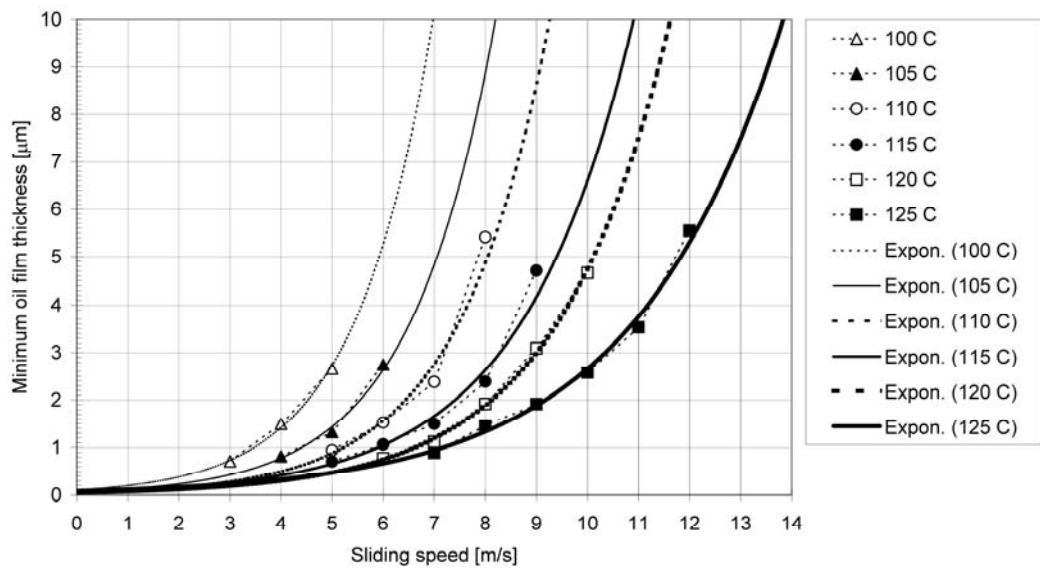


Figure 5-8. Simulated minimum oil film thickness (arithmetic mean) on the isotherms of the operating temperature. The simulated minimum oil film thickness had exponential trend-lines with $R^2 > 0.90$.

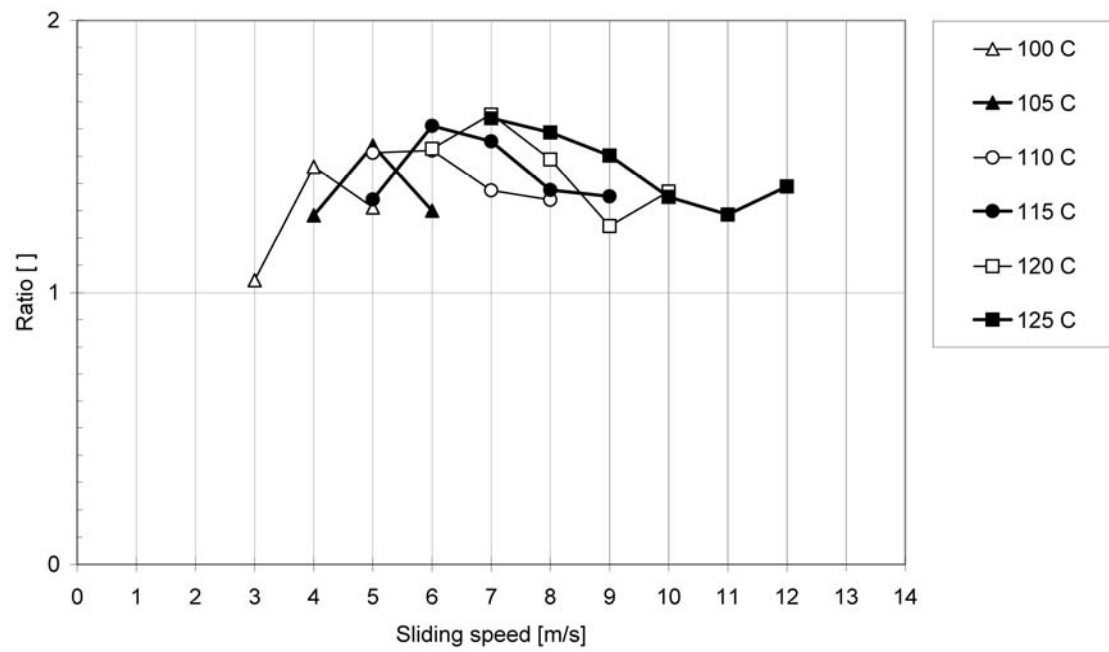


Figure 5-9. Ratio of the calculated minimum oil film thickness to the simulated minimum oil film thickness on the isotherms of the operating temperature.

Case 2: Operating range of the bearing BE

The dimensions and operating parameters used for Case 2 of the range experiment set, with the bearing BE, shaft SB and housing HS, are presented in Table 5-2.

Table 5-2. Dimensions and operating parameters used for Case 2 the range experiment set, with the bearing BE, shaft SB and housing HS. The bearing was non-grooved. The lubricating oil G was supplied through the shaft.

Dimension or parameter	Value
Diameter of the bearing [mm]	85.081
Diameter of the shaft [mm]	84.940
Bearing clearance [μm]	141
Relative bearing clearance [$1/10^3$]	1.7
Temperature of the housing [$^{\circ}\text{C}$]	95.6 ± 3.0
Inlet temperature [$^{\circ}\text{C}$]	77.5 ± 0.5
Inlet pressure [bar]	6.07 ± 0.02
Room temperature [$^{\circ}\text{C}$]	21.9 ± 0.2

The specific load on the isotherms of the operating temperature is presented in Figure 5-10. Within the operating range of the bearing, six different isotherms of the operating temperature of the bearing were determined experimentally: the isotherms of 105, 110, 115, 120, 125 and 130 $^{\circ}\text{C}$. The isotherms varied logarithmically as functions of the sliding speed. The trend-lines for the coefficients A and B are presented in Figure 5-11. The specific load on the interpolated and extrapolated isotherms of the operating temperature is presented in Figure 5-12.

The calculated minimum oil film thickness on the isotherms of the operating temperature is presented in Figure 5-13. The minimum oil film thickness varied exponentially as a function of the sliding speed on the isotherms of the operating temperature. The trend-lines for the coefficients C and D are presented in Figure 5-14.

The calculated minimum oil film thickness on the interpolated and extrapolated isotherms of the operating temperature is presented in Figure 5-15. The operating range with isotherms and constant thickness curves is shown in Figure 5-16. Typically, the gradients of the constant oil film thickness curves were high at low sliding speeds and close to zero at high sliding speeds (excluding the operating points on the highest isotherms).

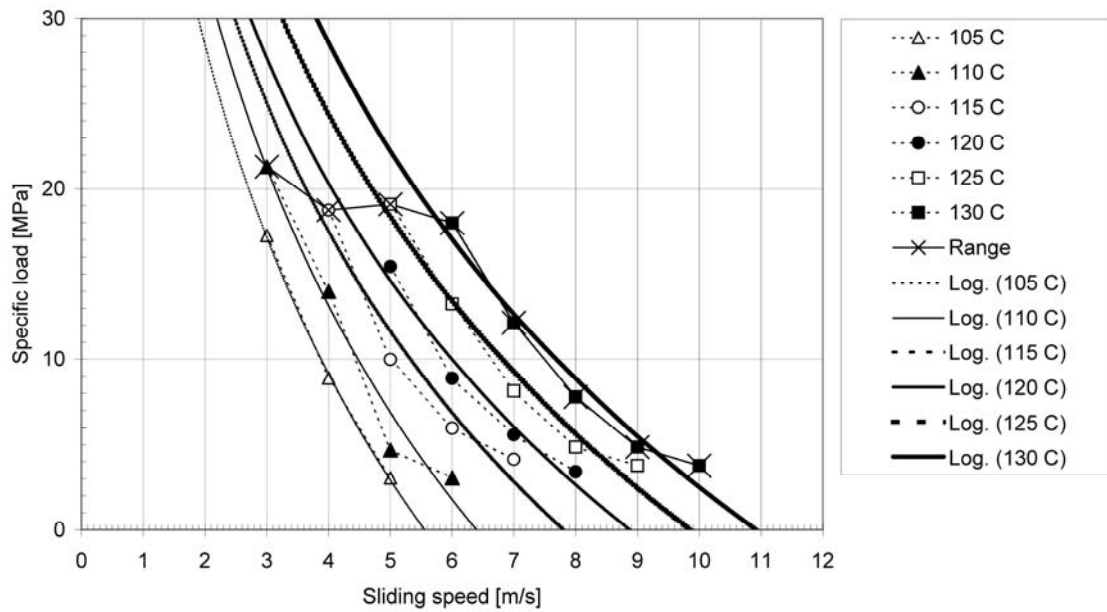


Figure 5-10. Specific load on the isotherms of the operating temperature. The presumed limit of the operating range of the bearing is shown by a line with a cross. The isotherms of the operating temperature had logarithmic trend-lines with $R^2 > 0.90$.

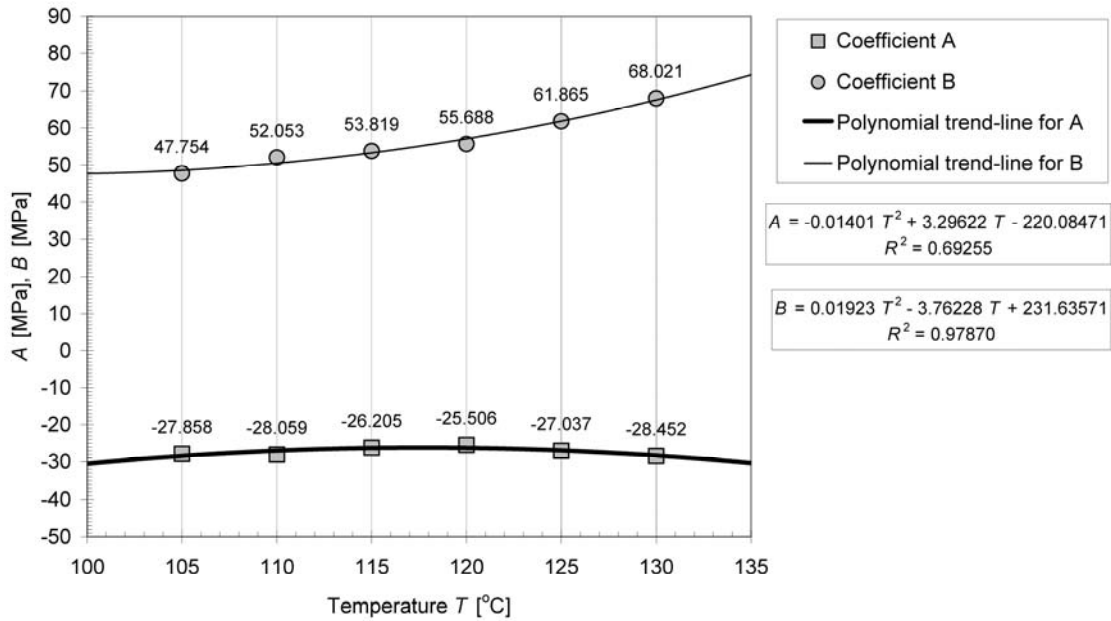


Figure 5-11. Trend-lines for the coefficients A and B in the equation $p_s = A(T)\text{Ln}(u_s) + B(T)$ showing the specific load p_s as a function of the temperature T and the sliding speed u_s .

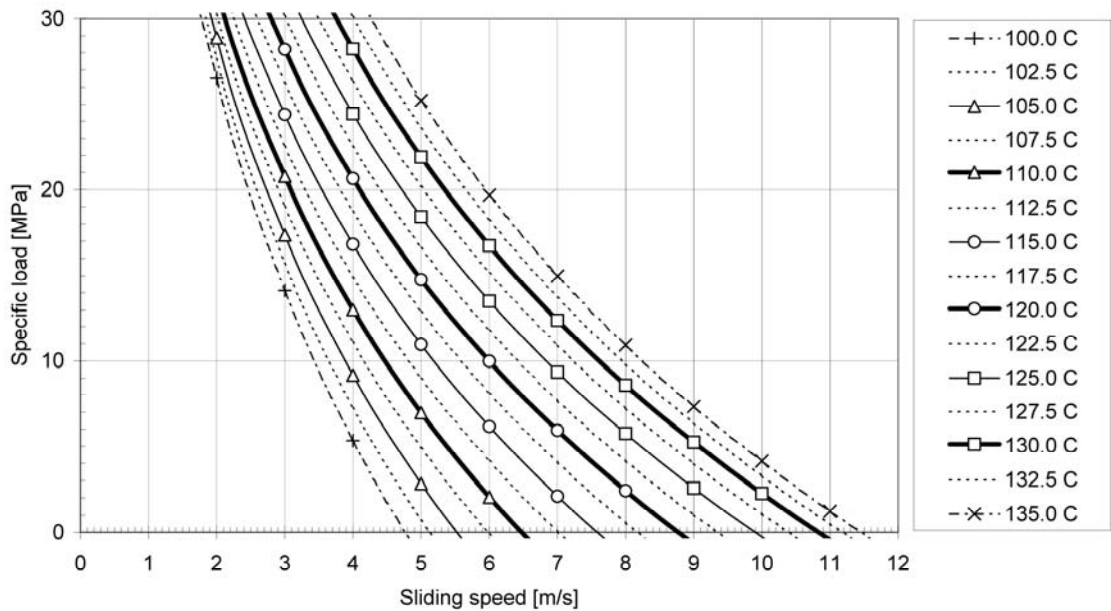


Figure 5-12. Specific load on the isotherms of the operating temperature. The isotherms were interpolated and extrapolated from the trend-line data.

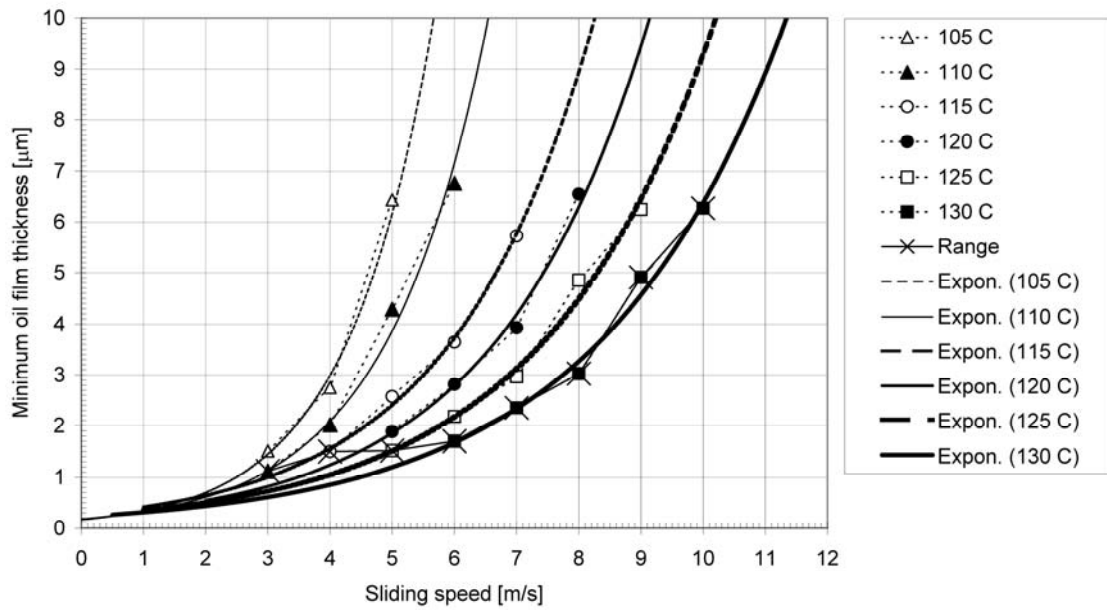


Figure 5-13. Calculated minimum oil film thickness on the isotherms of the operating temperature. The calculated minimum oil film thickness had exponential trend-lines with $R^2 > 0.90$.

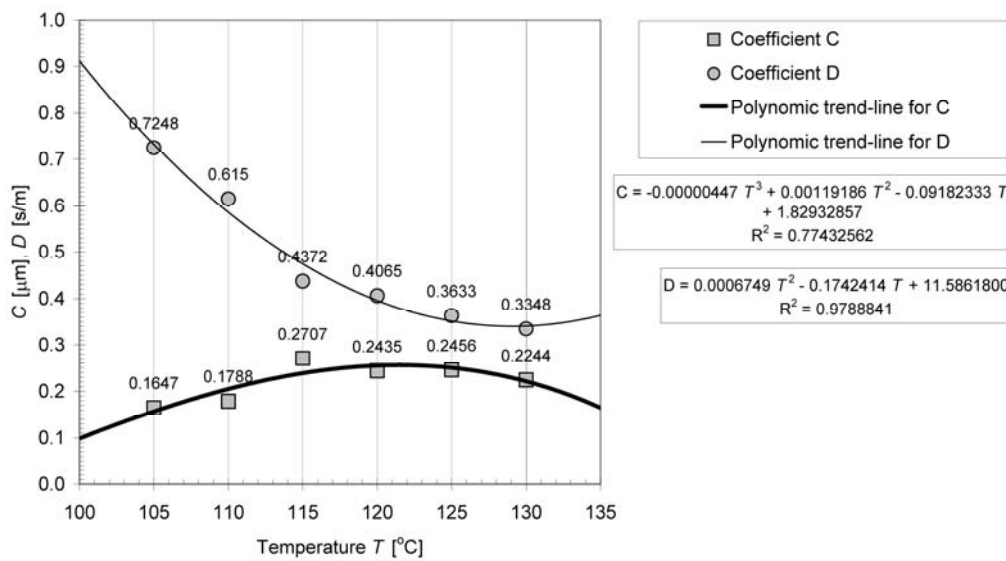


Figure 5-14. Trend-lines for the coefficients C and D in the equation $h_0 = C(T)e^{(D(T)u_s)}$ showing the minimum oil film thickness h_0 as a function of the temperature T and the sliding speed u_s .

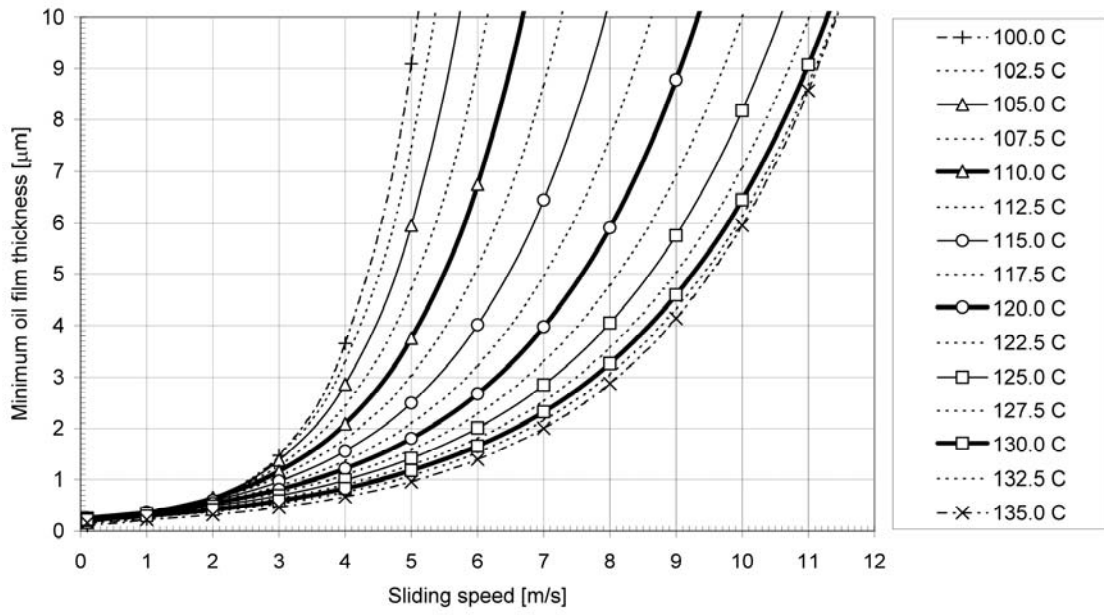


Figure 5-15. Calculated minimum oil film thickness on the isotherms of the operating temperature. The isotherms were interpolated and extrapolated from the trend-line data.

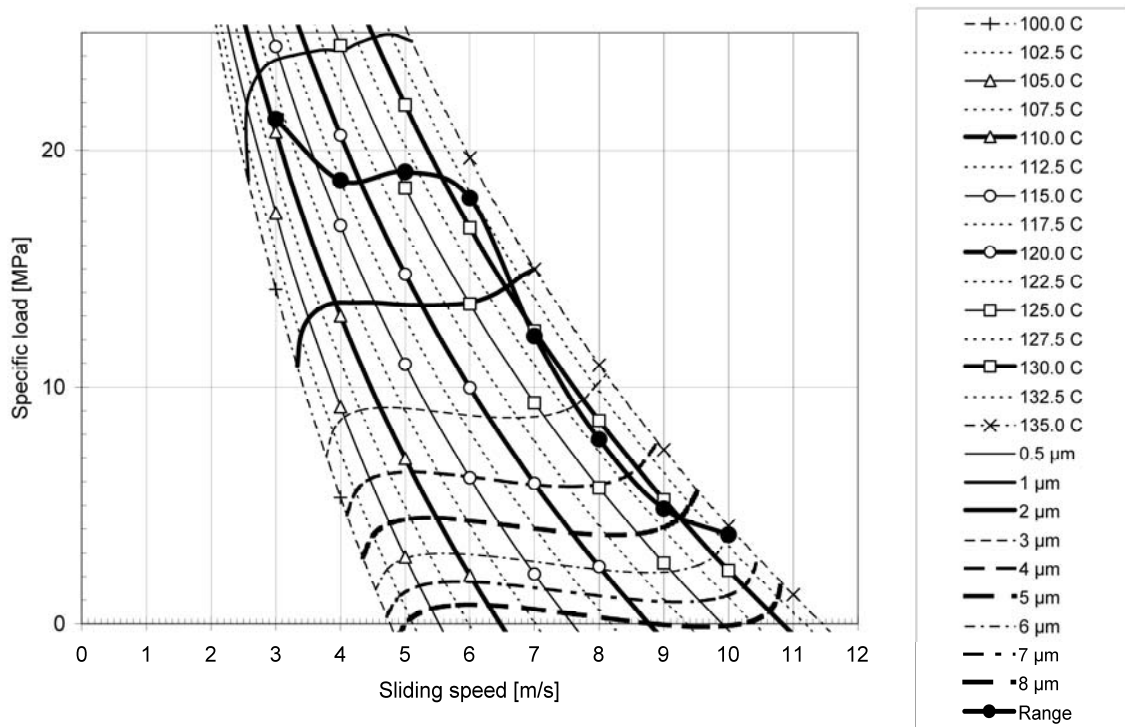


Figure 5-16. Operating range with isotherms and constant thickness curves interpolated and extrapolated from the trend-line data.

5.2 Friction loss

The results from the study of the friction loss and its influence on the width of the operating range of the hydrodynamic journal bearing are presented below. The study included the friction experiment set. The dimensions and operating parameters used for the friction experiment set, with the bearing BS, shaft SA and housing HS, are presented in Table 5-3.

Table 5-3. Dimensions and operating parameters used for the friction experiment set, with the bearing BS, shaft SA and housing HS. The lower sleeve of the bearing was grooved. The lubricating oils A, B, C, D, E and F were supplied through the bearing.

Dimension or parameter	Value
Diameter of the bearing [mm]	85.097
Diameter of the shaft [mm]	85.000
Bearing clearance [μm]	97
Relative bearing clearance [$1/10^3$]	1.1
Temperature of the housing [$^{\circ}\text{C}$]	91.8 \pm 0.7
Inlet temperature [$^{\circ}\text{C}$]	87.9 \pm 0.7
Inlet pressure [bar]	6.05 \pm 0.03
Room temperature [$^{\circ}\text{C}$]	22.7 \pm 0.2

The specific loads on the isotherms of the operating temperature with oils A, B, C, D, E and F are shown in Figure 5-17, Figure 5-18, Figure 5-19, Figure 5-20, Figure 5-21 and Figure 5-22, respectively. For all oils, three different isotherms of the operating temperature of the bearing were determined experimentally: the isotherms of 110, 115 and 120 $^{\circ}\text{C}$. The isotherms varied logarithmically as functions of the sliding speed.

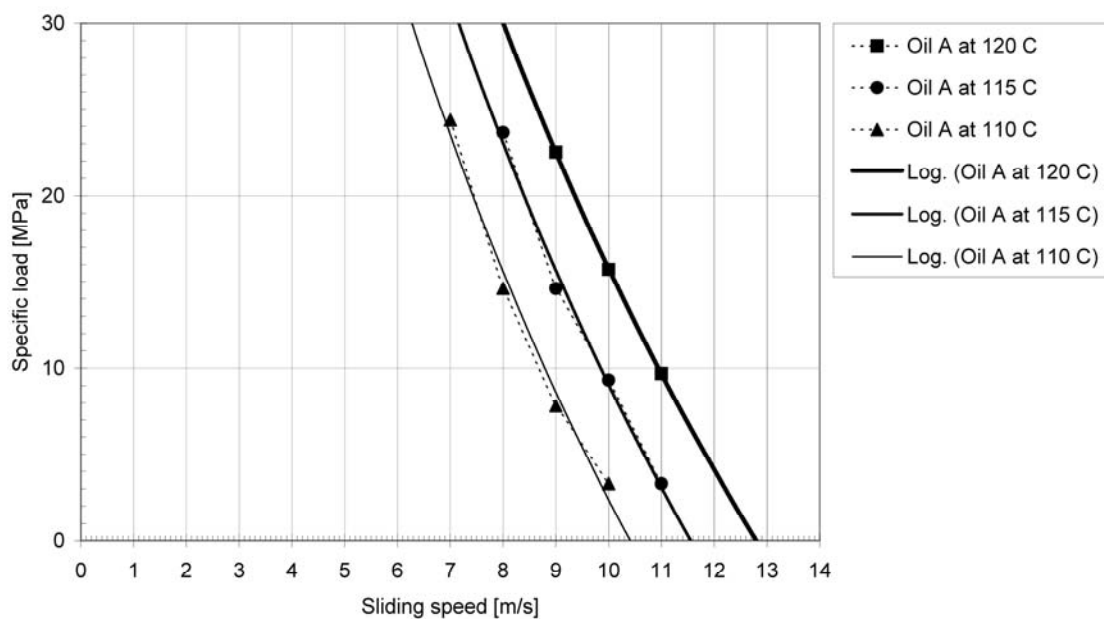


Figure 5-17. Specific load on the isotherms of the operating temperature with oil A. The isotherms of the operating temperature had logarithmic trend-lines with $R^2 > 0.90$.

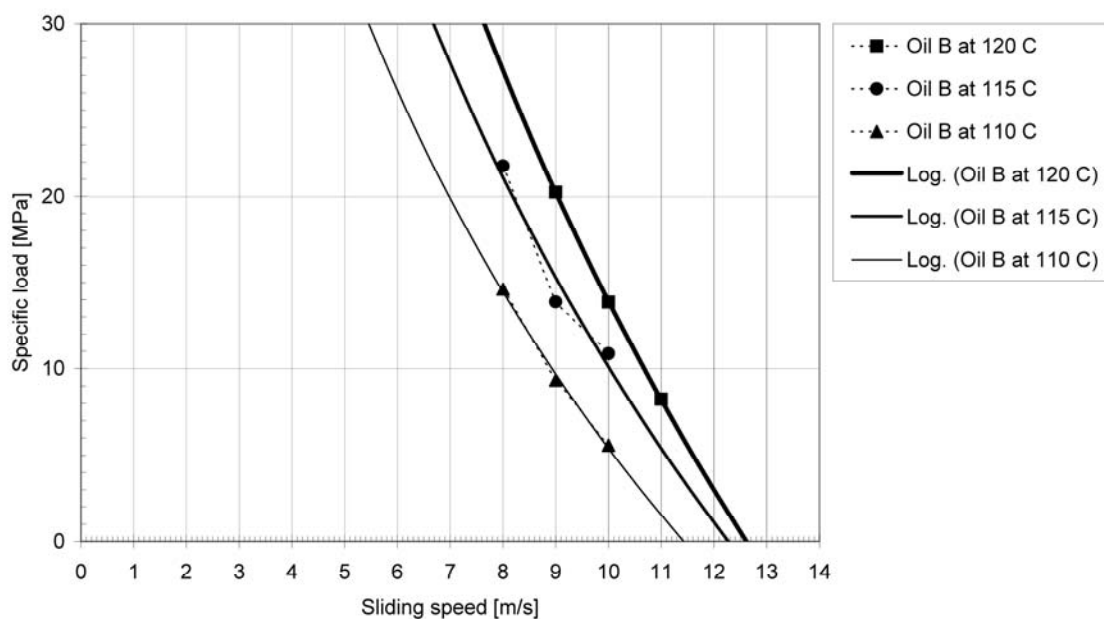


Figure 5-18. Specific load on the isotherms of the operating temperature with oil B. The isotherms of the operating temperature had logarithmic trend-lines with $R^2 > 0.90$.

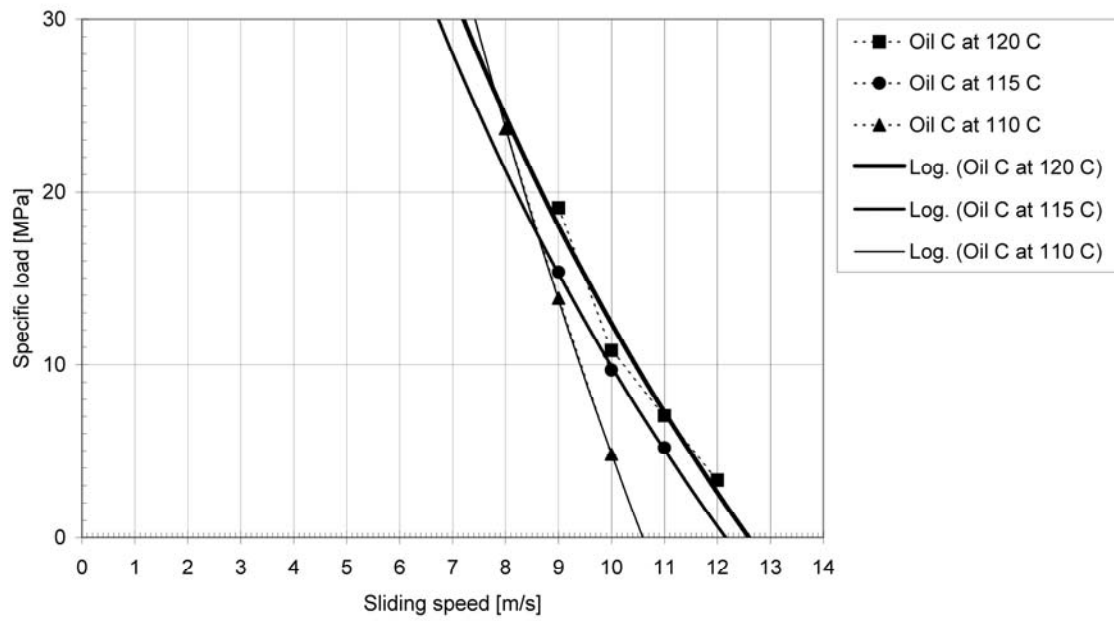


Figure 5-19. Specific load on the isotherms of the operating temperature with oil C. The isotherms of the operating temperature had logarithmic trend-lines with $R^2 > 0.90$.

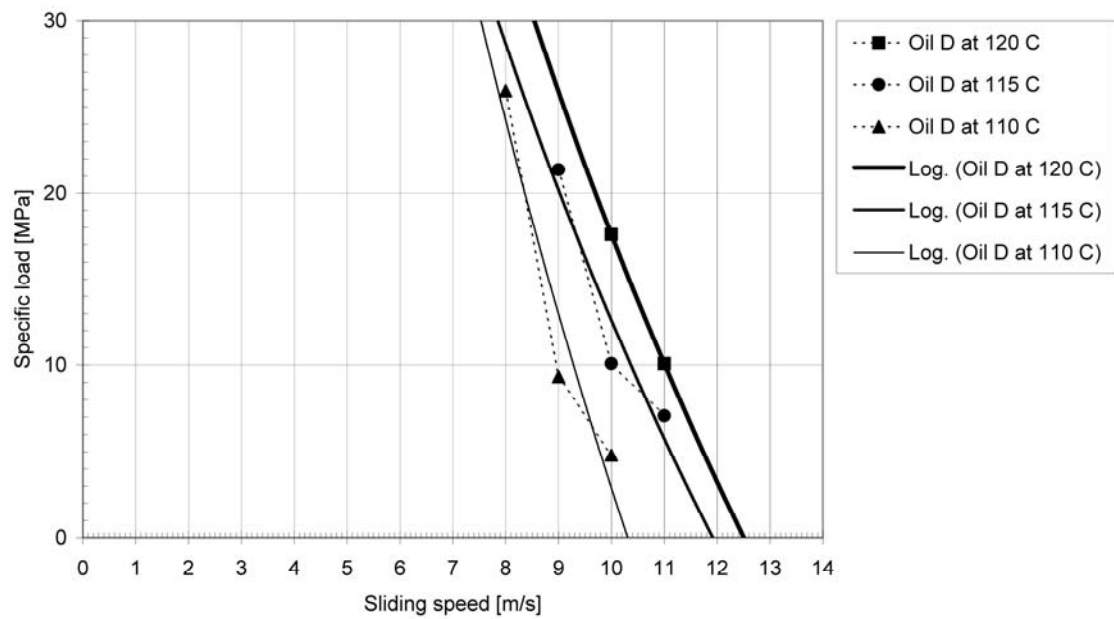


Figure 5-20. Specific load on the isotherms of the operating temperature with oil D. The isotherms of the operating temperature had logarithmic trend-lines with $R^2 > 0.90$.

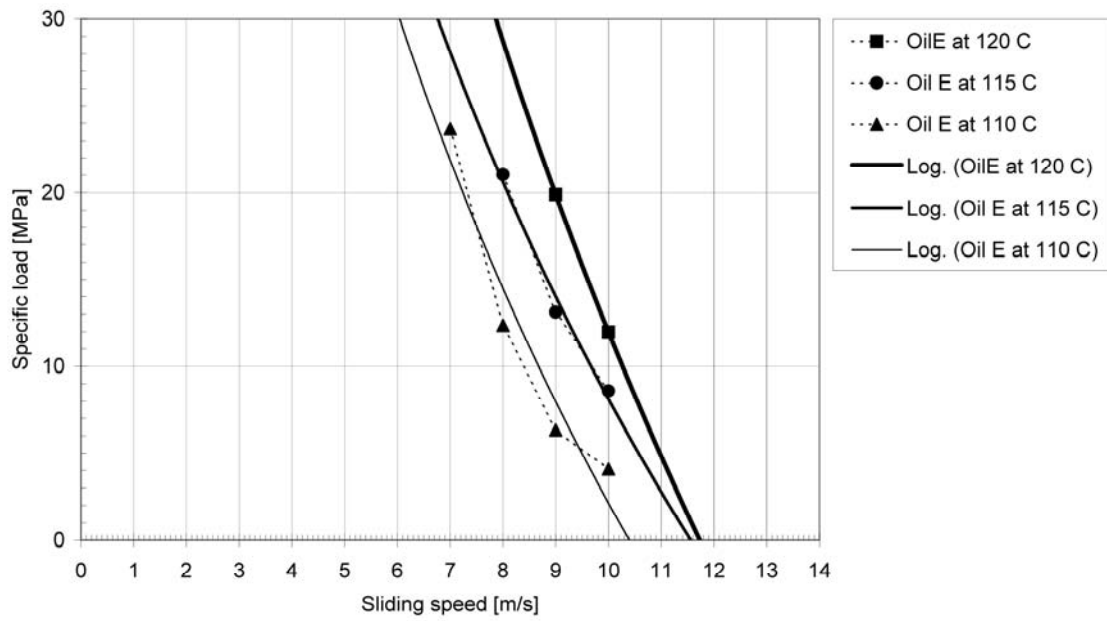


Figure 5-21. Specific load on the isotherms of the operating temperature with oil E. The isotherms of the operating temperature had logarithmic trend-lines with $R^2 > 0.90$.

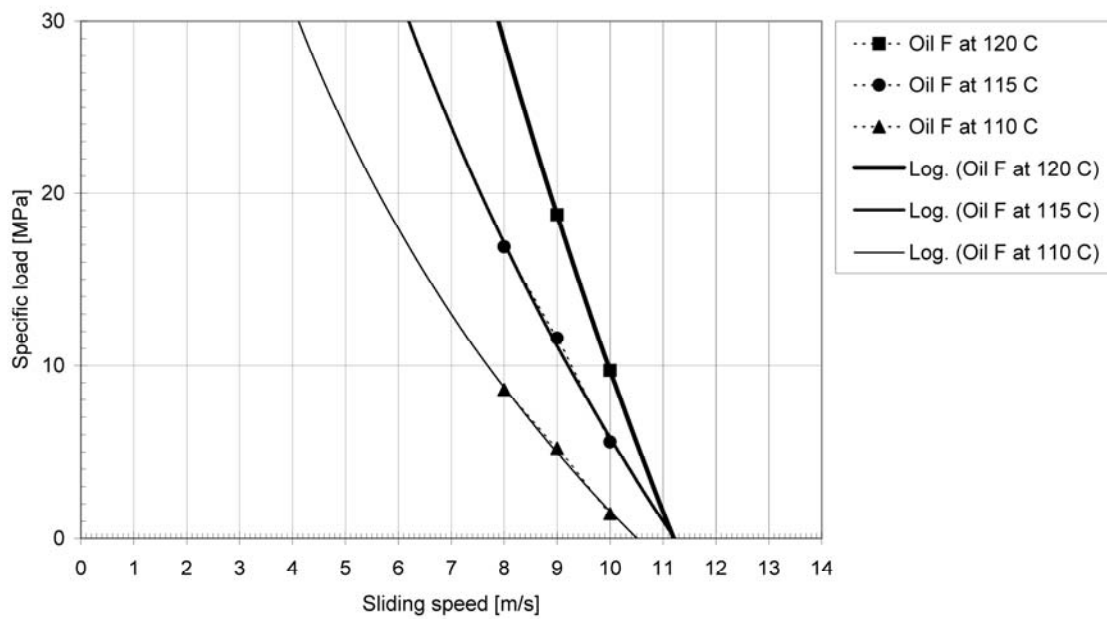


Figure 5-22. Specific load on the isotherms of the operating temperature with oil F. The isotherms of the operating temperature had logarithmic trend-lines with $R^2 > 0.90$.

The heat flow in convection through the housing with different oils at the sliding speed of 10 m/s is shown in Figure 5-23. The heat flow through the housing correlated roughly with the operating temperature. The heat flow through the housing was clearly less than the heat flow transferred by the lubricating oil, typically about 5 % of the total heat flow.

The heat flow transferred by different lubricating oils at the sliding speed of 10 m/s is shown in Figure 5-24. The heat flow transferred by the lubricating oil was clearly greater than the heat flow in convection through the housing, typically about 95 % of the total heat flow.

The total heat flow or friction power with different oils at the sliding speed of 10 m/s is shown in Figure 5-25. The friction power increased as the operating temperature increased.

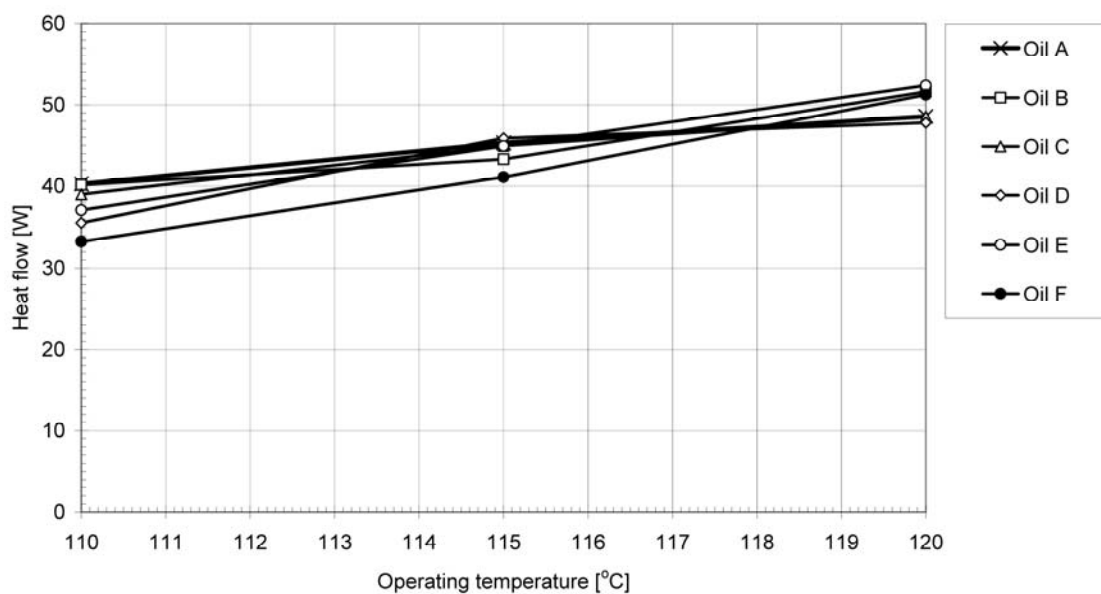


Figure 5-23. Heat flow in convection through the housing with different oils at the sliding speed of 10 m/s.

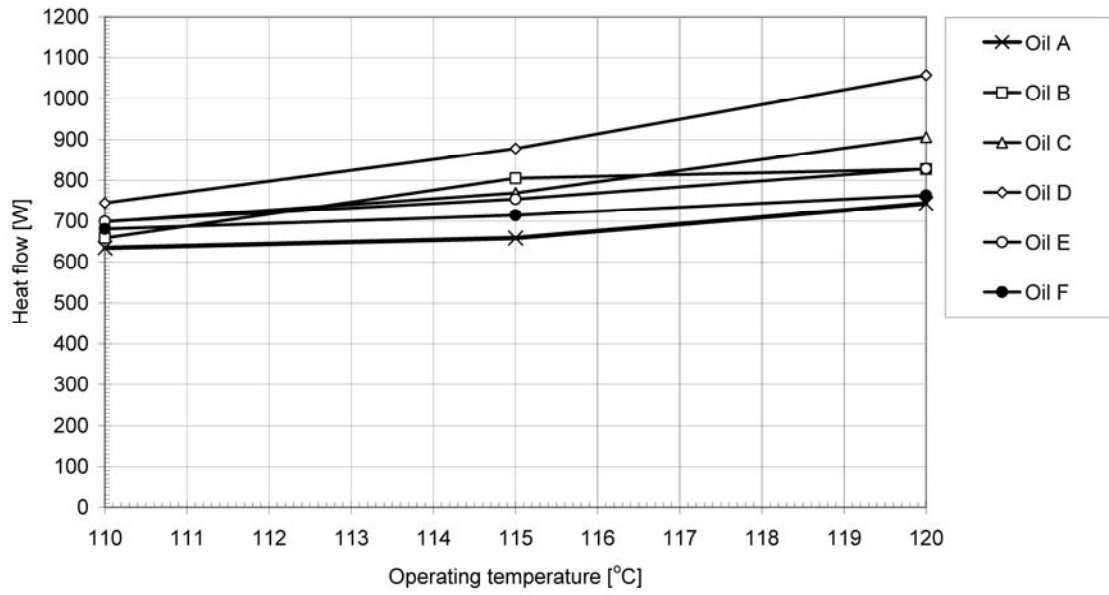


Figure 5-24. Heat flow transferred by different lubricating oils at the sliding speed of 10 m/s.

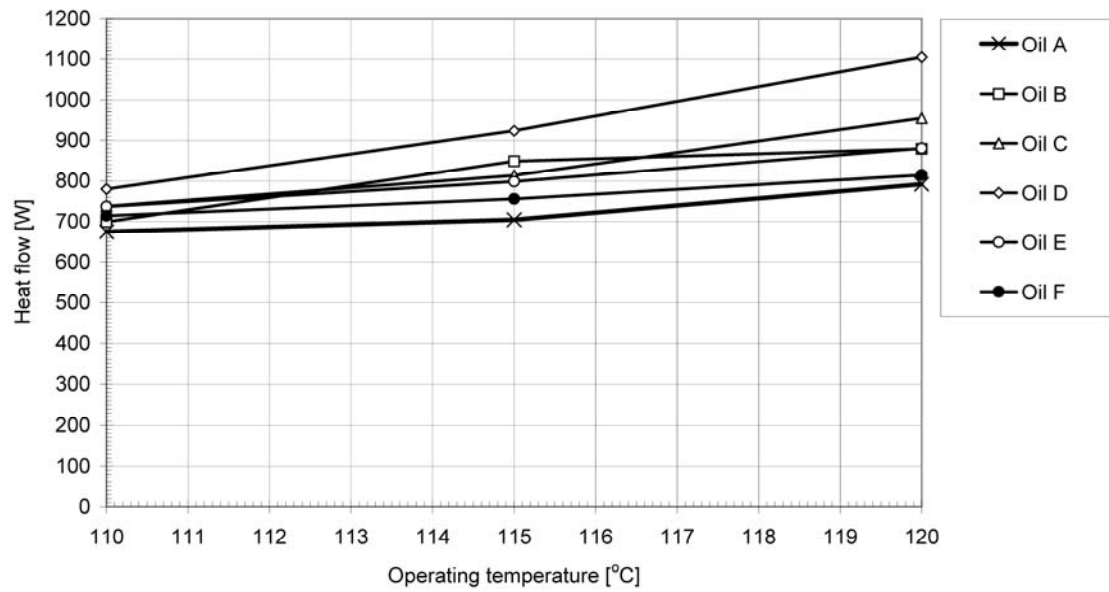


Figure 5-25. Total heat flow or friction power with different oils at the sliding speed of 10 m/s.

Power functions were found to describe the variations in friction power as a function of the specific load at the sliding speed of 10 m/s (see Figure 5-26). The power functions were determined by the method of least squares. The multipliers, exponents and coefficients of determination in the power functions are presented in Table 5-4.

Power functions were found to describe the variation in the friction coefficient as a function of the specific load at the sliding speed of 10 m/s (see Figure 5-27). The power functions were determined by the method of least squares. The multipliers, exponents and coefficients of determination of the power functions are presented in Table 5-5.

The above-mentioned power functions were used to calculate the friction coefficient (see Figure 5-28) and the relative friction coefficient (see Figure 5-29) at the specific loads of 5, 10, 15 and 20 MPa and at the sliding speed of 10 m/s. The relative friction coefficient was the ratio between the friction coefficient and the reference value. The friction coefficient calculated for oil A (that had the lowest viscosity index) was used as the reference value. Hence, the relative friction coefficient of oil A was exactly 1.0 at all specific load levels. In the case of the other oils (that have high viscosity indices), the relative friction coefficients typically increased sharply as the specific load increased. With oil F (which also had a high viscosity index), the relative friction coefficient decreased slightly as the specific load increased.

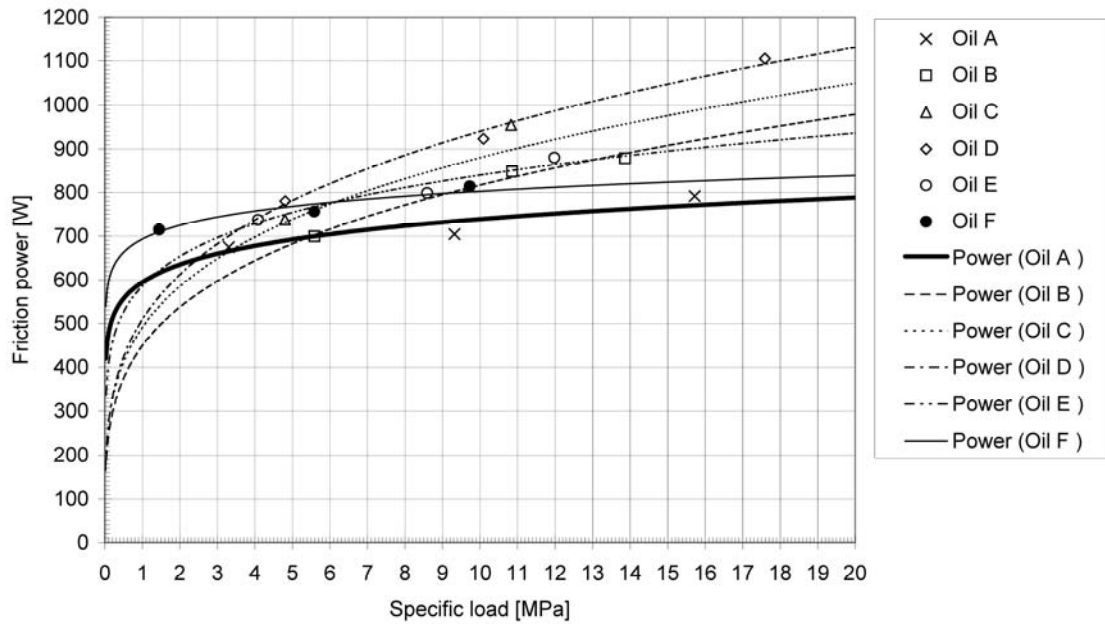


Figure 5-26. Friction power as a function of the specific load with different oils at the sliding speed of 10 m/s. The friction power had power function trend-lines with $R^2 > 0.7$.

Table 5-4. Multipliers k_3 , exponents k_4 and coefficients of determination (or R^2 -values) in the power functions $P_0 = k_3 p_s^{k_4}$ used to describe the friction power P_0 as a function of the specific load p_s .

	Oil A	Oil B	Oil C	Oil D	Oil E	Oil F
Multiplier k_3 []	595.293	449.143	490.934	509.334	586.798	693.160
Exponent k_4 []	0.093756	0.259964	0.253587	0.266140	0.155930	0.063847
Coefficient of determination []	0.811	0.985	0.740	0.990	0.929	0.903

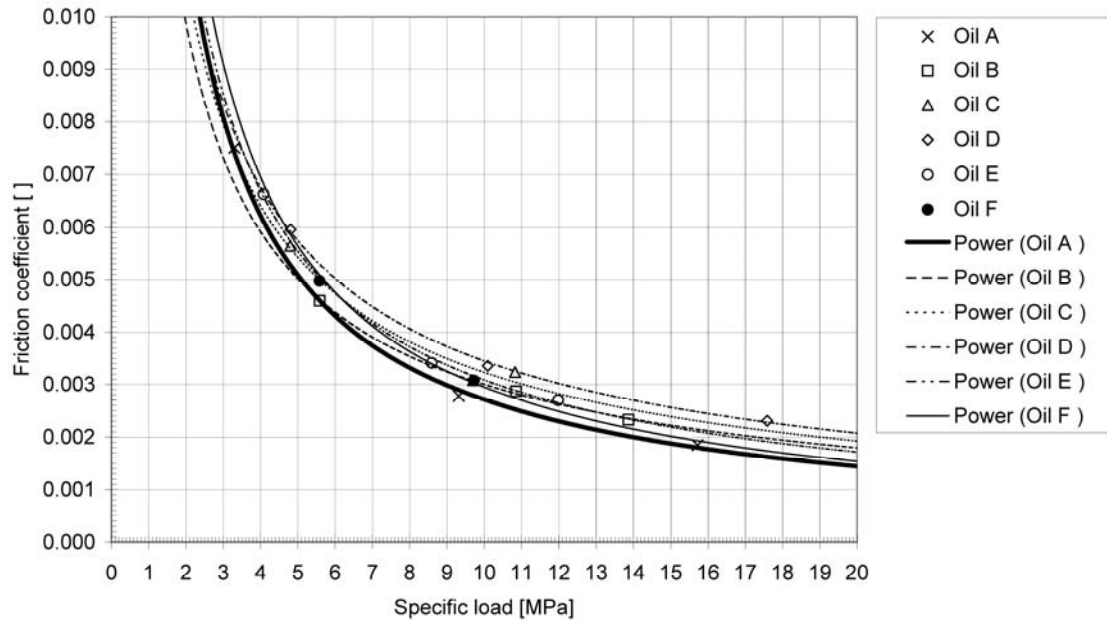


Figure 5-27. Friction coefficient as a function of the specific load with different oils at the sliding speed of 10 m/s. The friction coefficient had power function trend-lines with $R^2 > 0.9$.

Table 5-5. Multipliers k_3 , exponents k_4 and coefficients of determination (or R^2 values) in the power functions $\mu = k_3 p_s^{k_4}$ used to describe the friction coefficient μ as a function of the specific load p_s .

	Oil A	Oil B	Oil C	Oil D	Oil E	Oil F
Multiplier k_3 []	0.021861	0.016494	0.018028	0.018704	0.021549	0.025455
Exponent k_4 []	-0.906244	-0.740036	-0.746413	-0.733860	-0.844070	-0.936153
Coefficient of determination []	0.998	0.998	0.961	0.999	0.997	1.000

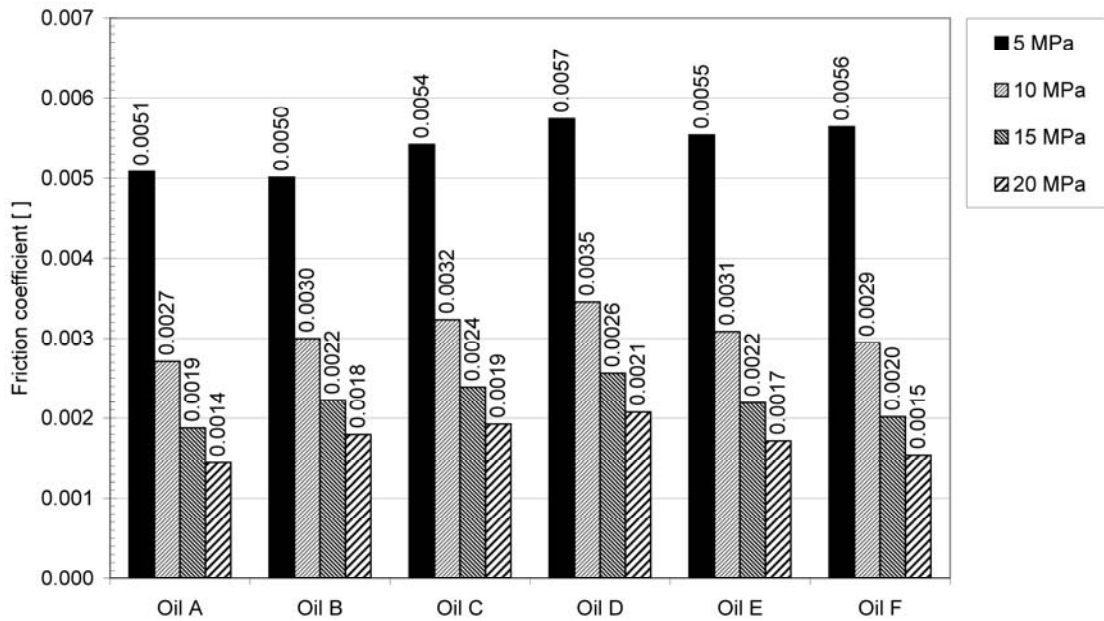


Figure 5-28. Friction coefficient at the specific loads of 5, 10, 15 and 20 MPa with different oils at the sliding speed of 10 m/s.

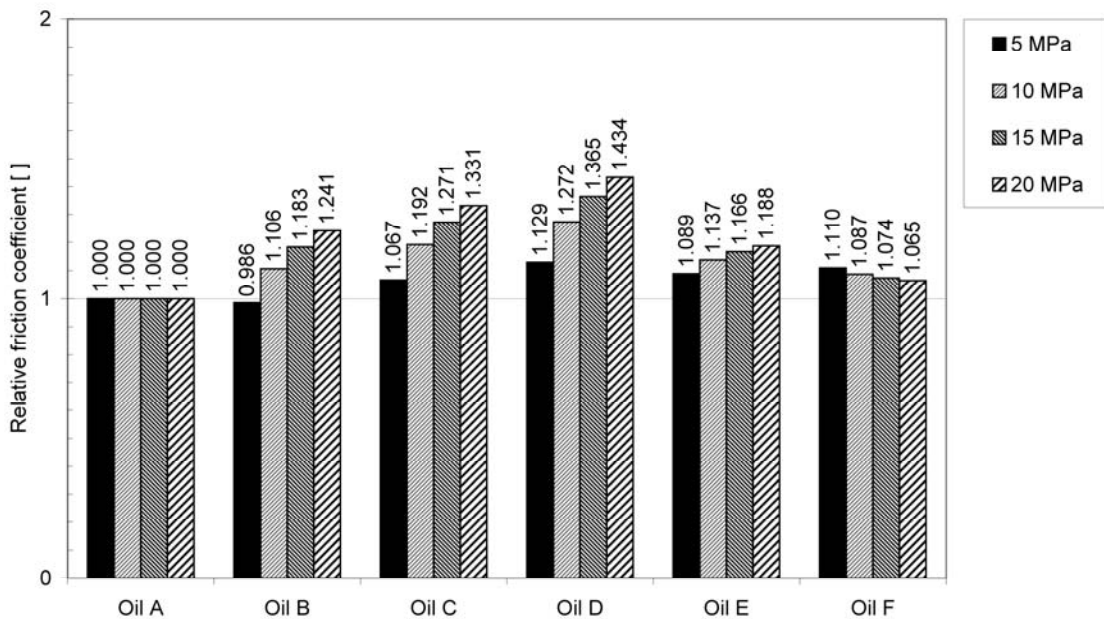


Figure 5-29. Relative friction coefficient at the specific loads of 5, 10, 15 and 20 MPa with different oils at the sliding speed of 10 m/s. For Oil A, the relative friction coefficient $\mu_{rel} = 1$.

5.3 Oil film pressure with a rotating load

The results from the study of the oil film pressure with a rotating load are presented below. The study included the Cases 1 and 2 of the pressure experiment set.

Case 1: Effect of the bearing load

The dimensions and operating parameters used for Case 1 of the pressure experiment set, with the bearing BD, shaft SC and housing HO, are shown in Table 5-6. The scaling of the oil film pressure data was based on results from the first calibration process (see Appendix E).

Table 5-6. Dimensions and operating parameters used for Case 1 of the pressure experiment set, with the bearing BD, shaft SC and housing HO. The lower sleeve of the bearing was grooved. The lubricating oil G was supplied through the shaft.

Dimension or parameter	Value
Diameter of the bearing [mm]	85.104
Diameter of the shaft [mm]	84.990
Bearing clearance [μm]	114
Relative bearing clearance [$1/10^3$]	1.3
Temperature of the housing [$^{\circ}\text{C}$]	70.3 ± 0.2
Inlet temperature [$^{\circ}\text{C}$]	70.2 ± 0.4
Inlet pressure [bar]	3.3 ± 0.1
Room temperature [$^{\circ}\text{C}$]	24.4 ± 2.1

The measured oil film pressure as a function of the angle of rotation with a rotating load is shown in Figure 5-30. The median, average and maximum values of the measured oil film pressure are presented in Figure 5-31. The simulated oil film pressure as a function of the angle of rotation is shown in Figure 5-32. The median, average and maximum values of the simulated oil film pressure are presented in Figure 5-33. The simulated

axial oil film pressure distribution at position angles between -24 and 9 degrees is presented in Figure 5-34. The simulated axial oil film pressure distribution at position angles between 9 and 27 degrees is presented in Figure 5-35. Using the simulated and measured oil film pressure distributions, the bearing load was determined as the resultant of the local forces (see Figure 5-36) caused by the local oil film pressures on the local surface areas. Determination of the resultant of the local forces is presented in Appendix H.

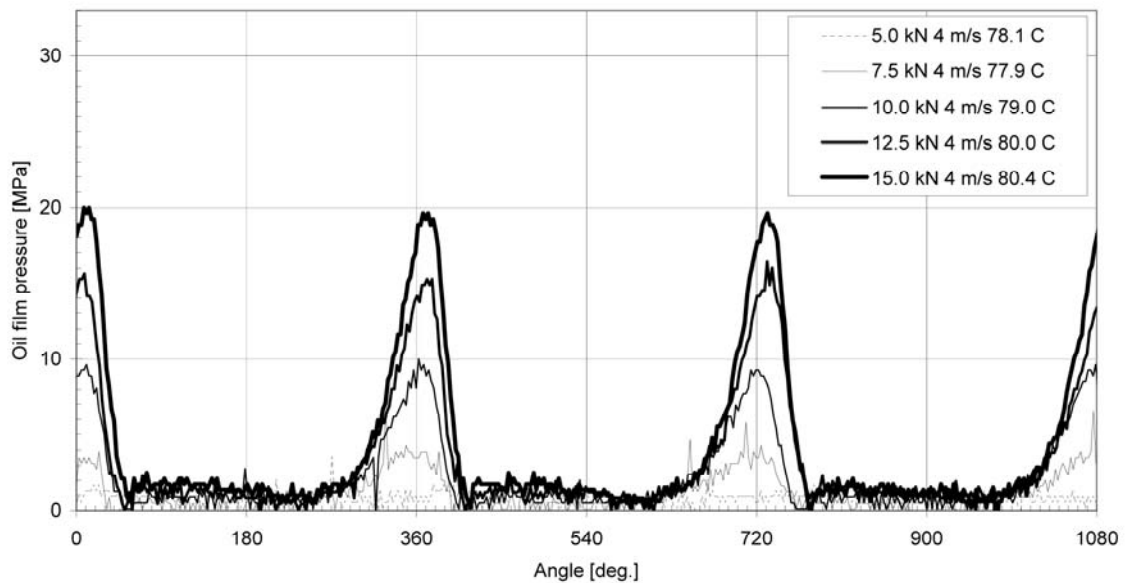


Figure 5-30. Measured oil film pressure with a rotating load. Effect of the bearing load on the oil film pressure. Sliding speed was 4 m/s. The bearing load was 5.0 to 15.0 kN. The specific load was 1.8 to 5.5 MPa. The inlet temperature was 70 °C. The inlet pressure was 3 bar.

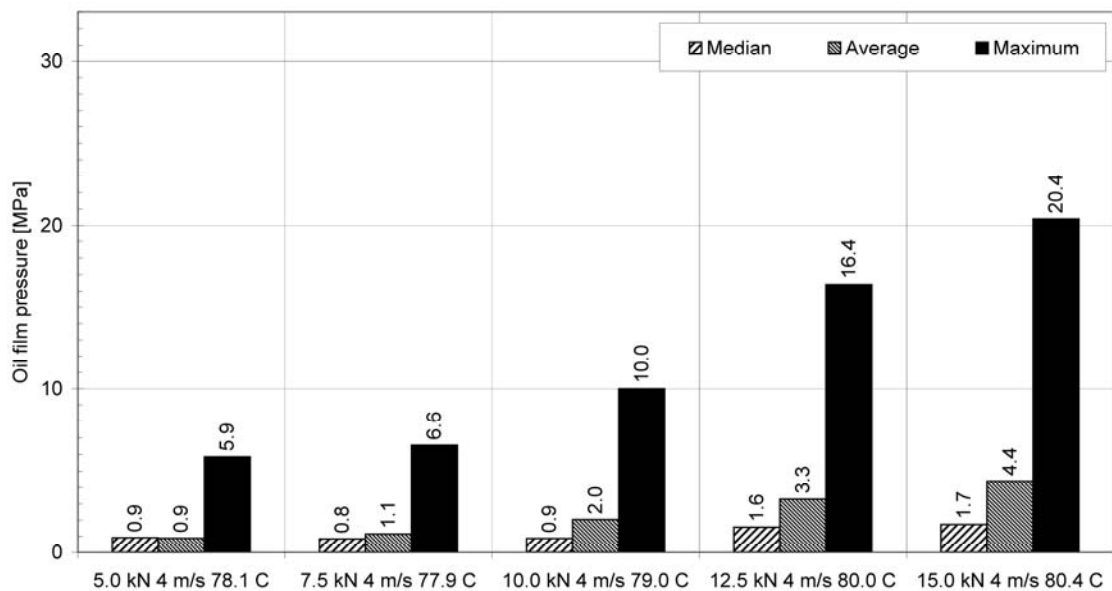


Figure 5-31. Median, average and maximum values of the measured oil film pressure with a rotating load. The sliding speed was 4 m/s. The bearing load was 5.0 to 15.0 kN. The specific load was 1.8 to 5.5 MPa. The inlet temperature was 70 °C. The inlet pressure was 3 bar.

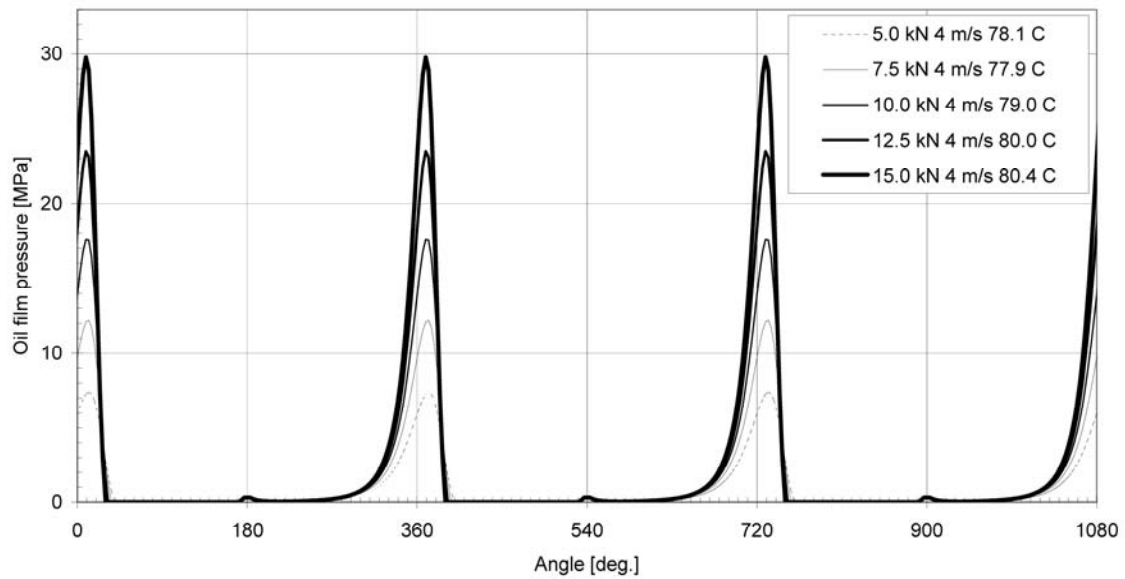


Figure 5-32. Simulated oil film pressure with a rotating load. Effect of the bearing load on the oil film pressure. The sliding speed was 4 m/s. The bearing load was 5.0 to 15.0 kN. The specific load was 1.8 to 5.5 MPa. The inlet temperature was 70 °C. The inlet pressure was 3 bar.

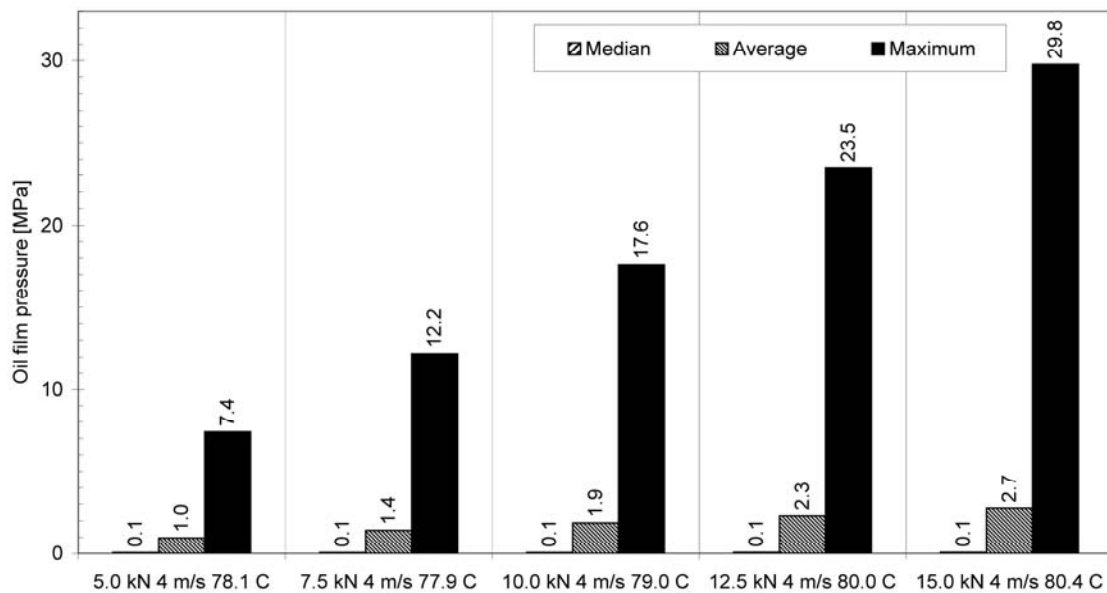


Figure 5-33. Median, average and maximum values of the simulated oil film pressure with a rotating load. The sliding speed was 4 m/s. The bearing load was 5.0 to 15.0 kN. The specific load was 1.8 to 5.5 MPa. The inlet temperature was 70 °C. The inlet pressure was 3 bar.

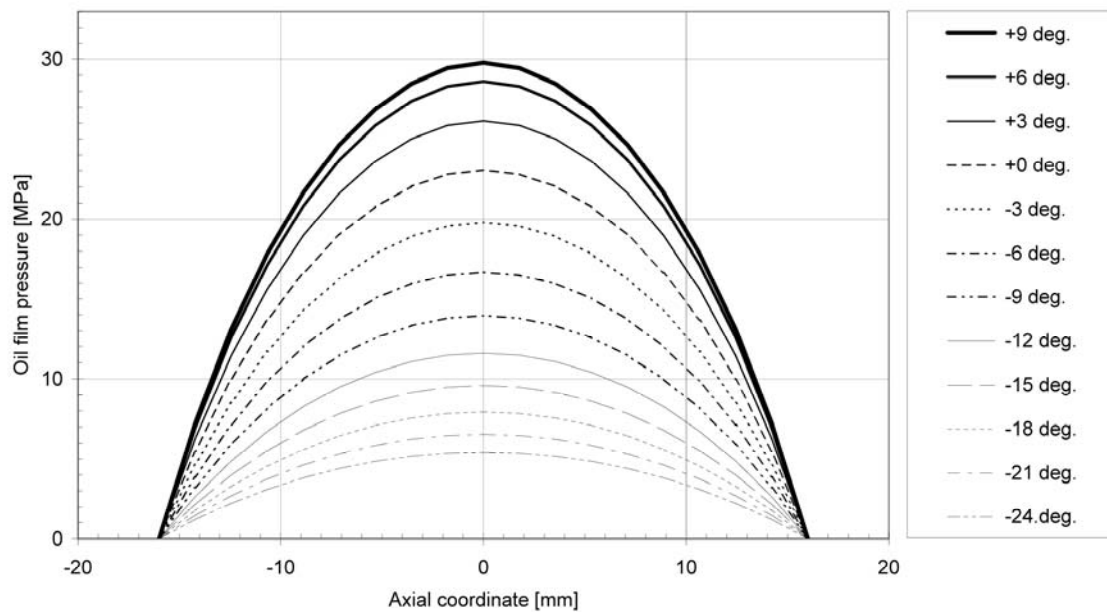


Figure 5-34. Simulated axial oil film distribution with position angles between -24 and 9 degrees. The sliding speed was 4 m/s. The bearing load was 15.0 kN. The specific load was 5.5 MPa. The operating temperature was 80.4 °C. The inlet temperature was 70 °C. The inlet pressure was 3 bar.

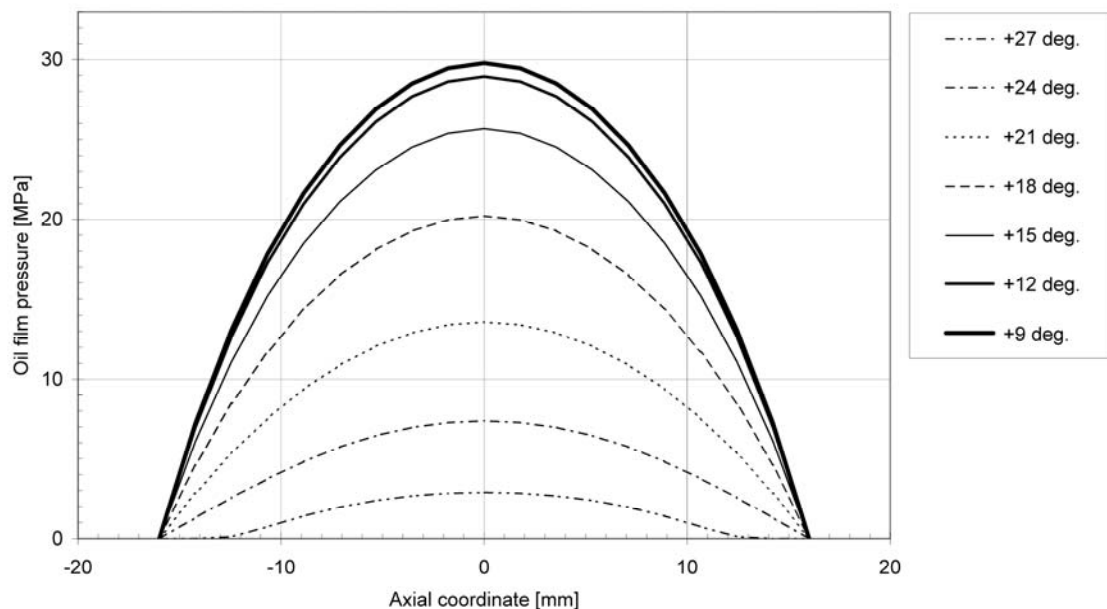


Figure 5-35. Simulated axial oil film distribution with position angles between 9 and 27 degrees. The sliding speed was 4 m/s. The bearing load was 15.0 kN. The specific load was 5.5 MPa. The operating temperature was 80.4 °C. The inlet temperature was 70 °C. The inlet pressure was 3 bar.

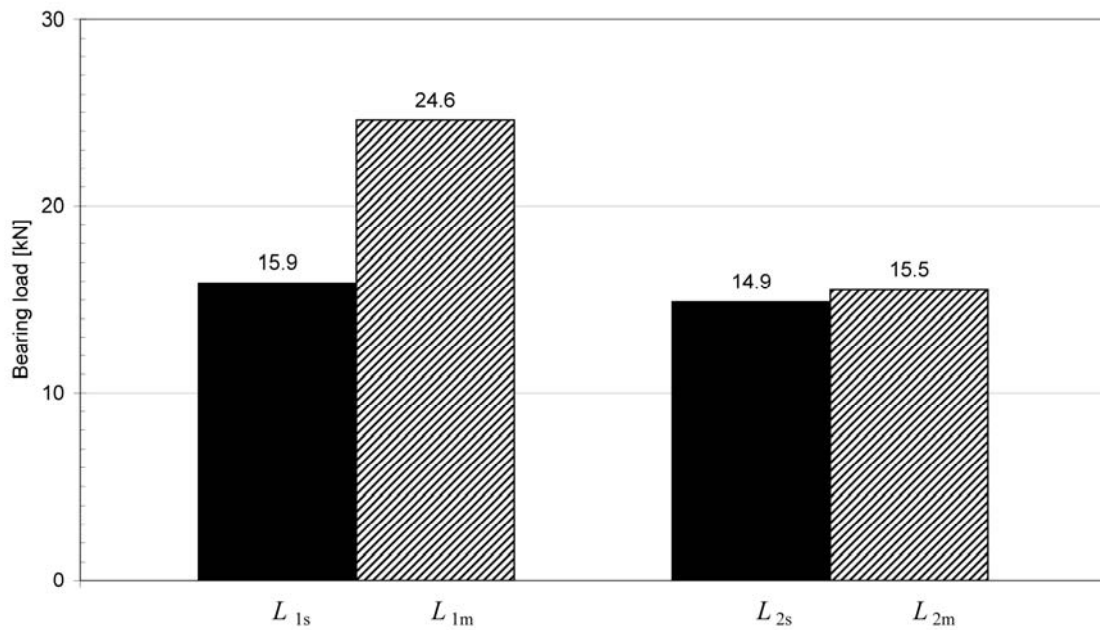


Figure 5-36. Bearing load determined as the resultant of the local radial forces. The sliding speed was 4 m/s. The bearing load was 15.0 kN. The specific load was 5.5 MPa. The operating temperature was 80.4 °C. The inlet temperature was 70 °C. The inlet pressure was 3 bar. The resultants L_{1s} and L_{2s} are based on the simulated oil film pressure and the resultants L_{1m} and L_{2m} are based on the measured oil film pressure. In the resultants L_{1s} and L_{1m} , the directions of the local radial forces were ignored. The resultants were arithmetic sums of the local radial forces. In the resultants L_{2s} and L_{2m} , the directions of the local radial forces were taken into account.

Case 2: Effect of the sliding speed

The dimensions and operating parameters used for Case 2 of the pressure experiment set, with the bearing BD, shaft SC and housing HO, are shown in Table 5-7. The scaling of the oil film pressure data was based on results from the first calibration process (see Appendix E).

Table 5-7. Dimensions and operating parameters used for Case 2 of the pressure experiment set, with the bearing BD, shaft SC and housing HO. The lower sleeve of the bearing was grooved. The lubricating oil G was supplied through the shaft.

Dimension or parameter	Value
Diameter of the bearing [mm]	85.104
Diameter of the shaft [mm]	84.990
Bearing clearance [μm]	114
Relative bearing clearance [$1/10^3$]	1.3
Temperature of the housing [$^{\circ}\text{C}$]	71.5 ± 0.4
Inlet temperature [$^{\circ}\text{C}$]	70.1 ± 0.4
Inlet pressure [bar]	3.4 ± 0.1
Room temperature [$^{\circ}\text{C}$]	22.7 ± 1.3

The measured oil film pressure as a function of the angle of rotation with a rotating load is shown in Figure 5-37. The median, average and maximum values of the measured oil film pressure are presented in Figure 5-38. The simulated oil film pressure as a function of the angle of rotation is shown in Figure 5-39. The median, average and maximum values of the simulated oil film pressure are presented in Figure 5-40.

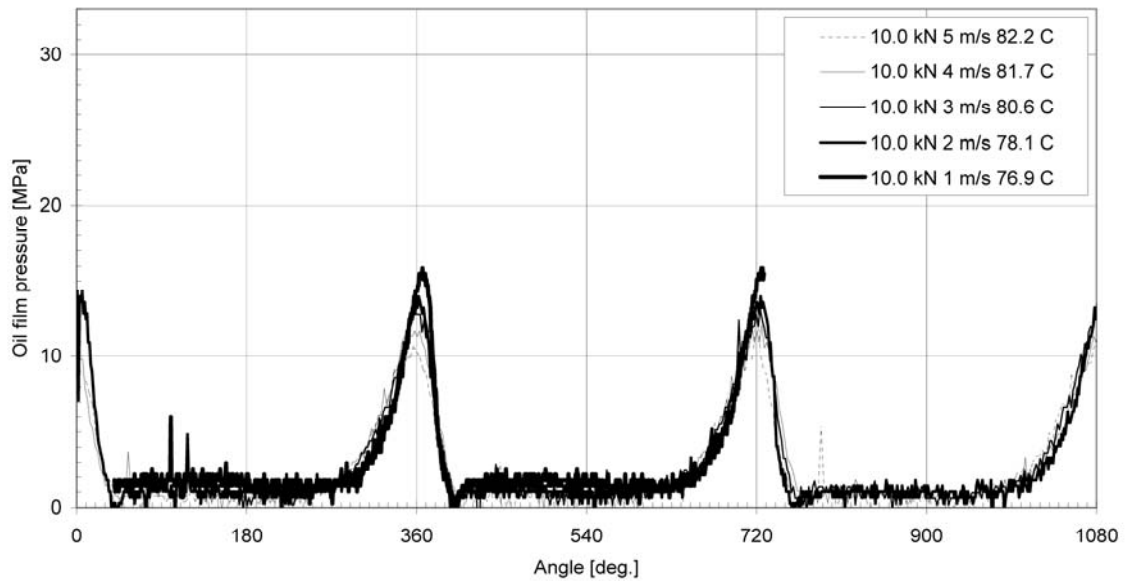


Figure 5-37. Measured oil film pressure with a rotating load. Effect of the sliding speed on the oil film pressure. The sliding speed was 1 to 5 m/s. The bearing load and the specific load were 10 kN and 3.7 MPa, respectively. The inlet temperature was 70 °C. The inlet pressure was 3 bar.

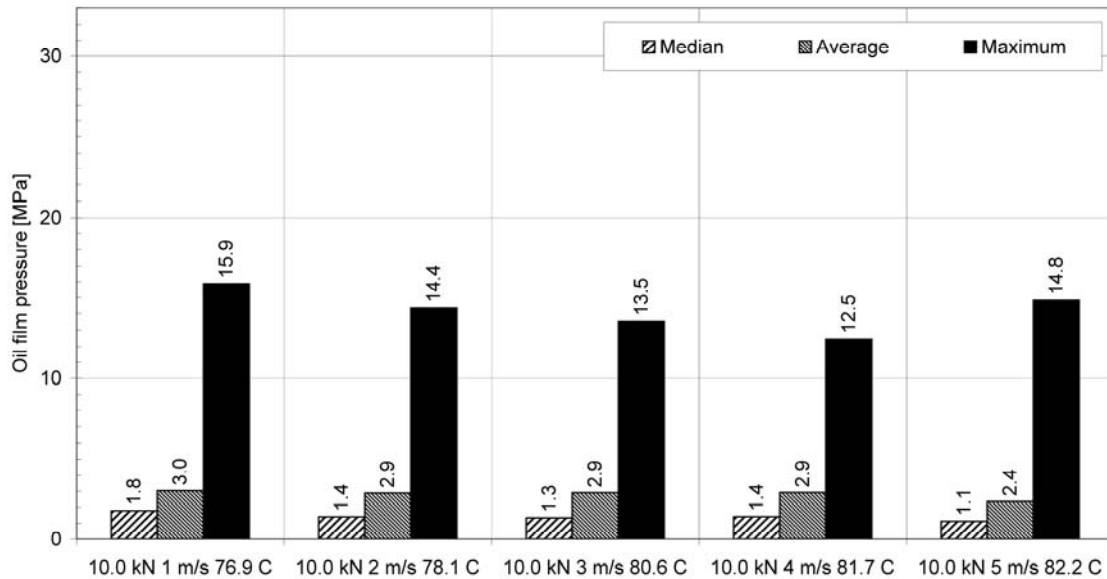


Figure 5-38. Median, average and maximum values of the measured oil film pressure with a rotating load. The sliding speed was 1 to 5 m/s. The bearing load and the specific load were 10 kN and 3.7 MPa, respectively. The inlet temperature was 70 °C. The inlet pressure was 3 bar.

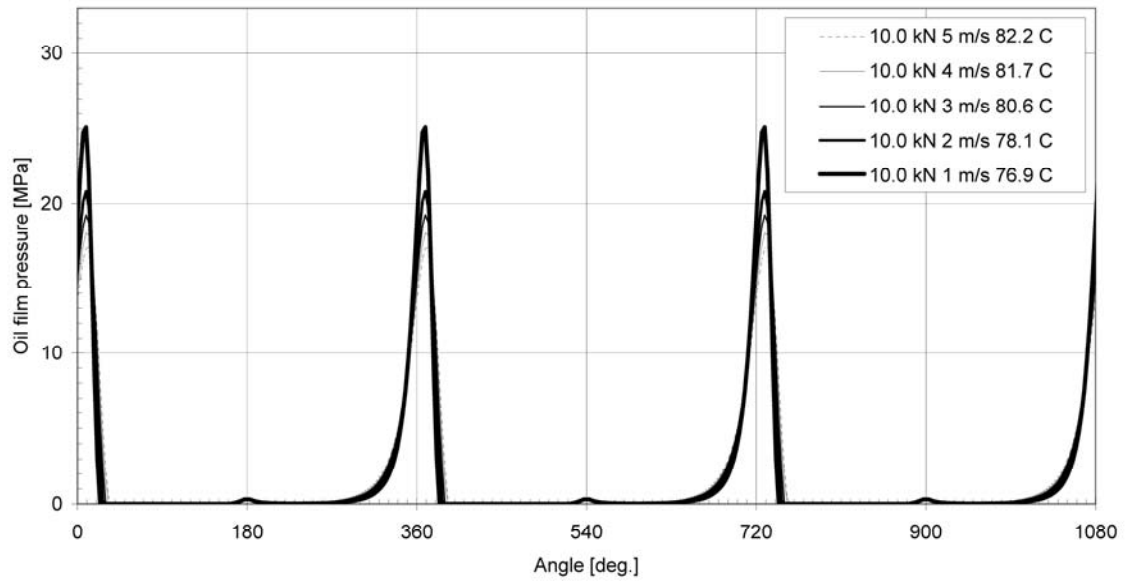


Figure 5-39. Simulated oil film pressure with a rotating load. Effect of the sliding speed on the oil film pressure. The sliding speed was 1 to 5 m/s. The bearing load and the specific load were 10 kN and 3.7 MPa, respectively. The inlet temperature was 70 °C. The inlet pressure was 3 bar.

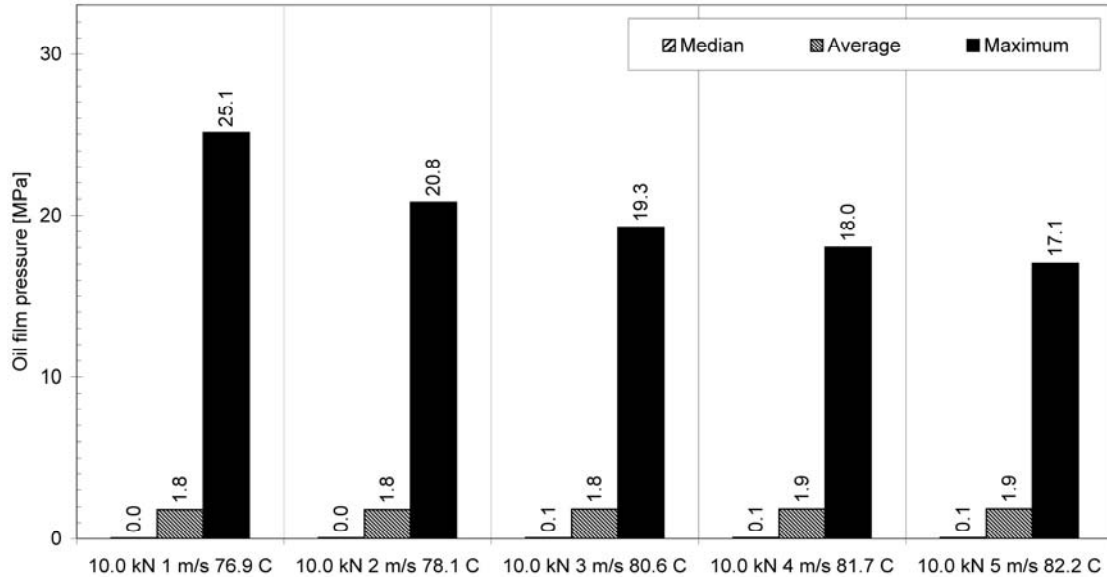


Figure 5-40. Median, average and maximum values of the simulated oil film pressure with a rotating load. The sliding speed was 1 to 5 m/s. The bearing load and the specific load were 10 kN and 3.7 MPa, respectively. The inlet temperature was 70 °C. The inlet pressure was 3 bar.

5.4 Oil film pressure with a static load

The results from the study of oil film pressure with a static load are presented below. The study included Cases 3 and 4 of the set pressure experiment set.

Case 3: Effect of the bearing load

The dimensions and operating parameters used for Case 3 of the pressure experiment set, with the bearing BD, shaft SC and housing HO, are shown in Table 5-8. The scaling of the oil film pressure data was based on results from the third calibration process (see Appendix E).

Table 5-8. Dimensions and operating parameters used for Case 3 of the pressure experiment set, with the bearing BD, shaft SC and housing HO. The lower sleeve of the bearing was grooved. The lubricating oil G was supplied through the shaft.

Dimension or parameter	Value
Diameter of the bearing [mm]	85.104
Diameter of the shaft [mm]	84.990
Bearing clearance [μm]	114
Relative bearing clearance [$1/10^3$]	1.3
Temperature of the housing [$^{\circ}\text{C}$]	89.0 ± 0.5
Inlet temperature [$^{\circ}\text{C}$]	71.3 ± 0.2
Inlet pressure [bar]	4.5 ± 0.2
Room temperature [$^{\circ}\text{C}$]	About 25

The measured oil film pressure as a function of the angle of rotation with a static load is shown in Figure 5-41. There was regular fluctuation in the measurement signal (see Figure 5-42). The measured oil film pressure with a static load collapsed to zero as the oil-feeding hole in the shaft crossed the measurement point (see Figure 5-43). The average, median and maximum values of the measured oil film pressure at the three measurement points are presented in Figure 5-44. The simulated oil film pressure is shown as a function of the angle of rotation in Figure 5-45. As the simulated oil film pressure was presented as a function of the position angle (see Figure 5-46), it was found that the shape of the simulated oil film pressure distribution with a static load and the shape with a rotating load (see Figure 5-32, for example) resembled each other. They both included sharp “pressure waves” (areas of high pressure in the oil film) with a smoothly increasing gradient on the left side and a sharply decreasing gradient on the right side. The major difference between those “pressure waves” was that the one with a rotating load moved along the sliding surface of the bearing at the sliding speed, but the one with a static load was stationary. The sensor position angles are shown in the Figure 5-46 so that the measured and simulated data may be compared. It was found that area of the simulated “pressure wave” did not cover all the measurement points where relatively high oil film pressures were measured. The above-mentioned result showed that the measured “oil film pressure wave” was wider than the simulated one. The highest measured oil film pressures were clearly lower than the simulated ones, but higher than the maximum oil pressure (500 bar) used in the calibration. The highest measured oil film pressures were about 87 to 135 MPa (see Figure 5-44) and the highest simulated oil film pressures were about 270 to 500 MPa (see Figure 5-46).

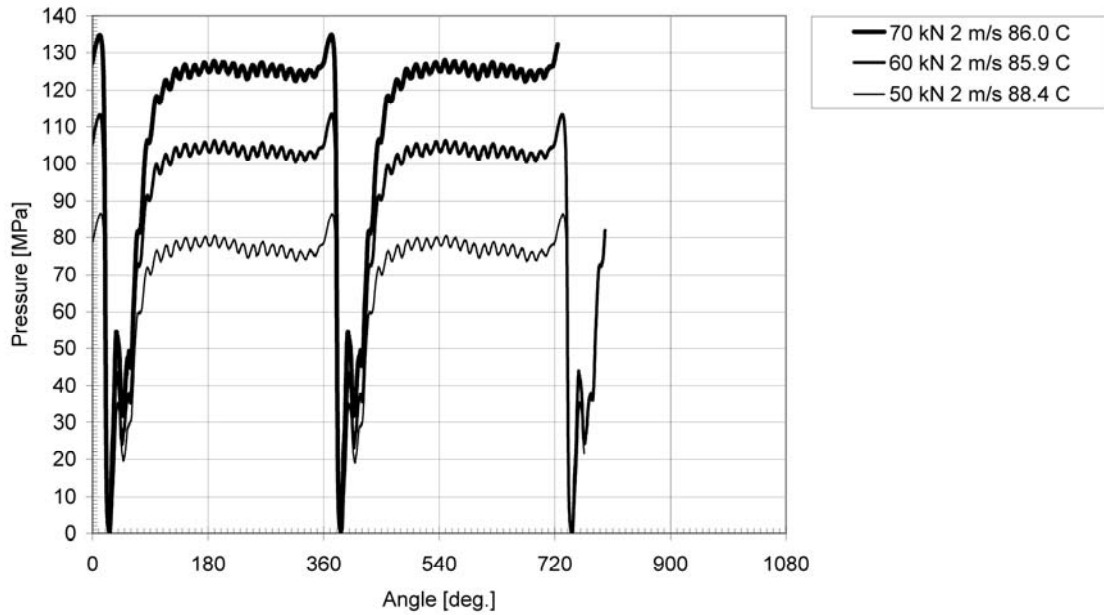


Figure 5-41. Measured oil film pressure with a static load. Effect of the load on the oil film pressure. The bearing load was 50, 60 and 70 kN. The sliding speed was 2 m/s. The inlet temperature was 71 °C. The inlet pressure was 4.5 bar. The optical pressure sensor was located at measurement point 5. The sensor position angle was $27 + N \times 360$ degrees ($N = 0, 1, 2, \dots$).

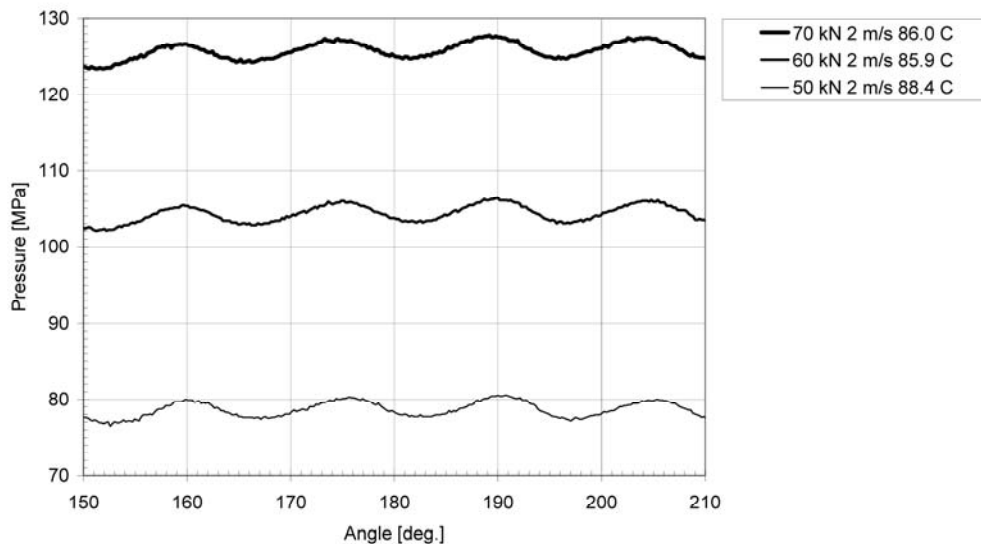


Figure 5-42. Fluctuation in the measured oil film pressure with a static load. The bearing load was 50, 60 and 70 kN. The sliding speed was 2 m/s. The inlet temperature was 71 °C. The inlet pressure was 4.5 bar. The optical pressure sensor was located at measurement point 5. The sensor position angle was $27 + N \times 360$ degrees ($N = 0, 1, 2, \dots$).

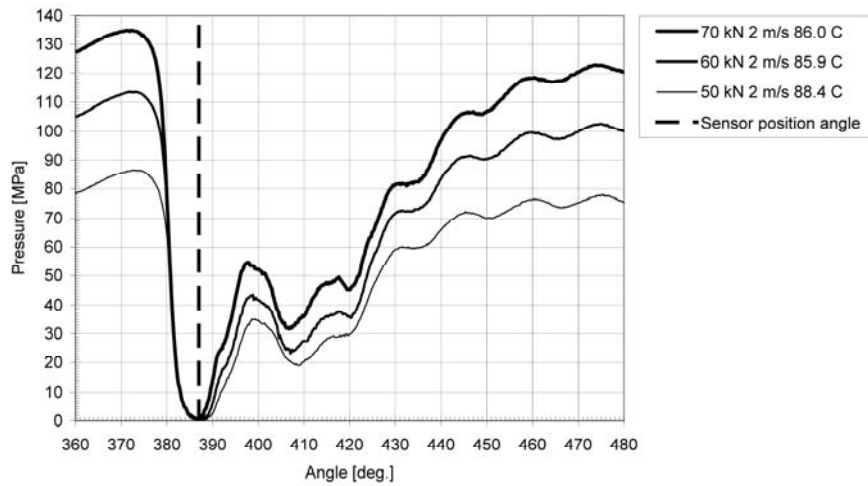


Figure 5-43. Measured oil film pressure with a static load as the oil-feeding hole in the shaft crossed the measurement point. The bearing load was 50, 60 and 70 kN. The sliding speed was 2 m/s. The inlet temperature was 71 °C. The inlet pressure was 4.5 bar. The optical pressure sensor was located at measurement point 5. The sensor position angle was $27 + N \times 360$ degrees ($N = 0, 1, 2, \dots$).

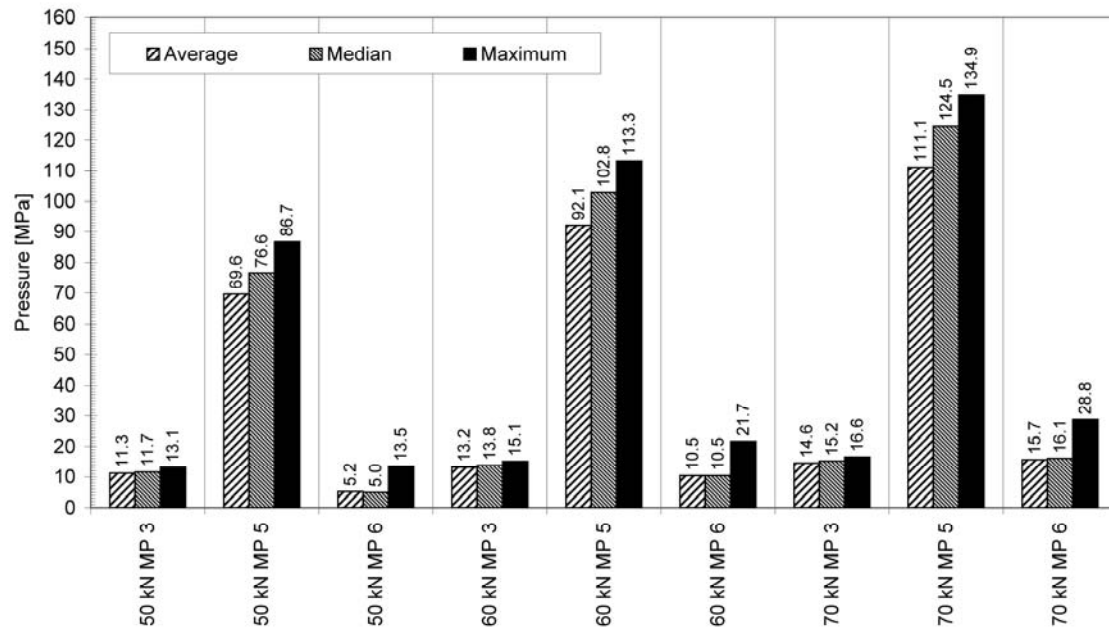


Figure 5-44. Average, median and maximum values of the measured oil film pressure at three measurement points with a static load. The bearing load was 50, 60 and 70 kN. The sliding speed was 2 m/s. The inlet temperature was 71 °C. The inlet pressure was 4.5 bar. The optical pressure sensors were located at measurement points (MP) 3, 5 and 6.

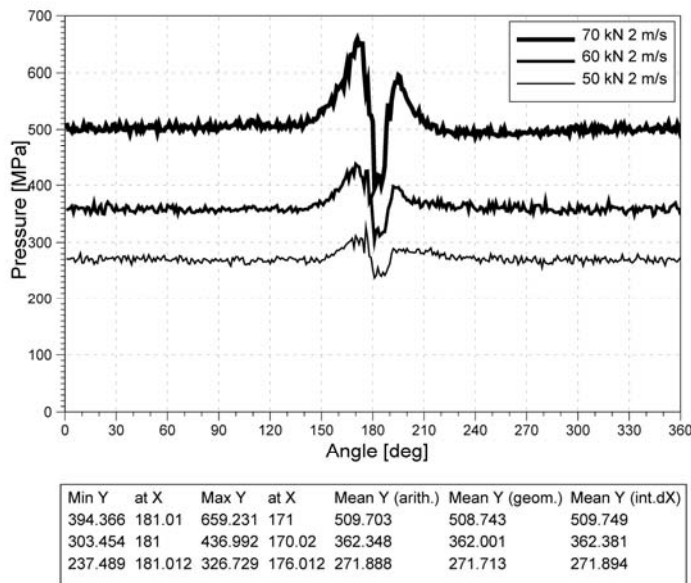


Figure 5-45. Simulated oil film pressure as a function of the angle of rotation with a static load. The bearing load was 50, 60 and 70 kN. The sliding speed was 2 m/s.

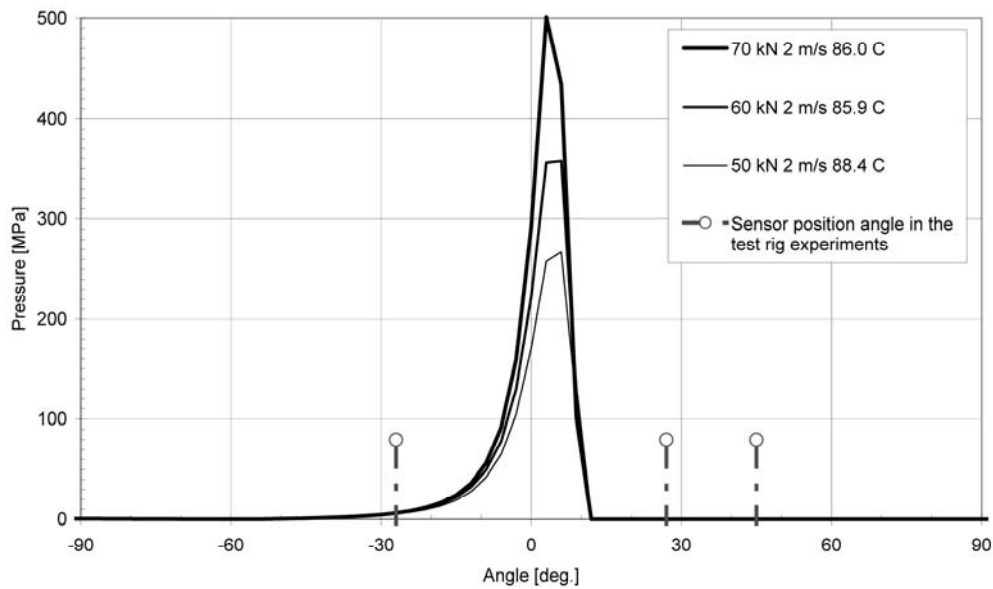


Figure 5-46. Simulated oil film pressure as a function of the position angle with a static load. The bearing load was 50, 60 and 70 kN. The sliding speed was 2 m/s. Note that the area of high oil film pressure does not cover all pressure-measurement points used in the test rig experiments.

Case 4: Effect of the sliding speed

The dimensions and operating parameters used for Case 4 of the pressure experiment set, with the bearing BD, shaft SC and housing HO, are shown in Table 5-9. The scaling of the oil film pressure data was based on results from the third calibration process (see Appendix E).

Table 5-9. Dimensions and operating parameters used for Case 4 of the pressure experiment set, with the bearing BD, shaft SC and housing HO. The lower sleeve of the bearing was grooved. The lubricating oil G was supplied through the shaft.

Dimension or parameter	Value
Diameter of the bearing [mm]	85.104
Diameter of the shaft [mm]	84.990
Bearing clearance [μm]	114
Relative bearing clearance [$1/10^3$]	1.3
Temperature of the housing [$^{\circ}\text{C}$]	89.0 ± 0.5
Inlet temperature [$^{\circ}\text{C}$]	71.1 ± 0.4
Inlet pressure [bar]	4.6 ± 0.1
Room temperature [$^{\circ}\text{C}$]	About 25

The measured oil film pressure as a function of the angle of rotation with a static load is presented in Figure 5-47. There was a regular amount of fluctuation in the measurement signal (see Figure 5-48). The measured oil film pressure collapsed to zero as the radial oil-feeding hole in the shaft crossed the measurement point (see Figure 5-49). The average, median and maximum values of the measured oil film pressure at the three measurement points are shown in Figure 5-50. The simulated oil film pressure is presented as a function of the angle of rotation in Figure 5-51. In this case, the shape of the simulated oil film pressure distribution with a static load (see Figure 5-52) and the shape with a rotating load (see Figure 5-39, for example) also resembled each other. They included sharp “pressure waves” (areas of high pressure in the oil film), with a smoothly increasing gradient on the left side and a rapidly decreasing gradient on the

right side. The area of the simulated “pressure wave” did not cover all the measurement points where relatively high oil film pressures were measured (see Figure 5-52). The above-mentioned result showed that the measured “oil film pressure wave” was wider than the simulated one. The highest measured oil film pressures were clearly lower than the simulated ones, but higher than the maximum oil pressure (500 bar) used in the calibration. The highest measured oil film pressures were about 82 to 103 MPa (see Figure 5-50) and the highest simulated oil film pressures were about 190 to 270 MPa (see Figure 5-52).

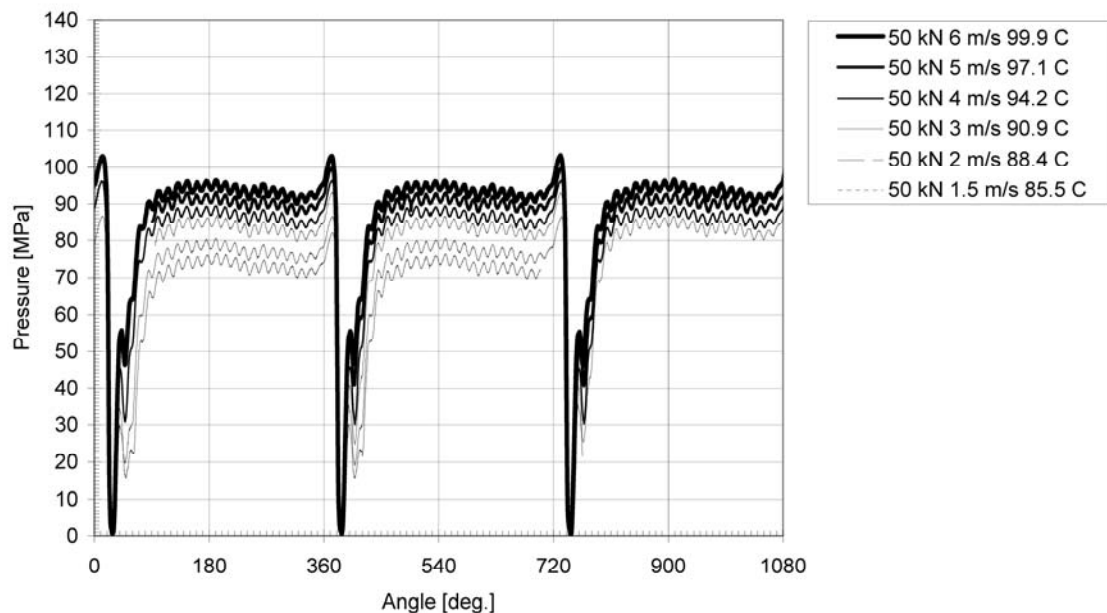


Figure 5-47. Measured oil film pressure with a static load. Effect of the sliding speed on the oil film pressure. The bearing load was 50 kN. The sliding speed was 1.5 to 6 m/s. The inlet temperature was 71 °C. The inlet pressure was 4.6 bar. The optical pressure sensor was located at measurement point 5. The sensor position angle was $27 + N \times 360$ degrees ($N = 0, 1, 2 \dots$).

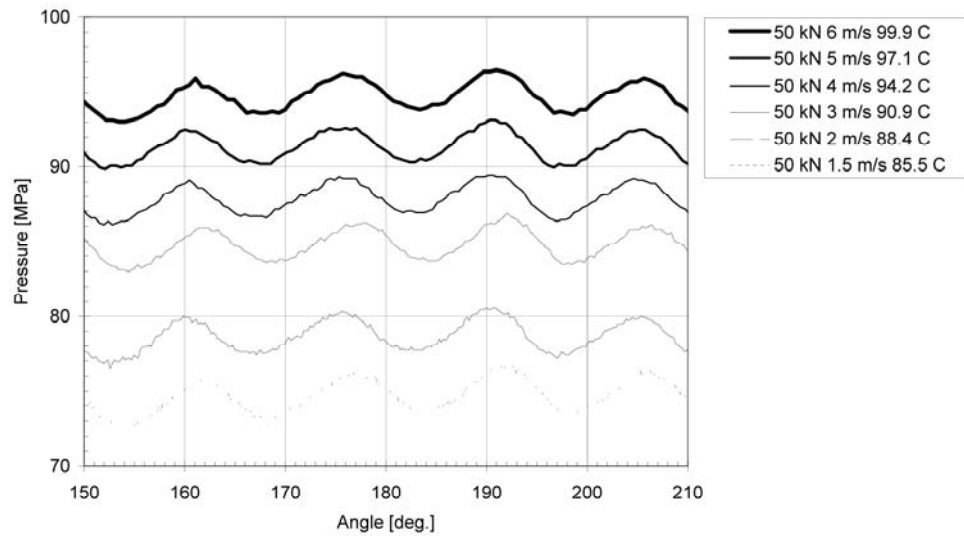


Figure 5-48. Fluctuation in the measured oil film pressure with a static load. The bearing load was 50 kN. The sliding speed was 1.5 to 6 m/s. The inlet temperature was 71 °C. The inlet pressure was 4.6 bar. The optical pressure sensor was located at measurement point 5. The sensor position angle was $27 + N \times 360$ degrees ($N = 0, 1, 2, \dots$).

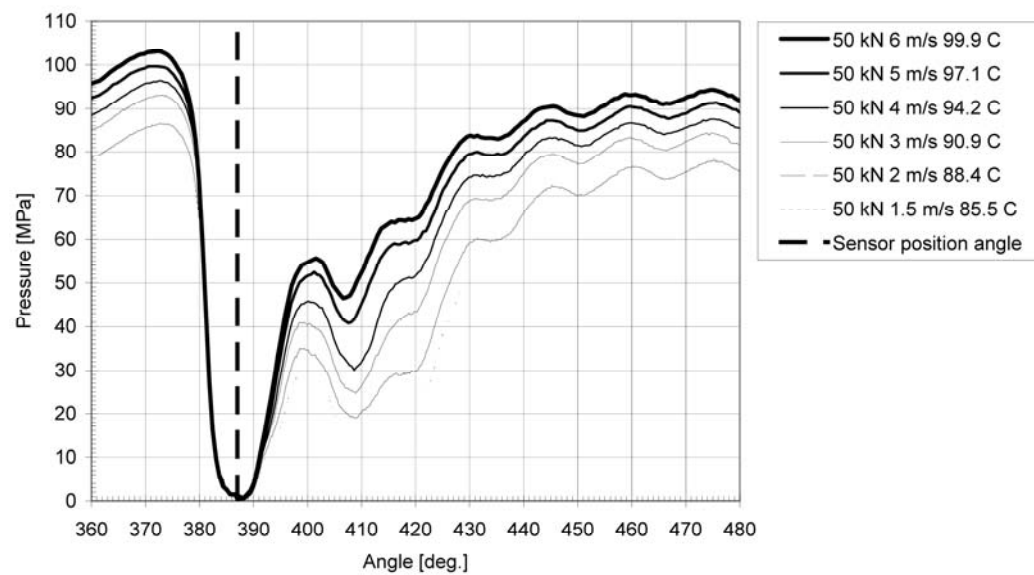


Figure 5-49. Measured oil film pressure with a static load as the radial oil-feeding hole in the shaft crossed the measurement point. The bearing load was 50 kN. The sliding speed was 1.5 to 6 m/s. The inlet temperature was 71 °C. The inlet pressure was 4.6 bar. The optical pressure sensor was located at measurement point 5. The sensor position angle was $27 + N \times 360$ degrees ($N = 0, 1, 2, \dots$).

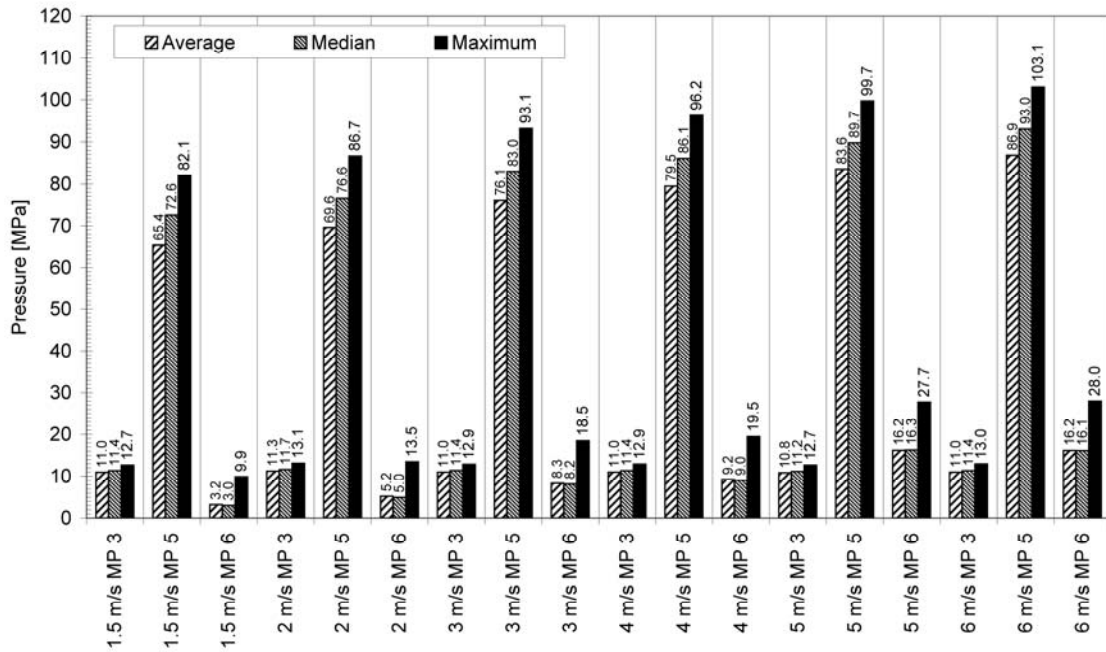


Figure 5-50. Average, median and maximum oil film pressure at three measurement points with a static load. The bearing load was 50 kN. The sliding speed was 1.5 to 6 m/s. The inlet temperature was 71 °C. The inlet pressure was 4.6 bar. The optical pressure sensors were located at measurement points (MP) 3, 5 and 6.

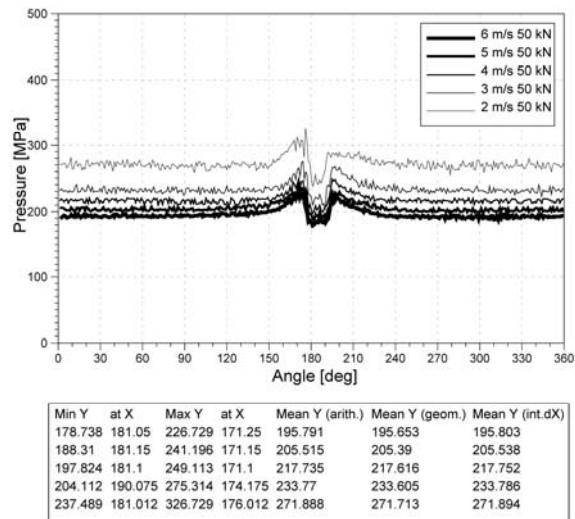


Figure 5-51. Simulated oil film pressure as a function of the angle of rotation with a static load. The bearing load was 50 kN. The sliding speed was 2, 3, 4, 5 and 6 m/s.

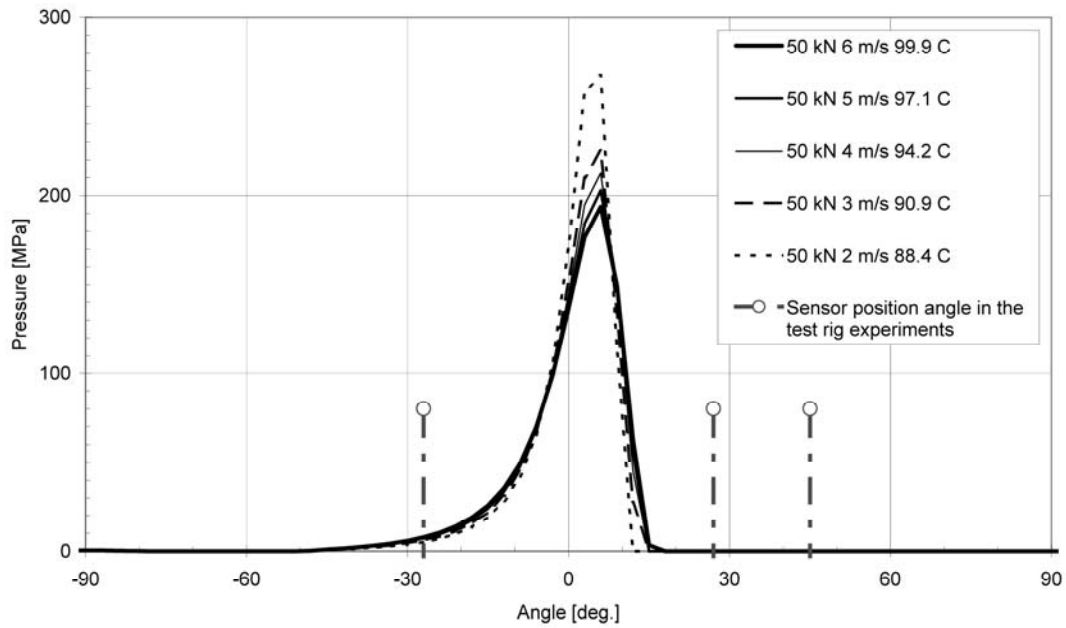


Figure 5-52. Simulated oil film pressure as a function of the position angle with a static load. The bearing load was 50 kN. The sliding speed was 2, 3, 4, 5 and 6 m/s. Note that the area of high oil film pressure does not cover all pressure-measurement points used in the test rig experiments.

6 Discussion

State of the Art

Numerous experimental and mathematical studies of the operating conditions of hydrodynamic journal bearings have been made over recent decades, but the case is far from closed. For example, the number of studies that use true-scale experiments to determine the true operating conditions of bearings in depth is limited. There is also a need for experimental studies to verify the theoretical ones.

Materials

The versatile bearing test rig used as the main test apparatus in this study was designed especially for tribological research into crankshaft bearings and lubricants of internal combustion engines. The main design of the bearing test rig was simple and spacious. The spacious main design of the bearing test rig made it possible to carry out experiments with test materials and measuring devices of different types and sizes. The frame was firm enough to resist disturbing yield and resonance phenomena within the normal operating range. This stability was an important feature for demanding experiments on bearings using sensitive measuring devices at high and dynamic loads. The hydraulic loading system was able to generate realistic static and dynamic bearing loads. The drive system generated realistic sliding speeds and the lubrication system produced realistic lubrication for the bearings of different types. The control system controlled the synchronised operation of the cylinders for various bearing load patterns. The measuring system measured and recorded the main tribological variables influencing the operation of hydrodynamic journal bearings. The optical pressure sensors for measuring the oil film pressure were novel, unique and usable devices.

The journal bearings used as test specimens in this study had the same main design and nominal dimensions as a real main bearing of a high-speed diesel engine. The shafts had a realistic nominal diameter and surface roughness. The design of the housings made it possible to use realistic pre-tensioning of oversized bearing shells and to use various

measuring devices. The lubricating oils were either real engine oils or close resemblances. The extensive use of realistic test materials enhances the general usability of the present results when they are compared with results from studies of real machines and engines.

Methods

The operation of hydrodynamic journal bearings was studied using both experimental methods and mathematical methods. Various experiments were carried out with different test materials and, as a result, the test run matrices were relatively large and complex. Mathematical studies were performed mainly for the analysis of the results from the experimental studies.

The isotherm mapping method used to determine the operating range of hydrodynamic journal bearings had several advantages. Firstly, the method was relatively simple (and therefore usable), because it was based on measurements of the operating temperature, which were easy to make with common measuring devices. Secondly, the method was illustrative and effective, because the first isotherms to be determined could (typically) be used to predict the general operation of the bearing. Thirdly, it was typically straightforward to analyse the measured data, because it was recorded (mainly) on the isotherms, where certain variables (such as the operating temperature, oil viscosity, oil density and heat flow in convection through the housing) were relatively stable. Fourthly, the method was non-destructive (when used with care), which was beneficial for practical research work with limited resources. Fifthly, the method was basically applicable to experiments using common test rigs with a continuous load control, in which the bearing load level is independent from the sliding speed level. The method also had a number of limitations or deficiencies. Firstly, the method has been tested in a limited number of cases. Secondly, the method has been tested using an apparatus with a partly manual control and automated test run procedures have not been developed. Thirdly, the applicability of the method to engine tests is limited due to continuous load control requirements, which are difficult to implement in real engines.

The experimental heat flow analysis method used to determine the friction loss of hydrodynamic journal bearings had several advantages. Firstly, the method was relatively simple (and therefore usable), because it was based on common measurements made by common measuring devices. Secondly, fairly accurate results were achieved by using a limited number of measuring devices. Thirdly, it was basically possible to use the method for different load patterns. This method also had a number of limitations or deficiencies. Firstly, the method was only usable under stable operating conditions, in which different heat flows heating and cooling the bearing were in balance. Secondly, the method was not suitable for determining momentary values of the friction loss (for example, when friction loss varies rapidly in every revolution), because the method was based on measurements at low sampling frequencies. Thirdly, thorough measurements with numerous temperature and flow measuring devices would be required to determine the friction loss exactly. In this study, the heat flow analysis was made using the minimum number of measuring devices. Therefore it was evident that there would be certain inaccuracies in the results of the analysis. Firstly, it can be assumed that the real temperature and heat flow distributions were more complex than those calculated. Secondly, some details were excluded from the analysis, such as the heat flow in convection through the shaft and the variation in oil inlet temperature and pressure, as the lubricating oil was supplied through long channels. However, the results from the heat flow analysis were mainly logical and showed an adequate level of correlation with the reference data and, therefore, it can be assumed that the experimental heat flow analysis was a fairly accurate method.

The oil film temperature was one of the key operating parameters in the experiments performed in this study. Because the thermocouples used to determine the oil film temperature were located at a small distance (3 mm) from the sliding surface of the bearing, it can be estimated that the oil film temperature was practically equal to the measured temperature (the operating temperature of the bearing). The thermocouples were mounted on the bearing in such a way that disturbing deformations, such as local bulges on the sliding surface, were avoided. The number of measurement points was set at close to the minimum. Due to the above-mentioned location and number of

measurement points, it was evident that there were certain differences between the real oil film temperature and the measured one. However, it can be assumed that these differences were tolerable for several reasons. Firstly, the temperature measurement points were located on the upper bearing sleeve, which carried the highest loads and, therefore, operated at the highest temperatures. Secondly, the expected maximum temperature differences between different points in the bearing were small. In the case of the rotating load, the maximum temperature difference was practically zero – in other words, there was an even temperature distribution. For the static load, the maximum measured temperature differences in the bearing were typically below 5 °C.

The simulations made to determine the oil film thickness were based on a well-known and accepted method; the numerical solution of the Reynolds differential equation. The calculations made to determine the oil film thickness were based on standard calculation methods. Step by step carried calculations illustrated how different variables influencing the oil film thickness (such as the bearing load, hydrodynamic angular velocity and dynamic viscosity) were linked. It was possible to make calculations without special software.

The optical pressure sensors were based on optical fibre technology, providing benefits such as insensitivity to electromagnetic disturbances and the capability to transmit information over long distances. The optical sensors were integrated in the bearing in such a way that the sliding surface of the bearing remained unchanged, which was a highly beneficial feature. The optical pressure sensors functioned well and were capable of measuring the oil film pressure in a journal bearing under realistic operating conditions. The sensor was sufficiently sensitive to detect the effects of the sliding speed and bearing load on the oil film pressure. The signal from the optical sensor had a good signal to noise ratio and its repeatability was good in the range studied. The level of fluctuation in the signal was tolerable. In the first sensor type tested, variations in the operating temperature caused some variation in the signal level. This was obviously caused by the thermal instability of the sensor design. The second sensor type had higher thermal stability than the first one.

Results - Operating range

The operating range of the bearing BA covered sliding speeds between 2 and 12 m/s and specific loads up to 32 MPa. The operating range of the bearing BE covered sliding speeds between 3 and 10 m/s and specific loads up to 21 MPa. With both bearings, the lowest calculated minimum oil film thickness was about 0.5 to 1 μm and the highest was about 8 μm . On the isotherms of the operating temperature, the specific load decreased logarithmically and the calculated minimum oil film thickness increased exponentially as the sliding speed was increased. Logically, the calculated minimum oil film thickness was at its lowest at the highest bearing loads and the lowest sliding speeds. The calculated minimum oil film thickness in bearing BA correlated fairly well with the simulated thickness. The calculated minimum oil film thickness determined by a simple method, based on the use of approximate equations, was typically between 20 and 70 % higher than the simulated minimum oil film thickness determined by the detailed method based on the numerical solution of the Reynolds differential equation. The variation of the gradients of the constant oil film thickness curves showed that the effect of the sliding speed on the oil film thickness varied. The effect was strongest at low sliding speeds and weakest at high sliding speeds. Several assumptions can be made based on these results. Firstly, at low sliding speeds, oil film thickness was the factor limiting the operating range, as the oil film thickness was close to zero at the limit of this range, regardless of the operating temperature. Secondly, the factors limiting the operating range at high sliding speeds were related to cooling capacity. The main factors influencing the cooling capacity were the oil inlet temperature, oil inlet pressure and bearing clearance. Results supporting this conclusion were presented by Fillon and Bouyer (2004) in their study involving a thermohydrodynamic analysis of a worn plain journal bearing.

The limit of the operating range was typically not an exact line at the edge of the usable operating zone, as there was a small but inevitable variation in the operating parameters disturbing the balance of operation of the bearing. The limits were inexact zones where the operating balance was limited. By increasing the load in small steps, it was possible to enhance the bearing's operating balance. The lowest usable bearing load step varied

and was linked to the level of friction loss and cooling capacity. Knowledge from the heat flow analysis can be used to analyse this relationship.

Results - Friction loss

By comparing the operating ranges used with different lubricating oils in the friction experiments and those determined by the range experiments, it can be supposed that friction loss was studied close to the limit of the bearing's operating range, at relative high operating temperatures (up to 120 °C), bearing loads (up to 36 MPa) and sliding speeds (up to 12 m/s). With all the lubricating oils tested, the specific load varied logically (and in the same way as in the range experiments) as a function of the sliding speed on the isotherms of the operating temperature. Small variations in certain operating parameters (the temperature of the housing, inlet temperature and room temperature) caused small dispersions in the recorded heat flow levels. The sliding speed of 10 m/s, which was used in the detailed study of friction loss, was close to the sliding speed of the main bearing in the real engine at its nominal output. At the sliding speed of 10 m/s, the total heat flow (friction power or friction loss) with different oils varied in the range from 0.6 to 1.1 kW which is fairly reasonable when compared with the experimental results by Berg (1996). Berg's results showed that the friction loss of a main bearing with a diameter of 54 mm in a running four-cylinder diesel engine is about 0.25 kW at a rotational speed of 4080 1/min (or sliding speed of 11.3 m/s), at a mean effective pressure of 0.5 MPa (a typical value in engines running at half load) and at operating temperature of about 140 °C. In the case studied by Berg, the proportion of heat flow transferred by the lubrication oil was about 72 %. In this study, the proportion of heat flow transferred by the lubricating oil was high when compared to the total heat flow; typically about 95 %. The proportion of heat flow through the housing was small when compared to the total heat flow; typically about 5 %. These proportions show that the cooling capacity of the bearing was based almost totally on the effectiveness of the circulating lubrication. Logically, power functions with positive gradients described the variation of the friction power as a function of the specific load and variations in the specific load had a minor effect on friction loss. Likewise, power functions with negative gradients logically described the variation of the friction coefficient as a

function of the specific load. The friction coefficients were typically below 0.01. The smallest friction coefficients were about 0.002, which is about 1 % of the typical friction coefficient between two un-lubricated metal surfaces. These relative low friction coefficient values show that the bearing was clearly operating under hydrodynamic lubrication and not under mixed or boundary lubrication. It was also logical that, in the case of oils with the highest viscosity indices (or the lowest variations in viscosity due to variations in temperature), the effect of the specific load on the relative friction coefficient was clearly different from the effect in the case of oils with the lowest viscosity indices. In the case studied, the effect of the specific load on the relative friction coefficient was strongest with the oils that had the highest viscosity indexes. The above-mentioned mentioned logical phenomena support the conclusion that the simple and rough method could be used to determine the friction loss.

Results – Oil film pressure

The operating ranges and friction losses determined for bearings of the same type as the one used in the pressure experiment set showed that the oil film pressure was measured under hydrodynamic lubrication and realistic operation conditions.

Determining the oil film pressure distribution in a circumferential direction with a rotating load was a straightforward task, as the pressure wave (area of high pressure in the oil film) crossed the measurement point once per revolution. There was a “moving pressure wave” that was simply “scanned” at the measurement point, once per revolution, by a single optical pressure sensor. The effect of the oil groove on the oil film pressure distribution was probably small, as the pressure-measurement point was located on the plain bearing sleeve, far from the oil groove.

Determining the oil film pressure distribution in a circumferential direction with a static load was a more difficult task, because the pressure wave did not cross the measurement points frequently. There was a “stationary pressure wave” with a non-fixed position, moving slightly clockwise or anticlockwise along the sliding surface of the bearing due to variations in the bearing load, sliding speed or operating temperature. It was difficult

to see how wide the pressure wave was by tracing signals from a limited number of measurement points in different angular positions and where its peak (point of maximum pressure) was. Because of these difficulties, a detailed analysis of oil film pressure distribution with a static load was excluded from the study. When the radial oil-feeding hole in the shaft crossed the measurement points once per revolution, the measured oil film pressure decreased rapidly to zero. This phenomenon was useful for determining momentary signal levels from the optical pressure sensors at zero oil film pressure. In addition, the phenomenon was useful for phasing the signals. Basically, it would also have been possible to determine the oil film pressure distribution in the axial direction, as the bearing and housing were modified for oil film pressure measurements in this direction.

With a rotating load, both the measured and simulated oil film pressures increased as the bearing load was increased. Both the measured and simulated oil film pressures decreased (typically) as the sliding speed was increased. The resultants, which were calculated as products of the surface area and the oil film pressure, were almost equal to the bearing load, as the direction of the local forces (or nodal forces) were taken into account. This equality showed that the magnitudes of the measured and simulated oil film pressure were typically at a realistic level. However, there were certain basic differences in the distribution of the measured and simulated oil film pressures. Firstly, the measured oil film pressure wave (area of high pressure in the oil film) was clearly wider than the simulated one. Secondly, the measured peak oil film pressure was clearly lower than the simulated pressure.

With a static load, both the measured and simulated oil film pressures increased as the bearing load was increased. Both the measured and simulated oil film pressures decreased as the sliding speed was increased. High oil film pressures were recorded at all three measurement points, which showed that the oil film pressure wave was wide. The measured oil film pressure wave was clearly wider than the simulated one.

Based on this limited data, it is difficult to define the main factor that causes the differences between measured and simulated oil film distributions. It is possible that the oil flow on the real sliding surface was more complex than the flow on the simulated sliding surface and that the complexity of the oil flow prevented an ideal, sharp “pressure wave” in the oil film. It is also possible that the deformation of the real sliding surface was clearly different from the deformation of the simulated sliding surface and that the difference between the deformations caused significant differences in the dimensions of the real and simulated lubrication gaps.

In this study, the highest measured oil film pressures in the bearing were clearly above 100 MPa, which is a fairly high value when compared with reported experimental results from other studies with real engine bearings. Mihara *et al.* (1995) measured oil film pressures up to about 33 MPa in the 62 mm diameter main bearing of a two-cylinder diesel engine with a displacement of 1885 cm³, running at full load and at a rotational speed of 1400 1/min (or sliding speed of 4.5 m/s). Mihara *et al.* (1996) measured oil film pressures up to about 7 to 9 MPa in the 52 mm diameter main bearing of a four-cylinder petrol engine with a displacement of 1588 cm³, running at half load and at a rotational speed of 3000 1/min (or sliding speed of 8.2 m/s). Someya and Mihara (2004) measured oil film pressures up to about 50 MPa in the 81 mm diameter main bearing of a four-cylinder diesel engine with a displacement of 5307 cm³, running at full load and at a rotational speed of 1500 1/min (or sliding speed of 6.4 m/s). In addition, they measured oil film pressures in the crank pin bearing of the above-mentioned engine, recording oil film pressures up to about 170 MPa.

Reliability of the results

The reliability of the results from this study was enhanced by several facts. Firstly, the test rig experiments were made in true scale and realistic test materials were extensively used. Secondly, the experimental methods were mainly conventional and usable. For example, the operating temperature mapping and the heat flow analysis were based on common temperature measurements by thermocouples. For the pressure measurements, it was possible to calibrate the optical sensors, as the bearing was basically ready for

instant use; installed and pre-tensioned in the housing. Thirdly, the cases studied were simple and, therefore, easy to perform and analyse. Fourthly, the bearing simulation method was based on the solution of the well-known and widely accepted Reynolds equation. Fifthly, the bearing simulations were carried out using advanced simulation software. The reliability of the results may have been reduced by the following facts, considered as possible sources of error. Firstly, the bearing test rig was a robust apparatus and the test material was examined through the use of simple methods. Therefore some defects may have been present (such as unstable operating parameters, incomplete geometry or misalignment), disturbing the experimental results. Secondly, there were certain shortcomings in the experimental methods. For example, the number of the temperature measurement points was limited close to the minimum and in some cases the locations of the temperature measurement points were not optimal. Thirdly, the sample sizes were typically small when compared to the size and complexity of the test run matrices. Fourthly, the analysis of the equations used in the simulations was limited. Fifthly, the analysis of the features of the simulation software was limited.

Novelty of the results

The novelty of the results related to the operating range and friction loss as such is low, because these subjects, particularly friction loss, have been discussed in numerous studies. However, the isotherm mapping used in the range experiment set can be considered as a fairly unique research method.

The novelty of the results related to the oil film pressure in real type hydrodynamic journal bearings under realistic operating conditions can be considered to be fairly notable, as the experimental determination of the oil film pressure in the bearings has typically been a demanding or even unfeasible task. However, it should be pointed out that the basics of the optical pressure sensor and preliminary results from oil film pressure measurements using this type of sensor were presented by a research team (Ronkainen *et al.*, 2008), of which the Author was a member. In this study, the results from the earlier studies were examined in detail and, for the first time, the relationship

between oil film pressure and other key parameters influencing the operation of hydrodynamic journal bearings was investigated.

Validity and universality of the results

The extent of the validity and the universality of the results from the experiments performed to determine the operating range and friction loss as such is limited, as they are related to a single type of hydrodynamic journal bearing, operating under certain given conditions. However, these results were necessary to determine the hydrodynamic operating range of the bearing used in experiments related to oil film pressure. These results were also usable for studying the relationship between oil film pressure and other key parameters.

The results related to the oil film pressure in hydrodynamic journal bearings are valid and universal to a notable extent for several reasons. Firstly, there have been a limited number of studies to experimentally determine the oil film pressure of hydrodynamic journal bearings under realistic operating conditions. In this study, oil film pressure was determined and its relationship to other key operating parameters was investigated, under realistic operating conditions. Secondly, there have been a limited number of studies to compare experimentally determined oil film pressures with those determined theoretically. This study compared the measured oil film pressure data to the simulated data. The results from the experimental studies of oil film pressure can be used to validate mathematical methods. The validity and the universality of the results are enhanced by the notable relationship between oil film pressure and other key bearing operation parameters. In particular, there is a clear link between oil film pressure and the minimum oil film thickness; typically, as the pressure increases, the thickness decreases, and *vice versa*. Therefore, by determining the oil film pressure, it is possible to obtain estimates of the oil film thickness. By determining the pressure in the lubricating oil film, it is possible to increase our knowledge of the true operating conditions of hydrodynamic journal bearings. This knowledge can be used in the development of safer and more efficient machines and engines with hydrodynamic journal bearings that carry high and dynamic loads.

7 Conclusions and recommendations

Main results

The main result of this study was the measurement of realistic oil film pressure in real type hydrodynamic journal bearings at various operating points across the realistic operating range and that certain significant differences between the measured and simulated data were found. The measured oil film pressure wave was clearly wider than the simulated one and the measured peak oil film pressures were clearly lower than those simulated.

Contribution of the study

The oil film pressure in hydrodynamic journal bearings was determined under realistic operating conditions by using a unique test apparatus and newly-developed measuring devices. The results from this study can be used as a reference in the development of research methods in journal bearing tribology, especially in the development of measuring and simulation methods related to the contact of the journal bearing, lubricating oil film and shaft.

New information on the operation of hydrodynamic journal bearings

The results showed that the experimentally determined oil film pressure in hydrodynamic journal bearings was distributed differently from the pressure estimated by mathematical methods. This difference in the oil film pressure distribution is significant, especially under extreme operating conditions close to the limit of the operating range of the bearing.

Recommendations

From the point of view of tribological bearing research, further development of the optical pressure sensor is highly recommended, because the sensors developed and tested so far have been unique prototypes with certain individual characteristics; they are not generally available research tools with guaranteed specifications. As part of further development, it would be worthwhile to integrate the optical pressure sensor in

the bearing as a completely fixed part and to add more functions (such as measuring the operating temperature) to the sensor head. In addition, it would be worthwhile to test the usability of the optical sensor in new applications, where its best characteristics (such as high durability and insensitivity to electromagnetic disturbances) can be utilised.

Preliminary results from the bearing experiments with the optical pressure sensor have been so promising that it would be most interesting to see the full potential of the sensor. Therefore it is recommended to continue the experimental bearing research with the optical pressure sensors. Concerning the test rig experiments, it would be straightforward (and definitely most useful) to carry out an experiment in which the oil film temperature, oil film thickness, oil film pressure and friction loss are determined simultaneously under various operating conditions. To determine the oil film distribution both in the circumferential and axial directions in the bearing, it is recommendable to utilise existing possibilities to obtain multipoint pressure measurements. A single experiment of this kind would return plenty of useful and illustrative data for tribological research into hydrodynamic journal bearings.

8 Summary

The power density in different machines, such as internal combustion engines, is increasing year by year because of increasing demands for mechanical and economic efficiency. In machine design, one of the consequences of the increase in power density is that critical power transmission components have to carry increasingly high loads. Hydrodynamic journal bearings are typical critical power transmission components, which carry high loads in various machines. In machine design, therefore, it is essential to know the true or expected operating conditions of the hydrodynamic journal bearings. The operating conditions can be described by a set of tribological variables, called key operating parameters. The key operating parameters most directly related to the bearing-lubricant-shaft contact are the oil film temperature, oil film thickness and oil film pressure. They can be determined by different experimental or mathematical means with varying levels of complexity.

Until now, oil film pressure in hydrodynamic journal bearings has been studied mainly by mathematical means, because the experimental determination of oil film pressure has been a demanding or even an unfeasible task. Under real operating conditions, there are generally many practical matters that complicate the experimental determination of the true oil film pressure in a certain point or at a certain moment. For example, the oil film may be extremely thin and therefore sensitive to different disturbing factors such as defects in geometry.

The main aim of the study was to determine the oil film pressure in hydrodynamic journal bearings under realistic loads. Therefore, the study was focused on the main bearings in the crank train of a high-speed diesel engine. In addition, the relationship between oil film pressure and other key operating parameters of journal bearings was studied. Therefore the study also included the determination of the operating range, friction loss, oil film temperature and oil film thickness.

The operation of hydrodynamic journal bearings was studied both by experimental means in true scale and by mathematical means in simulations and calculations. In the experimental study, the main test apparatus was a versatile bearing test rig designed especially for tribological research into crankshaft bearings of internal combustion engines. The test rig was developed by a research team. The Author was in charge of the main design, construction and operation of the test rig. The test rig had a hydraulic loading system to generate realistic bearing loads. The drive system of the test rig was able to generate realistic sliding speeds and the lubrication system was able to produce realistic lubrication for bearings of different types. The control system controlled the synchronised operation of the cylinders of the loading system. The measuring system measured and recorded the main tribological variables that influence the operation of hydrodynamic journal bearings.

Four different bearings, three different shafts, two different housings and seven different lubricating oil types were used in the test rig experiments. All bearings had the same main design. The nominal outer diameter, inner diameter, width and wall thickness of the bearings were 91 mm, 85 mm, 32 mm and 3 mm, respectively. Two of the bearings were plain and two had an oil groove in their lower shells. All shafts were made of steel and their nominal diameter and length were 85 mm and 600 mm, respectively. One of the shafts had no oil-feeding holes and the two other shafts had one radial oil-feeding hole with a diameter of 6 mm. A rotating union was used to supply oil through the shafts. Both housings had the same main design. The nominal outer diameter, inner diameter and width of the housings were 270 mm, 91 mm and 80 mm, respectively. The housings consisted of two half-round, thick-wall sleeves. The lower sleeve had lubrication channels. The upper sleeve had holes for different measuring devices. The design of the housings made it possible to use realistic pre-tensioning caused by oversized bearing shells. One of the lubricating oils was a typical SAE 40 mono-grade engine lubricant with a low viscosity index and one was a combined cylinder and crankcase lubricant blended as SAE 40 and used in medium speed marine diesel engines. The other oils were special oils with high viscosity indices and different additives.

To determine the operating range of hydrodynamic journal bearings, an experimental method called isotherm mapping was developed. The method was based on the predictable operation of journal bearings on isotherms of the operating temperature. In isotherm mapping, both the isotherms of the operating temperature and the limits of the operating range of the journal bearing were determined as functions of the sliding speed and specific load. The friction loss of the bearing was analysed by performing an experimental heat flow analysis with limited measurements and simple calculations. The oil film temperature was estimated to be equal to the operating temperature of the bearing. The operating temperature was measured by thermocouples, the measurement points of which were on the outer surface of the upper bearing shell, on the circumferential centreline. The minimum oil film thickness was either simulated by the simulation software or calculated. Optical pressure sensors were used for the experimental determination of the oil film pressure. The optical pressure sensors were developed by a research team, of which the Author was a member. The optical pressure sensors were based on optical fibre technology, which provides benefits such as insensitivity to electromagnetic disturbances and the capability to transmit information over long distances. The optical sensors were integrated in the bearing in such a way that the sliding surface of the bearing remained unchanged and acted as a measurement membrane.

The experimental studies were split up into three main sets of experiments, which were known as the range, friction and pressure experiment sets. In the range experiment set, the operating ranges of hydrodynamic journal bearings were studied by the isotherm mapping method and the aim of the study was to determine the operating range and its main influencing factors. Two different bearing types and two different bearing clearances were used. In the friction experiment set, the friction loss influencing the width of the operating range of the hydrodynamic bearing was studied using the heat flow analysis method. Six different oil types with different densities and viscosities were used. In the pressure experiment set, the oil film pressure influencing the operation of hydrodynamic journal bearings was studied using the optical pressure measurement

method. Between one and three optical pressure sensors were used to measure the oil film pressure. The pressure measurements were carried out at various different bearing load and sliding speed levels and at two different bearing load patterns, all within the bearing's realistic operating range.

The mathematical studies, consisting of simulations by advanced simulation software and calculations by common calculation methods, were performed mainly to analyse the results from the experimental studies. The simulations were focused on the main task of studying oil film pressure in hydrodynamic bearings. The bearing simulation method was based on the numerical solution of the Reynolds differential equation. The bearing simulations were made by the AVL EXCITE simulation software using the finite element method and finite element analysis to simulate the dynamic response of engine parts connected by a set of nonlinear joints. The simulations were executed by the Author. The simulation model consisted of an elastohydrodynamic bearing, a short shaft and an anchored housing. The model of the bearing had 19 nodes in the axial direction and 121 nodes in the circumferential direction. The shaft had five mass points. Both nominal and measured dimensions were used as the input data to determine the geometry of the components. Both nominal and measured parameters were used as input data to determine the operating conditions of the bearing. The increase in oil temperature due to friction was ignored. The lubricating oil temperature was assumed to be constant and equal to the measured operating temperature of the bearing.

The results showed that, with a sufficient bearing clearance and oil supply, the operating range of the bearing type that was tested covered realistic sliding speeds of between 2 and 12 m/s and realistic specific loads up to 32 MPa. As the sliding speed was increased along the isotherms of the operating temperature, the specific load decreased logarithmically and the calculated minimum oil film thickness increased exponentially. The calculated minimum oil film thickness varied between 0.5 and 8 μm . The effect of the sliding speed on the calculated oil film thickness was strongest at low sliding speeds and weakest at high sliding speeds. Based on these results, it was assumed that, at low sliding speeds, the oil film thickness was the factor limiting the operating range and at

high sliding speeds, the factors limiting the operating range were related to the cooling capacity.

The friction loss was studied close to the limit of the operating range of the bearing; at relatively high operating temperatures (up to 120 °C), bearing loads (up to 36 MPa) and sliding speeds (up to 12 m/s). With all lubricating oils tested, the specific load varied logically as a function of the sliding speed on the isotherms of the operating temperature. The sliding speed of 10 m/s, which was used in the detailed study of friction loss, was close to the sliding speed of the main bearings in a real engine at nominal output. At the sliding speed of 10 m/s, the total heat flow or friction power (friction loss) with different oils varied in the range from 0.6 to 1.1 kW. The cooling capacity of the bearing was based almost entirely on the effectiveness of the circulating lubrication. The friction coefficients were typically below 0.01 and the lowest values were about 0.002. Logical differences were found in the level of friction loss between oils with different viscosity indices.

The operating ranges and friction losses determined for bearings of the same type as the one used in the pressure experiment set showed that the oil film pressure was measured under hydrodynamic lubrication and realistic operation conditions. With a rotating load, both the measured and simulated oil film pressure increased as the bearing load was increased. Both the measured and simulated oil film pressure generally decreased as the sliding speed was increased. With a static load, both the measured and simulated oil film pressure increased as the bearing load was increased. Both the measured and simulated oil film pressure decreased as the sliding speed was increased. The magnitudes of the measured and simulated oil film pressures were generally realistic, but there were certain basic differences in the measured and simulated oil film pressure distributions. Firstly, the measured oil film pressure wave (area of high pressure in the oil film) was clearly wider than the simulated wave. Secondly, the measured peak oil film pressures were clearly lower than those simulated.

The reliability of the results from this study was enhanced by the use of true-scale experiments, realistic test materials, simple cases and mainly conventional research methods. The reliability of the results may have been reduced by the use of a robust test apparatus, limited measuring arrangements and complex test run matrices.

The results from the experiments performed to determine the operating range and friction loss are related to a single type of hydrodynamic journal bearing operating under certain given operating conditions. As such, these results are only valid and universal to a limited extent. However, the results were necessary to determine the hydrodynamic operating range of the bearing used in the experiments related to oil film pressure. Those results were also usable for studies of the relationship between the oil film pressure and other key parameters.

The results related to the oil film pressure in hydrodynamic journal bearings are valid and universal to a notable extent for several reasons. Firstly, there have been a limited number of studies to experimentally determine the oil film pressure in hydrodynamic journal bearings under realistic operating conditions. In this study, oil film pressure was determined and its relationship to other key operating parameters was investigated under realistic operating conditions. Secondly, there have been a limited number of studies to compare experimentally determined oil film pressures with those determined theoretically. This study compared the measured oil film pressure data to the simulated data. The results from the experimental studies of oil film pressure can be used to validate mathematical models. The validity and the universality of the results are enhanced by the notable relationship between oil film pressure and other key bearing operation parameters. By determining the pressure in the oil film, it is possible to increase our knowledge of the true operating conditions of hydrodynamic journal bearings. This knowledge can be used in the development of safer and more efficient machines and engines with hydrodynamic journal bearings that carry high and dynamic loads.

References

Affenzeller, J., and Gläser, H. 1996. Lagerung und Schmierung von Verbrennungsmotoren. Springer. 397 p. ISBN 978-3-211-82577-8.

Ahn, H.-J. 2006. A cylindrical capacitive sensor (CCS) for both radial and axial motion measurements. *Measuring Science Technology*. Vol. 17(2006), pp. 2027-2034.

Andersson, P., Juhanko, J. Nikkilä, A.-P., and Lintula, P. 1996. Influence of topography on the running-in of water-lubricated silicon carbide journal bearings. *Wear*. Vol. 201(1996), pp. 1-9.

Andersson, P., and Lintula, P. 1994. Load-carrying capability of water-lubricated ceramic journal bearings. *Tribology International*. Vol. 27(1994):5, pp. 315-321.

Aoyama, T., Kawamoto, A., Noda, T., Ozasa, T., Kato, T., Murai, Y., and Ito, T. 2003. Analysis of noise occurrence by cavitation in the main bearing of diesel engine. *JSAE Review*. Vol. 24(2003), pp. 59-64.

Bates, T. W., Fantino, B., Launay, L., and Frêne, J. 1990. Oil Film Thickness in an Elastic Connecting-Rod Bearing: Comparison Between Theory and Experiment. *Tribology Transactions*. Vol. 33(1990):2, pp. 254-266.

Becker, E. 2004. Trends in tribological materials and engine technology. *Tribology International*. Vol. 37(2004), pp. 569-575.

Berg, M. 1996. Untersuchungen zum Schmierstoffdurchsatz und zur Reibungsleistung dynamisch belasteter Radialgleitlager. Dissertation. Fachbereich Maschinenbau und Verfahrenstechnik der Universität Kaiserslautern. Kaiserslautern, Germany. 147 p.

Brito, F., Miranda, A., Bouyer, J., and Fillon, M. 2006. Experimental Investigation of the influence of Supply Temperature and Supply Pressure on the Performance of a Two Axial Groove Hydrodynamic Journal Bearing. In: *Proceedings of the IJTC2006: STLE / ASME International Joint Tribology Conference*. San Antonio, Texas, USA. October 23-25, 2006. IJTC06-12042. 9 p.

- Bukovnik, S., Dörr, N., Čaika, V., Bartz, W. J., and Loibnegger, B.** 2006. Analysis of diverse simulation models for combustion engine journal bearings and the influence of oil condition. *Tribology International*. Vol. 39(2006), pp. 820-826.
- Coy, R. C.** 1998. Practical applications of lubrication models in engines. *Tribology International*. Vol. 31(1998):10, pp. 563-571.
- Del Din, M., and Kassfeldt, E.** 1999. Wear characteristics with mixed lubrication conditions in a full scale journal bearing. *Wear*. Vol. 232(1999), pp. 192-198.
- Dowell, J.** 2005. Thermal cracks in diesel engine crankshafts. Dissertation. Case Western Reserve University, Department of Mechanical and Aerospace Engineering. Cleveland, Ohio. 167 p.
- Durak, E., Kurbanoglu, C., Bıyıkioğlu, A., and Kaleli, H.** 2003. Measurement of friction force and effects of oil fortifier in engine journal bearings under dynamic loading conditions. 2003. *Tribology International*. Vol. 36(2003), pp. 599-607.
- Dzida, M., and Prusakiewicz, P.** 2008. The effect of temperature and pressure on the physicochemical properties of petroleum diesel oil and biodiesel fuel. *Fuel*. Vol. 87(2008), pp. 1941-1948.
- Effenberger, H.** 2000. *Dampferzeugung*. Springer. 854 p. ISBN 978-3-540-64175-9.
- Ene, N., Dimofte, F., Keith Jr., T. G.** 2008. A stability analysis for a hydrodynamic three-wave journal bearing. 2008. *Tribology International*. Vol. 41(2008), pp. 434-442.
- Fillon, M., and Bouyer, J.** 2004. Thermohydrodynamic analysis of a worn plain journal bearing. *Tribology International*. Vol. 37(2004), pp. 129-136.
- Gleghorn, P., and Bonassar, L.** 2008. Lubrication mode analysis of articular cartilage using Stribeck surfaces. *Journal of Biomechanics*. Vol. 41(2008), pp. 1910-1918.
- Heywood, J. B.** 1988. *Internal Combustion Engine Fundamentals*. McGraw-Hill, Inc. 930 p. ISBN 0-07-028637-X.

Ichikawa, S., Mihara, Y., and Someya, T. 1995. Study on main bearing load and deformation of multi-cylinder internal combustion engine: Relative inclination between main shaft and bearing. *JSAE Review*. Vol. 16(1995), pp. 383-386.

Irani, K., Pekkari, M., and Ångström, H.-E. 1997. Oil film thickness measurement in the middle main bearing of a six-cylinder supercharged 9 litre diesel engine using capacitive transducers. *Wear*. Vol. 207(1997), pp. 29-33.

Jiang, G.D., Hu, H., Xu, W., Jin, Z.W., and Xie, Y.B. 1997. Identification of oil film coefficients of large journal bearings on a full scale journal bearing test rig. *Tribology International*. Vol. 30(1997):11, pp. 789-793.

de Kraker, A., van Ostayen, R., and Rixen, D. 2007. Calculation of Stribeck curves for (water) lubricated journal bearings. *Tribology International*. Vol. 40(2007), pp. 459-469.

Leclère, Q., Pezerat, C., Laulagnet, B., and Polac, L. 2005. Indirect measurement of main bearing loads in an operating diesel engine. *Journal of Sound and Vibration*. Vol. 286(2005), pp. 341-361.

Marx, S., and Junghans, R. 1996. Friction and wear of highly stressed thermoplastic bearings under dry sliding conditions. *Wear*. Vol. 193(1996), pp. 253-260.

Masuda, T., Ushijima, K., and Hamai, K. 1992. A Measurement of Oil Film Pressure Distribution in Connecting Rod Bearing With Test Rig. *Tribology Transactions*. Vol. 35(1992):1, pp. 71-76.

Meruane, V., and Pascual, R. 2008. Identification of nonlinear dynamic coefficients in plain journal bearings. *Tribology International*. Vol. 41(2008), pp. 743-754.

Mihara, Y., and Someya, T. 2002. Measurement of Oil-Film Pressure in Engine Bearings Using a Thin-Film Sensor. *Tribology Transactions*. Vol. 45(2002):1, pp. 11-20.

Mihara, Y., Kajiwara, M., Fukamatsu, T., and Someya, T. 1996. Study on the measurement of oil-film pressure of engine main bearing by thin-film sensor – The influence of bearing deformation on pressure sensor output under engine operation. *JSAE Review*. Vol. 17(1996), pp. 281-286.

Mihara, Y., Hayashi, T., Nakamura, M., and Someya, T. 1995. Development of measuring method for oil film pressure of engine main bearing by thin film sensor. 1995. *JSAE Review*. Vol. 16(1995), pp. 125-130.

Moreau, H., Maspeyrot, P., and Frene, J. 2002. Mesure des épaisseurs de film d'huile dans les paliers de moteur automobile. *Mécanique & Industries*. Vol. 3(2002), pp. 607-617.

Moreno Nicolás, J.A., Gómez de León Hijes, F.C., and Alhama, F. 2007. Solution of temperature fields in hydrodynamics bearings by the numerical network method. *Tribology International*. Vol. 40(2007), pp. 139-145.

Mosleh, M., Saka, N., and Suh, N. 2002. A mechanism of high friction in dry sliding bearings. *Wear*. Vol. 252(2002), pp. 1-8.

Nursoy, M., Öner, C., and Can, İ. 2008. Wear behaviour of a crankshaft journal bearing manufactured by powder spraying. *Materials and Design*. Vol. 29(2008), pp. 2047-2051.

Okamoto, Y., Kitahara, K., Ushijima, K., Aoyama, S., Xu, H., and Jones, G. 2000. A study for wear and fatigue on engine bearings by using EHL analysis. *JSAE Review*. Vol. 21(2000), pp. 189-196.

Ozsarac, U., Findik, F., and Durman, M. 2007. The wear behaviour investigation of sliding bearings with a designed testing machine. *Materials and Design*. Vol. 28(2007), pp. 345-350.

Priebsch, H. H., and Krasser, J. 1996. Simulation of the oil film behaviour in elastic engine bearings considering pressure and temperature dependent oil viscosity. In: Dowson, D., Childs, T.H.C., and Taylor, C. (eds.) Proceedings of the 23rd Leeds-Lyon Symposium on Tribology-Elastohydrodynamics. Leeds, UK. September 10-13, 1996. pp. 651-659.

Ronkainen, H., Hokkanen, A., Kapulainen, M., Lehto, A., Martikainen, J., Stuns, I., Valkonen, A., Varjus, S., and Virtanen, J. 2008. Optical sensor for oil film pressure measurement in journal bearings. *NORDTRIB 2008*. Tampere, Finland. June 10-13, 2008. 12 p. NT2008-79-12.

Savaşkan, T., Pürçek, G., and Murphy, S. 2002. Sliding wear of cast zinc-based alloy bearings under static and dynamic loading conditions. *Wear*. Vol. 252(2002), pp. 693-703.

Sinanoğlu, C., Nair, F., Karamış, M.B. 2005. Effects of shaft surface texture on journal bearing pressure distribution. *Journal of Materials Processing Technology*. Vol. 168(2005), pp. 344-353.

Someya, T., and Mihara, Y. 2004. New thin-film sensors for engine bearings. In: Proceedings of the CIMAC Congress 2004, Kyoto. Paper No. 91. 16 p.

Sun, J., and Changlin, G. 2004. Hydrodynamic lubrication analysis of journal bearing considering misalignment caused by shaft deformation. *Tribology International*. Vol. 37(2004), pp. 841-848.

Syverud, T. 2001. Experimental investigation of the temperature fade in the cavitation zone of full journal bearings. *Tribology International*. Vol. 34(2001), pp. 859-870.

Syverud, T., and Tanaka, M. 1997. Experimental investigation of the effect of shaft heating and cooling on single bore journal bearing. *Wear*. Vol. 207(1997), pp. 112-117.

Tanaka, M. 2000. Journal bearing performance under starved lubrication. *Tribology International*. Vol. 33(2000), pp. 259-264.

Tomimoto, M. 2003. Experimental verification of a particle induced friction model in journal bearings. *Wear*. Vol. 254(2003), pp. 749-762.

Turaga, R., Sekhar, A., and Majumdar, B. 1999. The effect of roughness parameter on the performance of hydrodynamic journal bearings with rough surfaces. *Tribology International*. Vol. 32(1999), pp. 231-236.

Ünlü, B., Atik, E., and Meriç, C. 2007. Effect of loading capacity (pressure-velocity) to tribological properties of CuSn10 bearings. *Materials and Design*. Vol. 28(2007), pp. 2160-2165.

Ünlü, B., and Atik, E. 2007. Determination of friction coefficient in journal bearings. *Materials and Design*. Vol. 28(2007), pp. 973-977.

Wang, Q. 1997. Seizure failure of journal-bearing conformal contacts. *Wear*. Vol. 210(1997), pp. 8-16.

Yang, Z., Wang, S., Wang, Q., and Xie, Y. 2007. Three-dimensional bearing load sensor design and numerical investigations. *Sensors and Actuators. A* 136(2007), pp. 304-312.

Zhou, H., Zhao, S., Xu, H., and Zhu, J. 2004. An experimental study on oil-film dynamic coefficients. *Tribology International*. Vol. 37(2004), pp. 245-253.

Appendix A Strength of the frame

The strength of the frame of the bearing test rig was studied mathematically, by the finite element method (FEM), by Lappeenranta University of Technology. The study was carried out as a part of a rotor vibration research project, in which the test rig was used as an active rotor vibration damper. Results of the study are presented in brief below.

The expected maximum stress in the frame was 90 MPa at 120 % load (see Figure 1). The point of maximum stress was in the junction between the uppermost cylinder housing and the beam (see Figure 2). The lowest natural oscillation frequency of the frame was 91 Hz (see Figure 3).

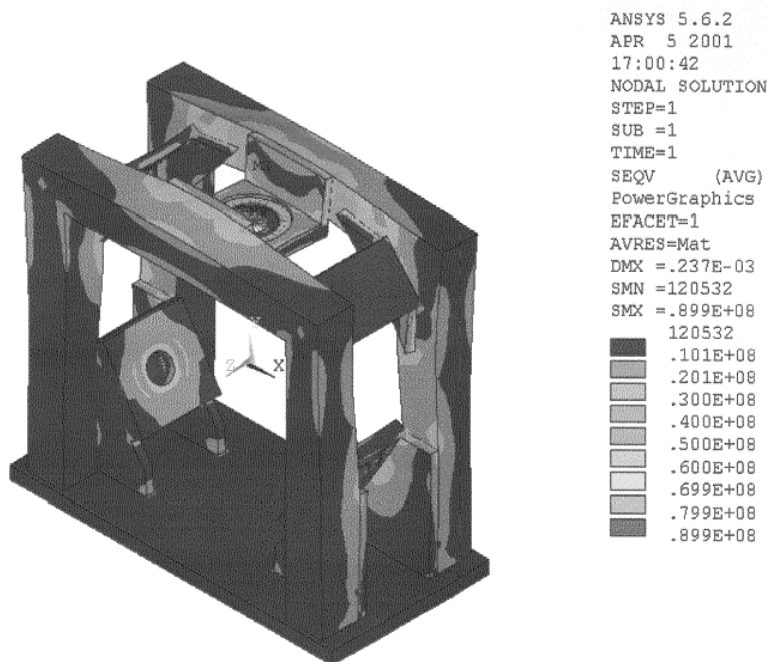


Figure 1. Stress in the frame at 120 % load. The pushing force of the cylinders was 120 kN. The notation “SMX=.899E+08” in the legend shows that the maximum stress was 90 MPa. (Lappeenranta University of Technology)

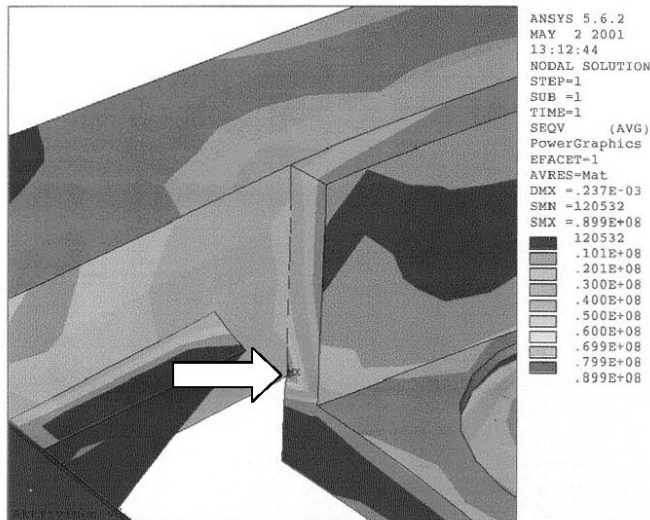


Figure 2. Stress in the junction between the uppermost cylinder housing and the beam at 120 % load. The pushing force of the cylinders was 120 kN. The point of the maximum stress (90 MPa) is indicated by an arrow. (Lappeenranta University of Technology)

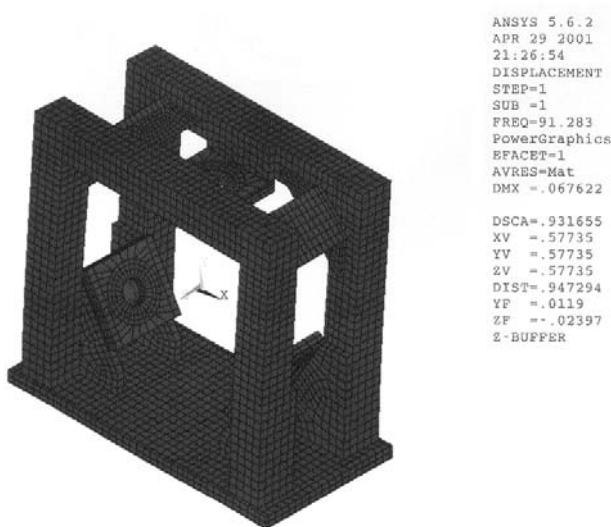


Figure 3. Vibrations in the frame of the test rig. The notation “FREQ=91.283” in the legend shows that the lowest natural oscillation frequency in the frame was 91 Hz. (Lappeenranta University of Technology)

Appendix B Trial run

The commissioning tests and the trial run of the loading system of the bearing test rig were carried out by the supplier of the hydraulics, Helsinki University of Technology, and VTT Technical Research Centre of Finland. Results from the trial run are presented below.

The trial run consisted of various tests. In test no. 1, a pressure test of the load cylinders was carried out. The control settings of the loading system were checked as part of the pressure testing. During the test, a load cell was installed between the piston head of cylinder no. 2 and the frame of the test rig, and the cylinder load was varied. The load range studied was from zero to the nominal load (100 kN). In addition, the bending of the upper beam of the frame was measured by a dial gauge. The maximum bend in the middle of the upper beam was about 20 μm at the nominal load.

In test no. 2, the set load, the load measured by the load cell, and load calculated from the hydraulic pressure data were compared at a load pattern resembling a sine wave load. It was found that the correlation between the set, measured, and calculated loads was high at the frequency levels studied, 1 Hz (see Figure 1) and 10 Hz (see Figure 2). There were inevitable phase differences between the set, measured and calculated loads, but the levels of these differences were fairly low.

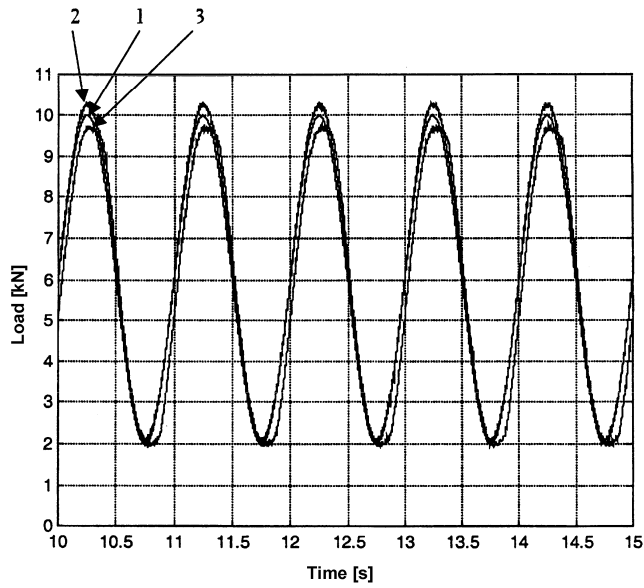


Figure 1. Set load (1), measured load (2), and calculated load (3) of cylinder no. 2 in the trial run of the loading system. The set frequency and set load were 1 Hz and 6 ± 4 kN, respectively. (VTT Technical Research Centre of Finland)

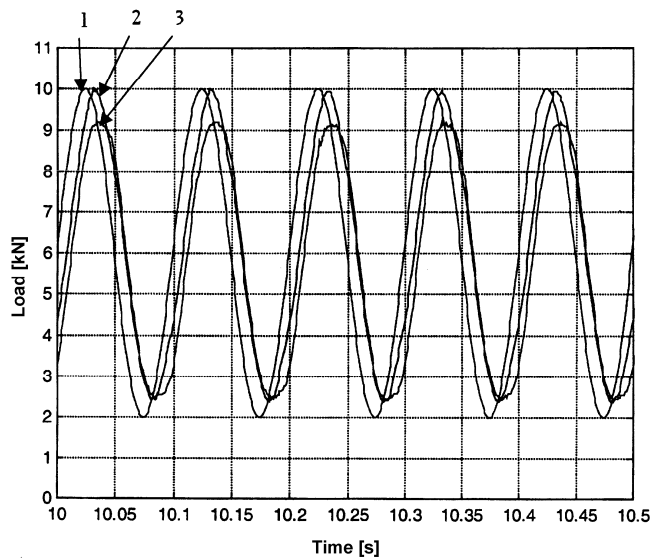


Figure 2. Set load (1), measured load (2), and calculated load (3) of cylinder no. 2 in the trial run of the loading system. The set frequency and set load were 10 Hz and 6 ± 4 kN, respectively. (VTT Technical Research Centre of Finland)

In test no. 3, the operation of the loading system was studied with a sine wave load pattern in a wide load frequency range, from 0 to 200 Hz. The correlation between the set load and the measured load was high at frequencies below 100 Hz. At the frequency of 200 Hz, the cylinder was controllable, but the measured load was only about 1/10 of the set load. The results from the test are presented in Figure 3.

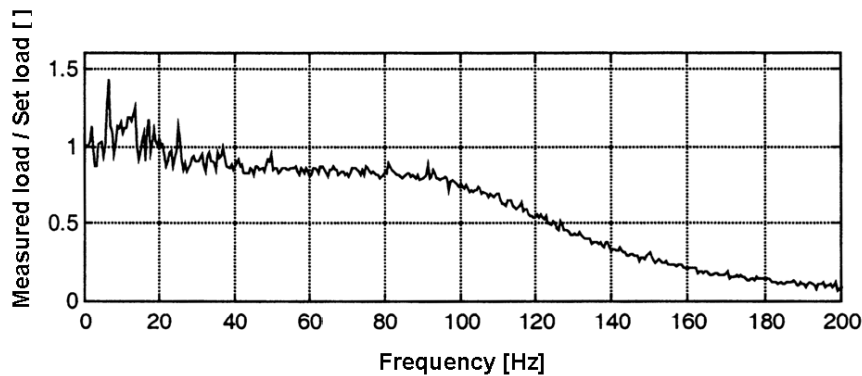


Figure 3. Correlation between the set and measured loads in the frequency range from 0 to 200 Hz with a sine wave load pattern in cylinder no. 2. (VTT Technical Research Centre of Finland)

Test no. 4 studied the operation of the loading system at low load levels and with rapid changes in load levels. A step function was used for step load patterns to control the loads. The delay between the set load and measured loads was about 5 ms. The rise time was about 10 ms. The results from the test are shown in Figure 4.

In test no. 5, the synchronization of the load cylinders was studied with a sine wave load. The set load level used was 2.5 ± 1.5 kN. The frequencies used were 1, 10, 20 and 30 Hz. A constant phase difference (120°) was set between the set loads of adjacent cylinders. It was found that the cylinders operated synchronously. As the frequency was increased, the load amplitude decreased in all cylinders. The results from the test are presented in Figure 5.

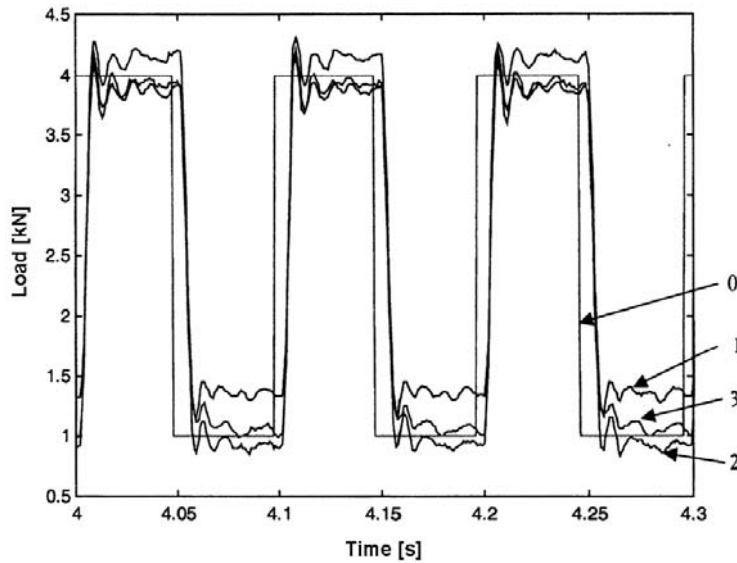


Figure 4. Set load (0) with loads generated by the cylinders no. 1 (1), no. 2 (2), and no. 3 (3) with a step function load. The set load was 2.5 ± 1.5 kN, and the step frequency was 10 Hz. (VTT Technical Research Centre of Finland)

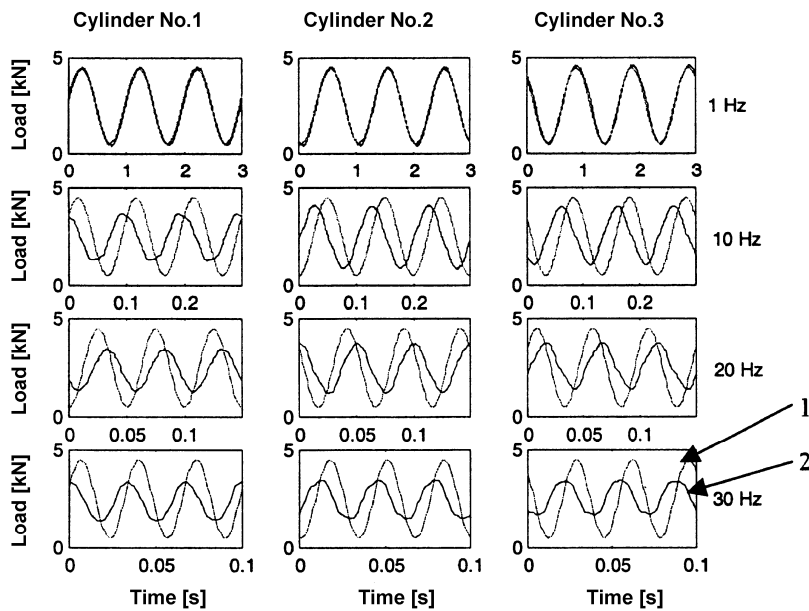


Figure 5. Set load (1), and measured load (2) in cylinders no. 1, no. 2, and no. 3 at frequencies 1, 10, 20 and 30 Hz. The set load was 2.5 ± 1.5 kN. (VTT Technical Research Centre of Finland)

Test no. 6 studied the operation of the loading system with a rotating load pattern. With a rotating load, all cylinders generated sine wave loads. There was a constant phase difference (120°) between the loads of adjacent cylinders. The resultant of the cylinder loads rotated around the centre axis of the shaft of the test rig. As the vertical component of the resultant was plotted as a function of the horizontal component of the resultant, its diagram resembled a circle. As the frequency was varied, it had certain effects on the size and shape of the above-mentioned circle. The results of the test are presented in Figure 6.

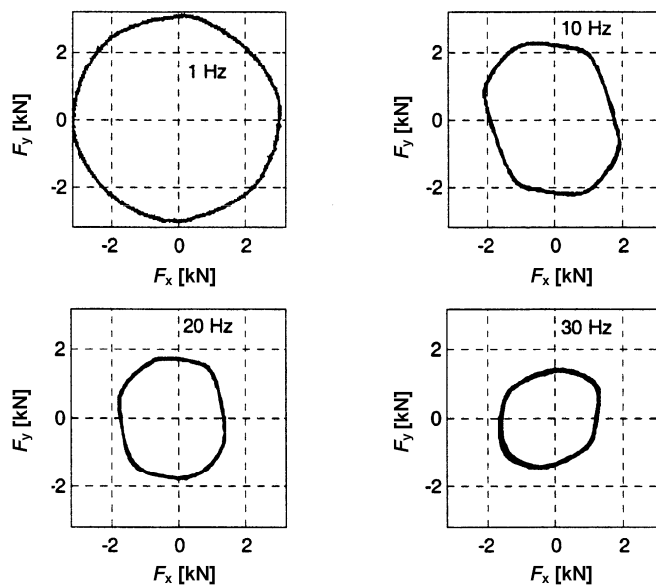


Figure 6. Components of the resultant R of cylinder loads with a rotating load. Vertical component F_y as a function of the horizontal component F_x . The set load (*i.e.*, the set resultant) was 3 kN. The frequencies were 1, 10, 20 and 30 Hz. (VTT Technical Research Centre of Finland)

Appendix C Calculations based on the engine data

The bearings used in this study were real main bearings (and other similar bearings) of a high-speed six-cylinder four-stroke diesel engine used as an experimental engine at Internal Combustion Engine Laboratory of Helsinki University of Technology (Tamminen and Sandström, 2003). To obtain estimates for typical sliding speeds and specific loads of the main bearing, common calculations based on the engine data were made. The engine data is presented in Table 1, and the results from the calculations are presented in Table 2. These estimates were used as reference data in the planning of experimental procedures and, finally, in the analysis of the results of the study.

Table 1. Engine data (by the engine manufacturer and Internal Combustion Engine Laboratory of Helsinki University of Technology).

Parameter	Value
Nominal output P_e [kW]	167
Torque at the nominal output M_{pe} [Nm]	723
Rotational speed at the nominal output n_{pe} [1/min]	2200
Output at the nominal torque P_{M0} [kW]	136
Nominal torque M_0 [Nm]	931
Rotational speed at the nominal torque n_{M0} [1/min]	1400
Cylinder bore or piston diameter D_p [mm]	108
Stroke S [mm]	134
Diameter of the main bearing D [mm]	85
Width of the main bearing B [mm]	32

The sliding speed u_s of the main bearing of the engine was calculated by the following equation:

$$u_s = \pi D n \quad (1)$$

where D is the diameter of the bearing,
 n is the rotational speed.

The mean piston speed C_m was calculated by the following equation:

$$C_m = 2 S n \quad (2)$$

where S is the stroke,
 n is the rotational speed.

The nominal output P_e of the engine was determined by the following equation:

$$P_e = \frac{\pi D_p^2 p_e C_m i}{8 j} \quad (3)$$

where D_p is the piston diameter,
 p_e is the mean effective pressure,
 C_m is the mean piston speed,
 i is the number of cylinders (for six-cylinder engines $i = 6$),
 j is the coefficient (for four-stroke engines $j = 2$).

In this case, the nominal output was known, and the mean effective pressure p_e was solved from the above-mentioned equation (3) by the following equation:

$$p_e = \frac{P_e 8 j}{\pi D_p^2 C_m i} \quad (4)$$

where P_e is the nominal output,

j is the coefficient (for four-stroke engines $j = 2$).

D_p is the piston diameter,

C_m is the mean piston speed,

i is the number of cylinders (for six-cylinder engines $i = 6$).

In a running engine, the bearing load is caused by gas and mass forces. Generally, the gas forces are clearly dominant at the nominal output. Therefore, in this case, the estimation of the bearing load was based on the gas forces, and the mass forces were excluded.

The mean gas force F_{Gm} was calculated by the following equation:

$$F_{Gm} = p_e A_p = p_e \pi \left(\frac{D_p}{2} \right)^2 \quad (5)$$

where p_e is the mean effective pressure,

A_p is the cross-sectional area of the piston,

D_p is the piston diameter.

The specific load p_s caused by the mean gas force was calculated by the following equation, which was formulated for this case, and which excludes the mass forces:

$$p_s = \frac{F_{Gm} k_1}{A_{Bp} k_2} = \frac{F_{Gm} k_1}{D B k_2} \quad (6)$$

where F_{Gm} is the mean gas force,
 k_1 is the number of pistons ($k = 1$ or 2),
 A_{Bp} is the projected area of the bearing,
 k_2 is the number of bearings ($k_2 = 2$ or 3),
 D is the diameter of the bearing,
 B is the width of the bearing.

In the above-presented equation (6), the number of pistons k_1 describes how many pistons generate the gas force, and the number of bearings k_2 describes how many bearing carry the gas force. The numbers k_1 and k_2 depend on the firing order of the cylinders and location of the bearing. These calculations were made for a case with one piston ($k_1 = 1$) and two bearings ($k_2 = 2$).

Table 2. Calculation results.

Parameter	Value at nominal torque	Value at nominal output
Sliding speed [m/s]	6.23	9.79
Mean piston speed [m/s]	6.25	9.83
Mean effective pressure [MPa]	1.03	1.24
Mean gas force [kN]	37.7	45.3
Specific load caused by the mean gas force [MPa]	6.93	8.33

Reference

Tamminen, J., and Sandström, C-E. 2003. Oil Film Thickness Simulations and Measurements of a Main Bearing in a High Speed DI Engine Using Reduced Engine Speed. Proceedings of the Ricarco Software 9th Annual International Users Conference. MI, USA. March 6th and 7th, 2003. 5 p.

Appendix D Heat transfer coefficient

The heat transfer coefficient in a cooling test was determined in the following way: After a test rig experiment, the loading, drive and lubrication systems of the test rig were shut down. Next, when the test rig was cooling during a certain period of time $\Delta t_c = t_1 - t_0$, the operating temperature of the bearing T_B , the temperature of the housing T_H , and the ambient temperature T_R were measured. From the measured data, the average temperature difference ΔT_{a1} was calculated by the following equation:

$$\Delta T_{a1} = \frac{(T_{B0} - T_{B1}) + (T_{H0} - T_{H1})}{2} \quad (1)$$

where T_{Bi} is the operating temperature of the bearing,
 T_{Hi} is the temperature of the housing.

The average temperature difference ΔT_{a2} was calculated by the following equation:

$$\Delta T_{a2} = \frac{\frac{(T_{B0} + T_{B1})}{2} - T_R + \frac{(T_{H0} + T_{H1})}{2} - T_R}{2} \quad (2)$$

where T_{Bi} is the operating temperature of the bearing,
 T_{Hi} is the temperature of the housing,
 T_R is the ambient temperature.

Finally, the heat transfer coefficient h was calculated by the following equation:

$$h = \frac{P_c}{A \Delta T_{a2}} = \left(\frac{\Delta T_{a1}}{\Delta t_c} c m \right) \quad (3)$$

where P_c is the heat flow in free cooling,
 A is the surface area of the housing,
 ΔT_{a2} is the average temperature difference between the housing and the environment,
 ΔT_{a1} is the average decrease in temperature,
 Δt_c is the time period,
 c is the specific heat capacity of steel,
 m is the mass of the housing.

In addition, to estimate typical temperature gradients in (practically) free cooling (for example after a rapid decrease in the bearing load or sliding speed), the temperature gradient in free cooling $\Delta T_c / \Delta t$ was calculated by the following equation:

$$\Delta T_c / \Delta t = \frac{\Delta T_{a1}}{\Delta t_c} \quad (4)$$

where ΔT_{a1} is the average temperature difference,
 Δt_c is the period of time.

The input and output data from the cooling test are shown in Table 1 and Table 2, respectively.

Table 1. Input data from the cooling test.

Variable	Value
Period of time Δt_c [s]	605
Operating temperature of the bearing T_{B0} [°C]	76.97
Operating temperature of the bearing T_{B1} [°C]	72.3
Temperature of the housing T_{H0} [°C]	76.2
Temperature of the housing T_{H1} [°C]	73.9
Ambient temperature T_R [°C]	24.0
Surface area of the housing A [m ²]	0.34
Specific heat capacity of steel c [J/kgK]	500
Mass of the housing (including masses of the force ring and sealing covers) m [kg]	67.5

Table 2. Output data from the cooling test.

Variable	Value
Temperature difference ΔT_{a1} [K]	3.485
Temperature difference ΔT_{a2} [K]	50.84
Heat transfer coefficient h [W/m ² K]	11.2
Temperature gradient in free cooling $\Delta T_c / \Delta t_c$ [K/s]	-0.006

Appendix E Calibration of the optical sensors

The first calibration process, carried out before the test rig experiments with a rotating load

The calibration of the optical sensor was carried out using the calibration device of VTT Technical Research Centre of Finland. The measured optical intensity was transformed into voltage by VTT Technical Research Centre of Finland. The voltage as a function of the time during three calibration sets is presented in Figure 1. The voltage as a function of the pressure in three calibration sets is presented in Figure 2. The average value of the voltage as a function of the pressure is presented in Figure 3. A linear function was chosen to present the voltage as a function of the pressure. The scale coefficient or gradient $C = -1.56 \cdot 10^8 \text{ Pa/V}$ was calculated from the coefficients of the linear function with $R^2 > 0.99$.

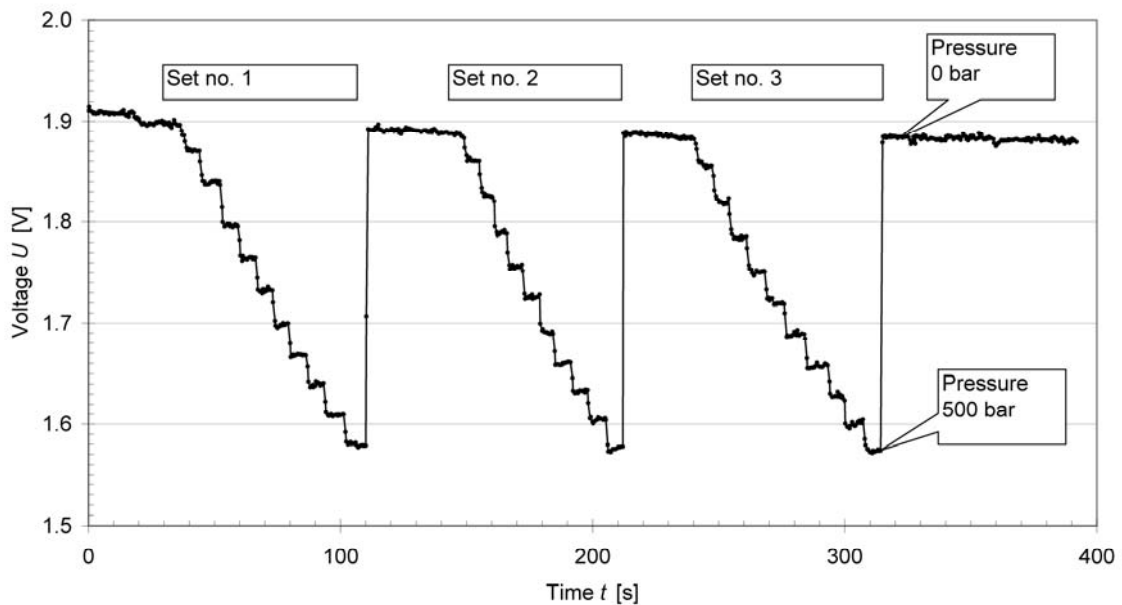


Figure 1. Voltage as a function of the time during three calibration sets. The pressure was increased step by step from 0 to 500 bar. The pressure step was 50 bar.

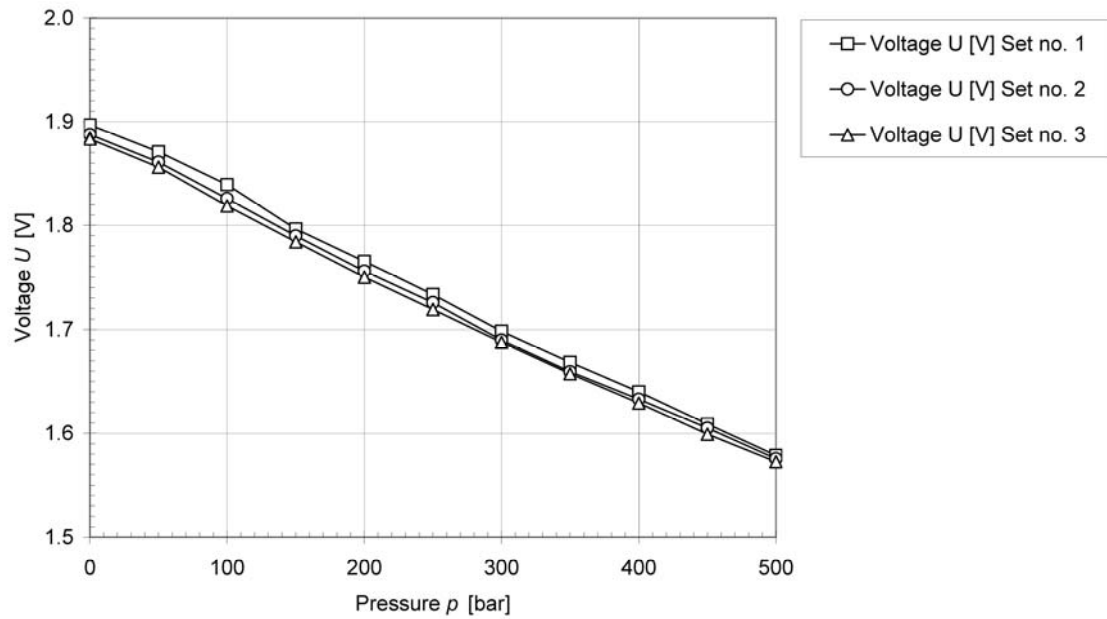


Figure 2. Voltage as a function of the pressure during three calibration sets.

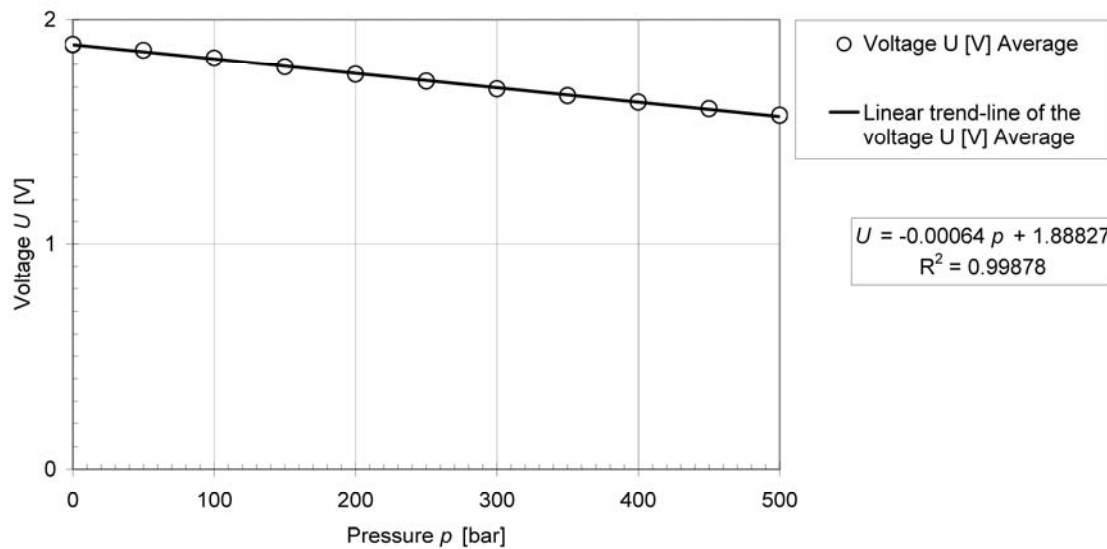


Figure 3. Average value of the voltage as a function of the pressure. The data was from three calibration sets. The scale coefficient C was calculated from the coefficients of the linear trend-line of the voltage. The result showed that the scale coefficient or gradient $C = 500 \text{ bar} / (500 \text{ bar} \cdot -0.00064 \text{ V/bar}) = -1.56 \cdot 10^8 \text{ Pa/V}$.

The second calibration process, carried out after the test rig experiments with a rotating load

The calibration of the optical sensor was carried out using the calibration device of VTT Technical Research Centre of Finland. The measured optical intensity was transformed into voltage by VTT Technical Research Centre of Finland. The voltage as function of the time during four calibration sets is presented in Figure 4. The voltage as a function of the pressure in four calibration sets is presented in Figure 5. The average value of the voltage as a function of the pressure is presented in Figure 6. A linear function was chosen to present the voltage as a function of the pressure. The scale coefficient or gradient $C = -1.37 \cdot 10^8 \text{ Pa/V}$ was calculated from the coefficients of the linear function with $R^2 > 0.99$.

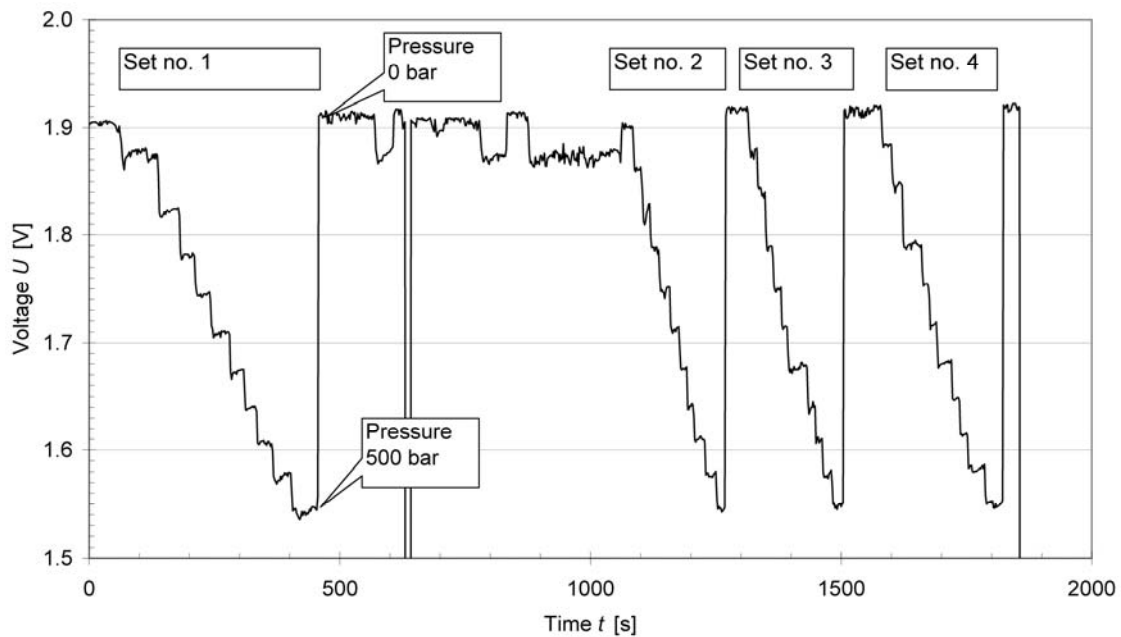


Figure 4. Voltage as a function of the time during four calibration sets. The calibration pressure was varied step by step from 0 to 500 bar. The pressure step was 50 bar.

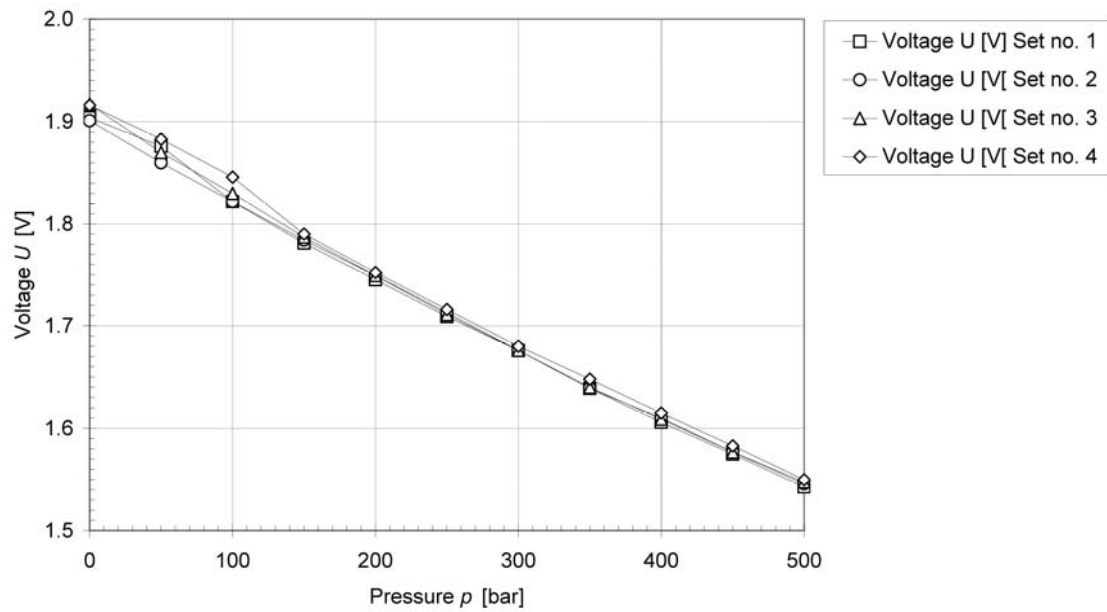


Figure 5. Voltage as a function of the pressure in four calibration sets.

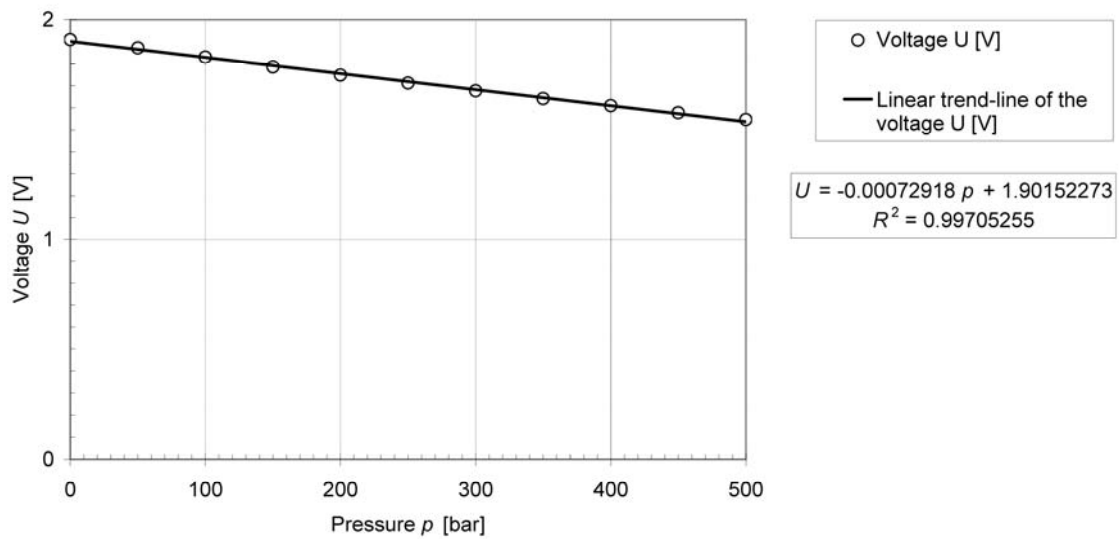


Figure 6. Average value of the voltage as a function of the pressure. The data was from four calibration sets. The scale coefficient C was calculated from the coefficients of the linear trend-line of the voltage. The result showed that the scale coefficient or gradient $C = 500 \text{ bar} / (500 \text{ bar} \cdot -0.000729 \text{ V/bar}) = -1.37 \cdot 10^8 \text{ Pa/V}$.

The third calibration process, carried out before the test rig experiments with a static load

The calibration of the optical sensor was carried out using the calibration device of VTT Technical Research Centre of Finland. The measured optical intensity was transformed into voltage and the relationship between the voltage and pressure was calculated by VTT Technical Research Centre of Finland. The voltage as function of the pressure is presented in Figure 7. The pressure as a function of the voltage is presented in Figure 8.

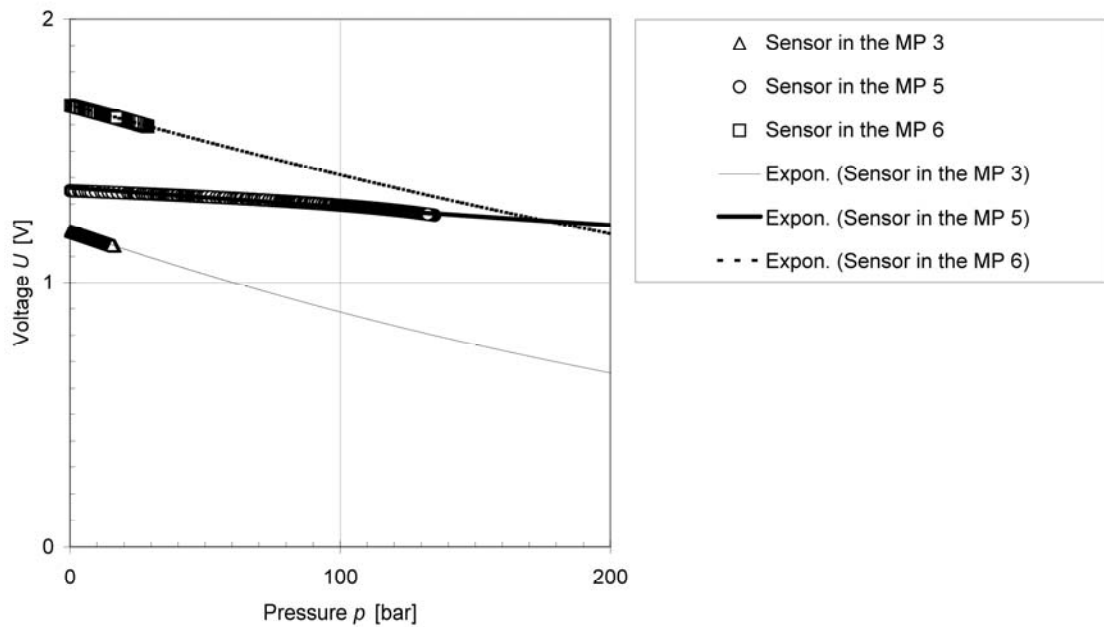


Figure 7. Voltage as a function of the pressure with exponential trend-lines. The optical pressure sensors were located at measurement points (MP) 3, 5 and 6.

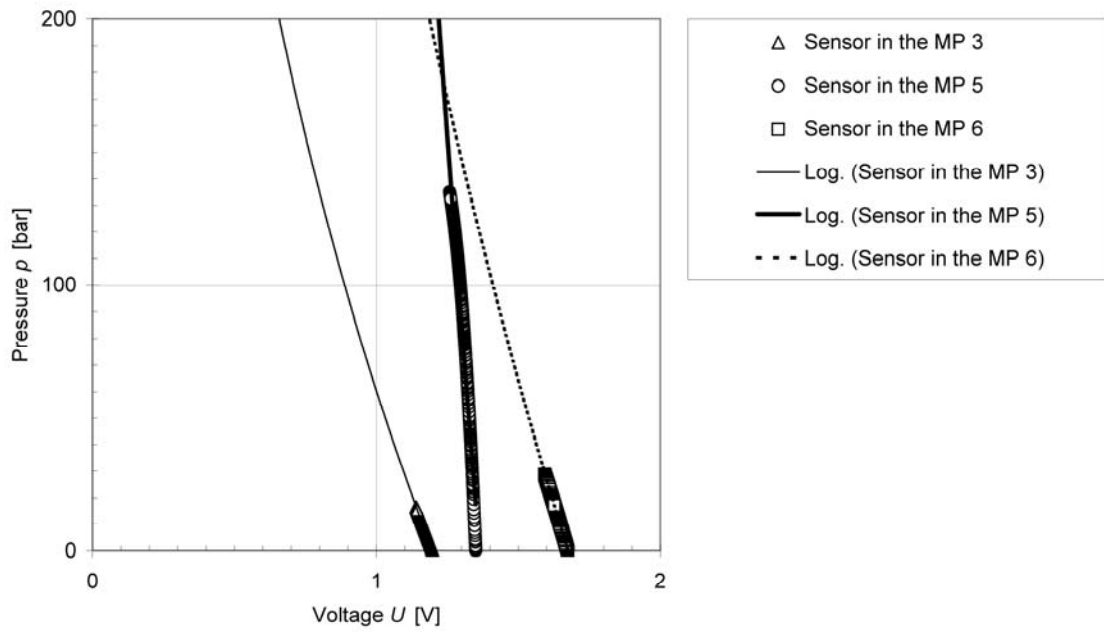


Figure 8. Pressure as a function of the voltage with logarithmic trend-lines. The optical pressure sensors were located at measurement points (MP) 3, 5 and 6.

Appendix F Relative eccentricity

The relative eccentricity ε was determined approximately as a function of the Sommerfeld number So and the width-to-diameter ratio B/D . The approximation of relative eccentricity was based on a graph which is presented in a standard for hydrodynamic journal bearings with a static load (DIN 31652 Teil 2, 1983) and in which the Sommerfeld number So is presented as a function of the width-to-diameter ratio B/D at different values of the relative eccentricity ε . The estimated relative eccentricity in a typical case (with the width $B = 32$ mm, the diameter $D = 85$ mm, and the width-to-diameter ratio $B/D = 0.376$) is presented in Figure 1.

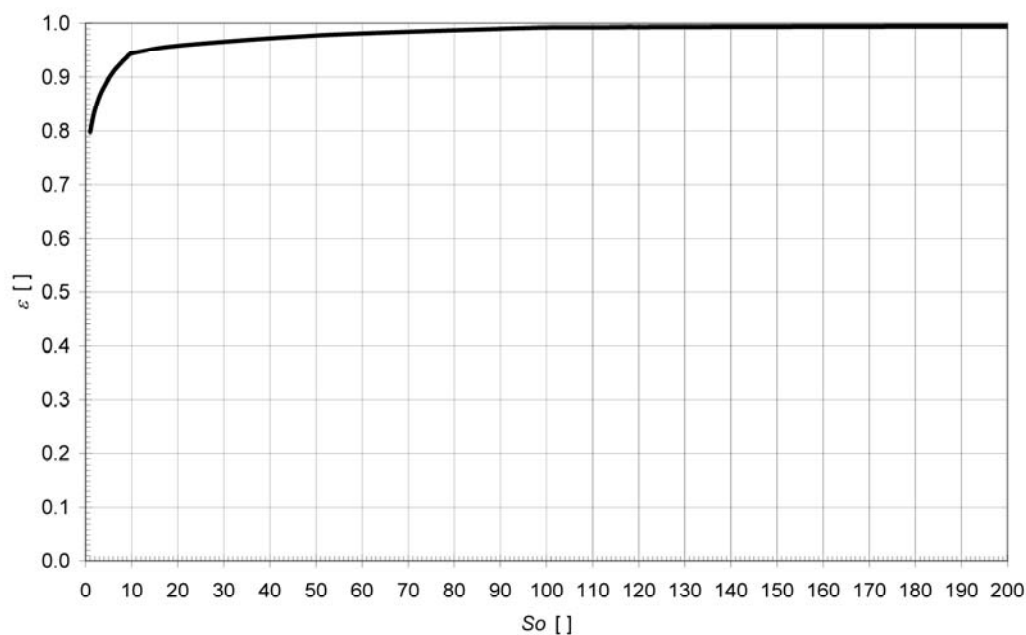


Figure 1. Estimated relative eccentricity ε as a function of the Sommerfeld number So . The width-to-diameter ratio B/D is 0.376, and $1 < So < 200$.

Reference

DIN 31652 Teil 2. 1983. Hydrodynamische Radial-Gleitlager im Stationären Betrieb. Funktionen für die Berechnung von Kreiszyylinderlagern. Februar 1983. 19 p.

Appendix G Viscosity and density

In the simulations, the dynamic viscosity of lubricating oil G was calculated by the Fogel-Barus method. The dynamic viscosity as a function of the pressure is presented in Figure 1. The dynamic viscosity as a function of the temperature is presented in Figure 2. The density of lubricating oil G was calculated by the Dowson-Higginson method. The density as a function of the pressure is presented in Figure 3. The density as a function of the temperature is presented in Figure 4.

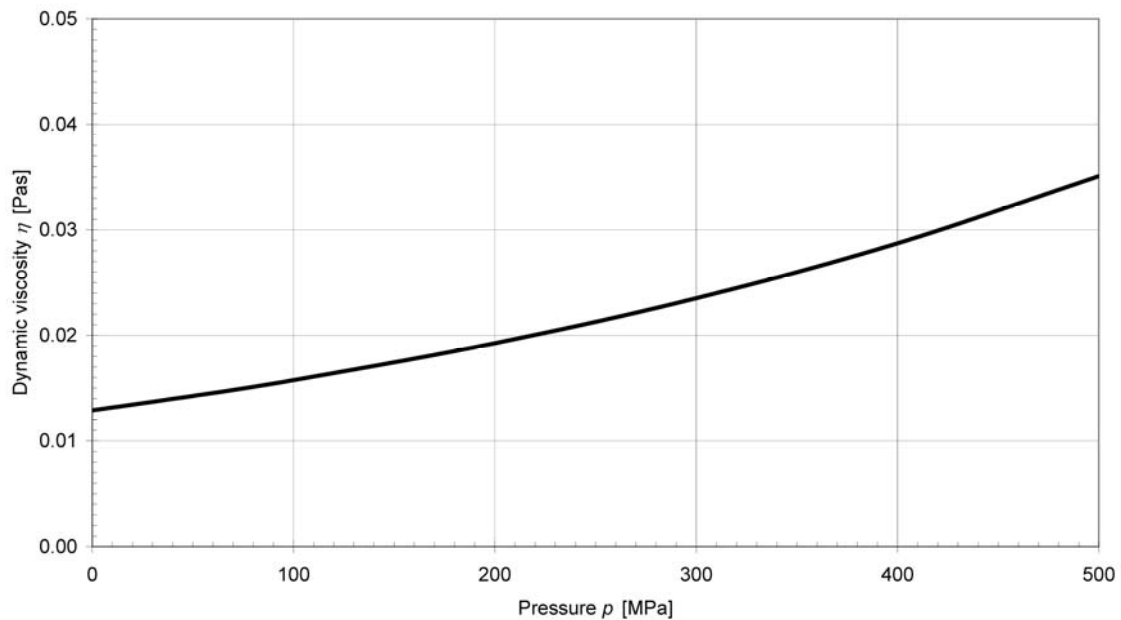


Figure 1. Simulated dynamic viscosity of oil G as a function of the pressure at a constant temperature of 100 °C.

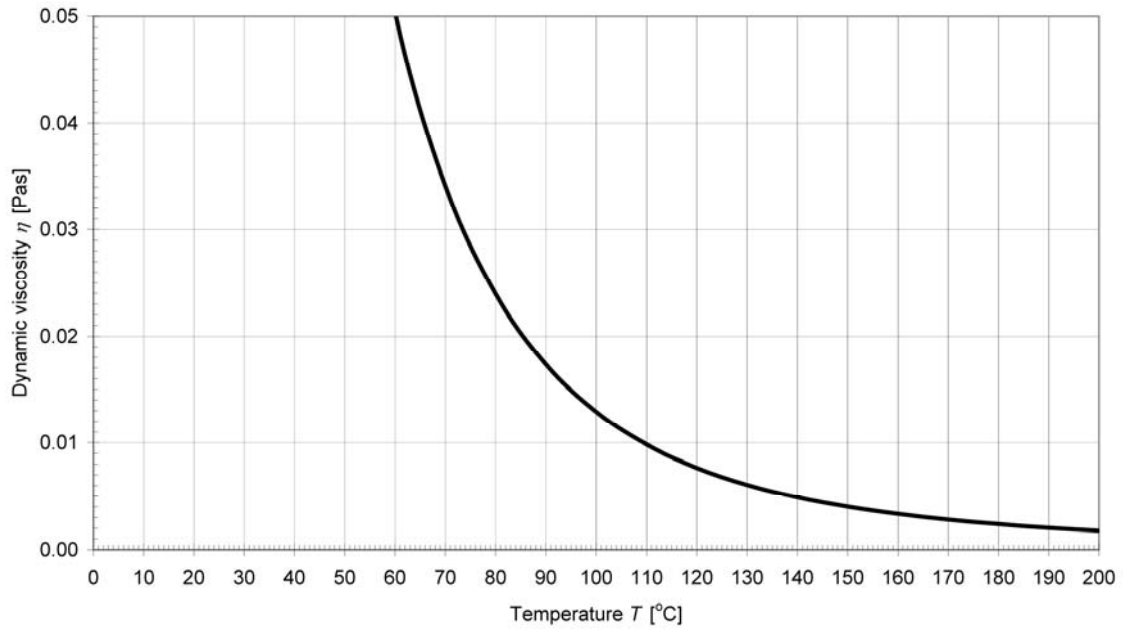


Figure 2. Simulated dynamic viscosity of oil G as a function of the temperature at a constant pressure of 1 bar.

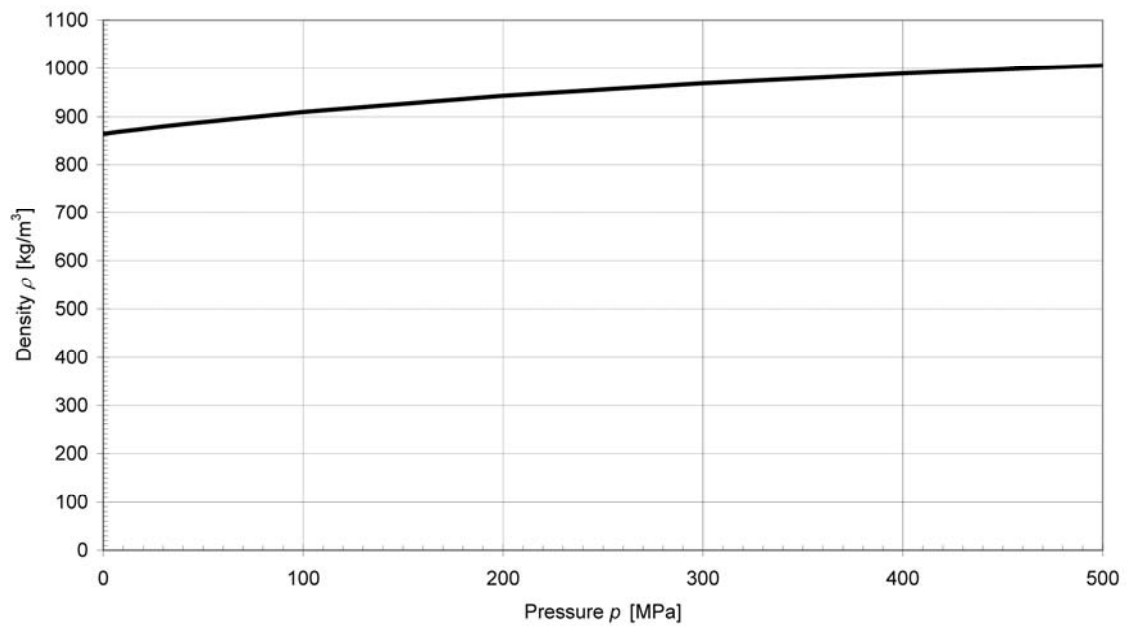


Figure 3. Simulated density of oil G as a function of the pressure at a constant temperature of 100 °C.

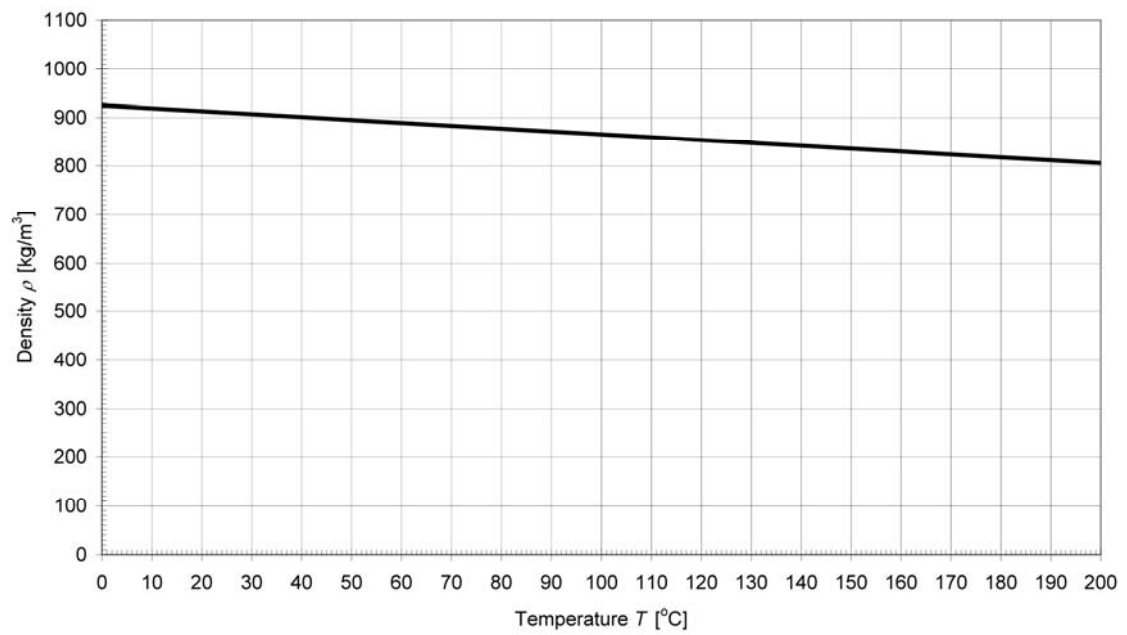


Figure 4. Simulated density of oil G as a function of the temperature at a constant pressure of 1 bar.

Appendix H Resultant of the local forces

The simulated and measured data related to the oil film pressure was used to determine the bearing load as the resultant of the local forces pointing in the radial direction on the sliding surface of the bearing. To determine the local forces, mathematical grids with various nodes in circumferential rows and axial columns were used.

Number of nodes in the grids

The total number of the nodes in the grid of simulated data was 2299 and there were 121 nodes in each circumferential row and 19 nodes in each axial column. In the grid of the measured data, the total number of nodes varied. The number of nodes in the circumferential direction N was determined by using the following equation:

$$N = 1 + \frac{s f_s}{u_s} \quad (1)$$

where s is the length of the bearing in the circumferential direction,
 f_s is the sampling frequency,
 u_s is the sliding speed.

The number of nodes in the axial direction M was set to 19, which was equal to the value used in the simulations.

Oil film pressure distributions

The simulated data included the oil film pressure in the circumferential and axial directions. In other words, the simulated oil film pressure distributions on the sliding surface of the bearing were known. The measured data only included the oil film pressure in the circumferential direction at the centreline of the sliding surface of the bearing. In other words, only the circumferential oil film pressure distribution was known. Therefore, the axial oil film pressure distribution was estimated based on the

simulated data. It was assumed that the real axial oil film pressure distribution resembled that determined by the simulations. Because parabolic equations were found to describe the simulated oil film pressure in the axial direction, the oil film pressure p in the axial direction was estimated by using the following equation of a parabola:

$$p(x) = p_c \frac{ax^2 + c}{c}, \quad a < 0 \quad (2)$$

where p_c is the measured oil film pressure at the circumferential centreline of the sliding surface of the bearing,
 a is the constant,
 x is the axial coordinate,
 c is the constant.

The constants a and c in the above-presented equation (2) were chosen so that the oil film pressure at the edges of the bearing was zero.

Local forces in the nodes of the grids

The local forces (or nodal forces) F_{local} in the nodes of the grids were determined by the following equation:

$$F_{\text{local}} = p_{\text{local}} A_{\text{local}} = p_{\text{local}} \Delta s \Delta B = p_{\text{local}} \frac{s}{N-1} \frac{B}{M-1} \quad (3)$$

where p_{local} is the oil film pressure in the node,
 A_{local} is the surface area around the node,
 N is the number of nodes in the circumferential direction,
 M is the number of nodes in the axial direction,
 s is the length of the bearing in the circumferential direction,
 B is the width of the bearing.

The local force F_{local} was divided into its horizontal and vertical components. The horizontal component F_x was calculated by the following equation:

$$F_x = F_{\text{local}} \cos(\beta) \quad (4)$$

where F_{local} is the local force,
 β is the angle of direction.

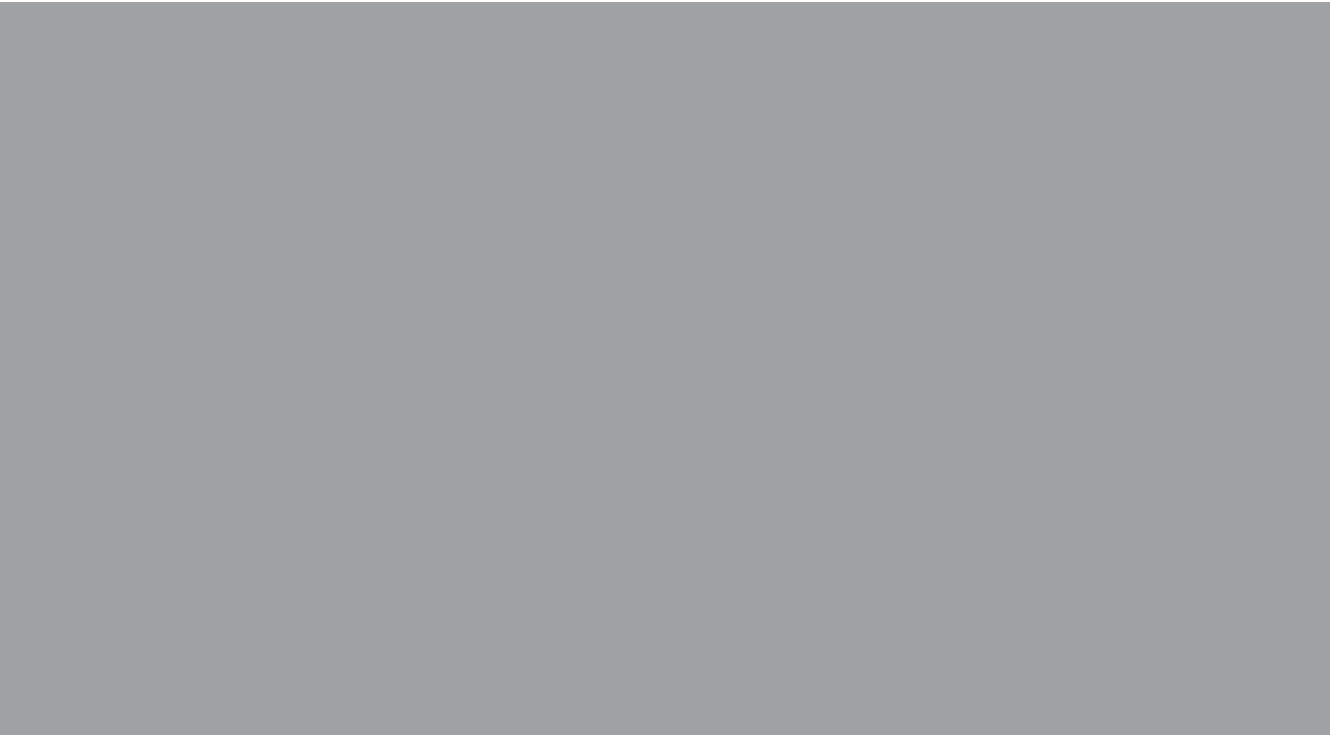
The angle of direction β in the equation (4) increased in a clockwise direction, and was zero as the local force pointed right, in a horizontal direction. The vertical component F_y was calculated by the following equation:

$$F_y = F_{\text{local}} \sin(\beta) \quad (5)$$

where F_{local} is the local force,
 β is the angle of direction.

Resultants of the local forces

The resultant L_{1s} of the simulated data and the resultant L_{1m} of the measured data were determined as the sums of magnitudes of the local forces F_{local} . The resultant L_{2s} of the simulated data and the resultant L_{2m} of the measured data were determined as the real resultants of the local forces F_{local} and, therefore, it was assumed that they were approximately equal to the bearing load L .



ISBN 978-952-248-161-0
ISBN 978-952-248-162-7 (PDF)
ISSN 1795-2239
ISSN 1795-4584 (PDF)